Study of the photon strength functions and level densities in the gamma decay following neutron capture on the isotopes ^{23} U, ^{23} U and ^{23} U

Javier Moreno Soto

université
PARIS-SACLAY

Study of the photon strength functions and level densities in the gamma decay following neutron capture on the isotopes ^{234}U, ^{236}U and ^{238}U

Thèse de doctorat de l'Université Paris-Saclay

École doctorale n° 576, Particules, Hadrons, Énergie, Noyau, Instrumentation, Imagerie, Cosmos et Simulation (PHENIICS)
Spécialité de doctorat: Structure et réactions nucléaires
Unité de recherche: Université Paris-Saclay, CEA, Institut de recherche sur les lois Fondamentales de l'Univers, 91191, Gif-sur-Yvette, France
Référent: Faculté des sciences d'Orsay

Thèse présentée et soutenue à Saclay, le 16 Octobre 2020, par

Javier MORENO SOTO

Composition du jury:

Araceli LOPEZ MARTENS Directrice de recherche, IJCLab, Orsay	Présidente
Beatriz JURADO Directrice de recherche, CENBG, Bordeaux	Rapporteure et examinatrice
José Luis TAIN Directeur de recherche, IFIC, Valencia	Rapporteur
Milan KRTIČKA Directeur de recherche, Charles University Prague	Examinateur
Olivier LITAIZE Ingénieur de recherche, DES, CEA Cadarache	Examinateur
Stéphane HILAIRE Ingénieur de recherche, CEA DAM-DIF	Examinateur
Frank GUNSING Directeur de recherche, Irfu, CEA Saclay	Directeur de thèse
Emmeric DUPONT Ingénieur de recherche, Irfu, CEA Saclay	Co-encadrant, invité

Thèse de doctorat

NNT: 2020UPASP033

Es peligroso, Frodo, cruzar tu puerta. Pones tu pie en el camino y si no cuidas tus pasos nunca sabes a dónde te pueden llevar.

– Bilbo Bolsón –

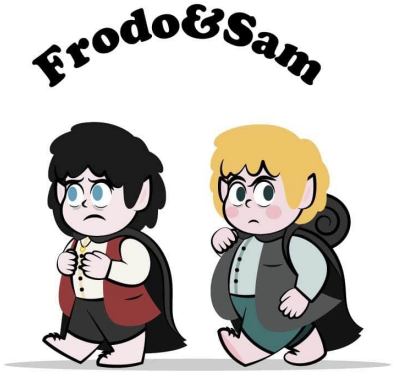

Acknowledgments

I have a lot of people that I wish to thank, so sorry if I forget someone. First, I wish to express a huge thank to my supervisor Frank Gunsing and my two co-supervisor Emmeric Dupont and Olivier Serot for the attention and dedication with my work. I wish to mention Eric Berthoumieux and Olivier Litaize who were always there to help me with software and technical questions.

During my stay in CEA Cadarache I want to highlight the hospitality of everyone. I especially want to mention Maria Diakaki, Fiona, Juliana, Nitendra, Julie-Anne and Jehaan with whom I have spent very nice moments.

I do not have enough lives to thank Stanislav Valenta for everything he has done for me. Although I was not his student and from a different country he always helped me to improve and understand better my work. Million thanks for that dedication to my work.

I am very grateful to have been part of the n_TOF collaboration. It allowed me to travel to some places but especially to the CERN which was awesome. In this point I want to mention Michael Bacak who was a good friend and sometimes I required his wisdom about lxplus.

Paso a escribir en español ya que lo más importante es siempre dicho en tu idioma. Si algo ha merecido la pena de este viaje de tres años lejos de casa, sin lugar a duda han sido todos los amigos que he hecho en el Colegio de España que ha sido mi hogar en París. Quiero empezar por mi primer grupo bautizado como "conosexuales" quienes me dieron amablemente su amistad en mis primeros meses de esta aventura y los cuales me ayudaron a asentarme en París y que fuese menos doloroso como lo son todos los comienzos lejos de tu hogar. También agradecer a mi otro grupo formado por Julia, Luis, Mariela, Marta, Pol y Ricardo con los que tengo muchos buenos recuerdos, aunque me quedo con esas cenas de comida asquerosa del crous y nuestras charlas. Hay muchos que no los puedo situar en ningún grupo pero forman una parte especial de esta historia como mis compañeros de habiatión Ferran y Carlos, mi amigo Sergio que tiene mi admiración y además me regaló un libro, y mi amigo Ricardo de Chile con quien desconectaba de trabajar los miércoles por la noche en la mina con bebida en mano y al que quiero un montón. Para terminar, darle mil gracias acompañado de mil besos a mi grupo formado por Valle, Juan Martín, Juan Álvarez, Rafa, Xenia, Ana, Alvaro, Ainoa y Emilio quienes más que un grupo fueron mi familia en París. Gracias por todas esas risas, por las charlas interminables en la cocina, por haberme hecho disfrutar de París, por los viajes, por animarme si estaba triste y por ser tan grandes como sois cada uno de vosotros.

Por último permitidme este párrafo para ponerme sentimental hablando de mi verdadero hogar, Sevilla. Yo a la vida le pedí amor y buenas personas, y la vida me ha dado tanto que no sé como dar las gracias. A mis tres amigos Gonzalo, Pablo y Jesús por estar durante estos tres años ahí para lo que hiciese falta, porque si en algún momento me he sentido solo ahí estabais en la pantalla de mi ordenador haciendome reir y si volvía a Sevilla ahí estabais haciéndome sentir de nuevo en casa. De verdad, gracias por vuestro apoyo y vuestra amistad. También quiero agradecer la tremenda fuerza de mi novia, Pilar, por tener una relación a distancia durante tanto tiempo. Yo me fuí a París

pero mi corazón no se subió al avión. Gracias por darme esa estabilidad emocional, por todos los viajes que hemos hecho, por todos los aviones que has tenido que coger para verme y por darme fuerzas para no rendirme. Has hecho que estos tres años se dividieran en pequeños capítulos más llevaderos.

Para terminar, infinitas gracias a mi familia. A mi hermano Álvaro a quien por motivos del covid-19 llevo sin verlo casi un año y aún estando al otro lado del mundo sigue cuidándome y procupándose por mi. Además, me ayudo con latex para escribir esta tesis. A mis padres a los que amo con todas mis fuerzas y han confiado siempre en mi. Gracias por haberme cuidado desde la distancia todos estos años y por haberme apoyado siempre. De pequeño se me daban fatal las matemáticas y gracias a vuestra dedicación habeis sido durante toda mi vida esa escalera por la que poder subir y alcanzar cualquier meta propuesta. Infinitas gracias.

Contents

Acronyms

ADC Analog to digital converters

ARC Average resonance capture

BSC Beam shaping collimator

BSFG Back-shifted Fermi gas

CAD Computer aided design

CASTOR CERN's advanced storage

CGCM Composite Gilbert and Cameron

CT Constant temperature

DANCE Detector for advanced neutron capture experiments

DAQ Data acquisition system

EGLO Enhanced generalized Lorentzian

ELO Enhanced Lorentzian

ENDF Evaluated Nuclear Data File

ENSDF Evaluation nuclear structure data file

GDR Giant dipole resonance

GEDR Giant electric dipole resonance

GEQR Giant electric quadrupole resonance

GFL Generalized Fermi liquid

GLO Generalized Lorentzian

GMDR Giant magnetic dipole resonance

HFB Hartree-Fock-Bogoliubov

IPPE Institute of physics and power engineering

JEFF Joint Evaluated Fission and Fusion

KMF Kadmenskii, Markushev and Furman

LD Level density

LINAC Linear accelerator

MGLO Modified generalized Lorentzian

MLO Modified Lorentzian

MSC Multi-step cascade

NRF Nuclear resonance fluorescence

OCL Oslo cyclotron laboratory

PS Proton synchrotron

PSA Pulse shape analysis

PSF Photon strength function

PTF Porter Thomas fluctuations

QRPA Quasiparticle random phase approximation

RIPL Reference input parameter library

SC Scissors

SF Spin-flip

SLO Standard Lorentzian

SSC Source screening collimator

TAC Total absoption calorimeter

TOF Time of flight

TRW Total radiation width

Résumé

Dans cette thèse, la fonction force radiative (PSF) et la densité de niveau (LD) dans la région d'énergie en dessous de l'énergie de liaison du neutron S_n ont été étudiées pour les réactions ^{234}U(n,γ), ^{236}U(n,γ) et ^{238}U(n,γ).

La PSF a été proposée comme une approximation des équations fondamentales régissant l'émission des rayons gamma, et est essentielle dans la modélisation des réactions nucléaires impliquant une excitation et une désexcitation électromagnétiques. De plus, la connaissance de la PSF peut être utilisée comme point de connexion entre la largeur partielle radiative et la section efficace de photoabsorption. Pendant de nombreuses années, beaucoup d'auteurs ont étudié la PSF à l'énergie au-dessus de l'énergie de liaison du neutron S_n où l'émission de rayons gamma est dominée par un mouvement collectif appelé résonance géante dipolaire (GDR) soit électrique (GEDR) soit magnétique (GMDR). Dans la bibliographie, nous pouvons trouver une grande variété de modèles pour reproduire ces données, ceux-ci peuvent être soit phénoménologiques (SLO, ELO, GLO, MGLO, entre autres) soit semi-microscopiques. Cependant, bien que ces modèles reproduisent les valeurs au sommet de la GEDR, le comportement de chaque modèle à une énergie inférieure à S_n est très différent. De plus, concernant les PSF inférieures à S_n, une contribution importante des transitions $M1$ a été identifiée. La contribution $M1$ est décrite par deux modes de vibrations - le mode ciseaux (SC) et le mode spin-flip (SF). Cependant, il y a encore un manque de connaissance de la PSF pour les actinides.

La LD peut être observée expérimentalement à une énergie d'excitation très faible où une description détaillée des niveaux nucléaires et des transitions existe, et légèrement au-dessus de S_n où les niveaux sont connus à partir des réactions neutroniques. Cependant, l'augmentation exponentielle de la densité de niveau rend impossible l'étude expérimentale des niveaux se chevauchant à plus haute énergie, où l'utilisation de modèles statistiques devient nécessaire. Une grande variété de formules a été développée pour la LD. Dans ce travail, nous n'utilisons que les modèles CT, BSFG et CGCM qui reproduisent avec un bon accord l'espacement D_0 des ondes s.

Les mesures de capture neutronique sur les isotopes ^{234}U, ^{236}U et ^{238}U ont été faites auprès de l'installation n_TOF du CERN. Cette installation consiste en un faisceau de protons fourni par le synchrotron à protons qui interagit avec une cible principale pour produire des neutrons de spallation. Ces neutrons sont modérés par l'eau autour de la cible de spallation et parcourent la ligne expérimentale de 185 m jusqu'à la zone expérimentale EAR1 où se trouvent l'échantillon à étudier et le détecteur. Le détecteur utilisé dans les trois mesures est le calorimètre à absorption totale (TAC) qui est un détecteur 4π segmenté en 40 cristaux de BaF_2. l'efficacité du TAC est proche de 100% pour détecter au moins un gamma ray émis par l'échantillon lors d'une cascade. De plus,

deux couches de matériaux absorbeurs de neutrons sont introduites entre l'échantillon et les cristaux car la principale source de bruit de fond est produite par les neutrons diffusés dans l'échantillon. Une couche est composée de ^{10}B enveloppant chaque détecteur et l'autre est une sphère composée d'un sel de lithium inerte non inflammable $C_{12}H_{20}O_4(^6Li_2)$ encapsulé par 0.5 mm d'Al pour la mesure avec l'échantillon de ^{234}U, et de polyéthylène boré inerte ininflammable enrichi à 5% de ^{10}B pour les autres mesures. 'Nous étudions les réactions ^{234,236,238}U(n,γ) avec de faibles énergies neutroniques jusqu'à quelques dizaines d'eV, nous pouvons donc considérer que l'énergie d'excitation initiale du noyau composé est environ S_n. Le noyau composé se désintègre vers l'état fondamental principalement via une cascade gamma avec une multiplicité typique entre 1 et 8. Les événements de la cascade sont reconstruits en prenant des rayons gamma détectés dans les détecteurs BaF_2 dans une fenêtre de coïncidence temporelle de 20 ns avec un seuil de détection de 250 keV. Les observables que nous pouvons créer avec le TAC pour l'analyse des données sont:

- Le spectre de temps de vol qui peut être exprimé en énergie du neutron E_n.
- La multiplicité des cristaux, m_{cr}, donnée par le nombre de cristaux touchés dans chaque événement de cascade.
- L'énergie somme E_{sum} déposée dans tous les détecteurs pour chaque événement de cascade.
- Les spectres de la cascade multi-étapes (MSC) pour chaque multiplicité m_{cr}, qui sont les spectres d'énergie gamma ray pour les cascades entièrement détectées.

Les spectres de temps de vol donnent accès à l'énergie des résonances. Chaque résonance correspond à un niveau spécifique du noyau composé peuplé après la réaction de capture du neutron et décroissant vers l'état fondamental via une cascade électromagnétique. À l'intérieur de ces résonances, nous définissons une fenêtre temporelle pour créer les autres observables. Dans ces spectres, nous constatons qu'il n'y a pas d'autres isotopes d'uranium parce que les trois échantillons sont proche d'une pureté de 100%. De plus, pour réduire l'effet du temps mort dans l'analyse des données, nous avons décidé de ne prendre que des fenêtres de temps avec un taux de comptage inférieur à 0,20 coups/μs par impulsion. d'autre part, la soustraction du bruit de fond a été estimée pour chaque résonance à partir des spectres des régions voisines après interpolation linéaire. Cette méthode reproduit très bien le comportement du bruit de fond dans les spectres des trois uranium dans toutes les résonances utilisées dans ce travail. Dans le cas de ^{234}U(n,γ) la soustraction du bruit de fond reproduit la contribution des isotopes du titane recouvrant cet échantillon. De plus, le bruit de fond peut être supprimé des spectres avec une sélection sur la multiplicité des cristaux. On s'attend à ce que les spectres E_{sum} pour $m_{cr} = 1$ soient dominés par le bruit de fond en dessous de 2 MeV tandis que pour $m_{cr} \geq 2$, ce bruit de fond est presque soustrait. Enfin, nous comparons quelques résonances avec le même spin et la même parité, $1/2^+$, pour considérer les possibles variations. La normalisation des spectres se fait par l'intégrale de E_{sum} avec $m_{cr} \geq 2$ entre $E_{sum} = 5.0 - 5.6$ MeV pour ^{234}U(n,γ), $E_{sum} = 4.9 - 5.3$ pour ^{236}U(n,γ) et $E_{sum} = 4.5 - 4.8$ MeV pour ^{238}U(n,γ). Ces fenêtres dans le pic de somme sont également

utilisées pour créer les spectres MSC et la distribution de multiplicité car nous nous intéressons aux événements de cascade dans lesquels toute l'énergie gamma émise par l'échantillon est détectée par le TAC. Nous pouvons voir certaines différences entre les résonances qui sont attribuées aux fluctuations de Porter Thomas dans l'intensité primaire. Ces fluctuations sont plus évidentes dans les spectres MSC pour $m_{cr} = 2$ car elles sont composées de deux transitions d'intensité spécifique. Pour une visualisation facile des données expérimentales, nous avons décidé de ne montrer que les spectres moyens et leur écart-type qui est représentatif de la fluctuation de Porter Thomas.

Les codes de simulation utilisés pour la simulation de la cascade gamma sont DICEBOX et FIFRELIN. L'objectif principal de FIFRELIN est la simulation de l'émission neutron/gamma dans le processus de fission, nous testons donc ici la validité de ce code pour la modélisation de la cascade électromagnétique en comparant avec DICEBOX. Ces deux codes simulent des ensembles de niveaux produits à partir d'une formule de densité de niveau et des ensembles aléatoires de largeurs partielles radiatives, appelées réalisations nucléaires. La largeur radiative partielle pour les transitions entre deux niveaux suite à un choix aléatoire de la distribution de Porter Thomas est reliée à la PSF et à la LD. La simulation de l'ensemble des niveaux par DICEBOX peut être divisée en deux régions:

- La région en dessous d'une certaine énergie d'excitation critique E_{crit} qui est considérée expérimentalement connue, et les énergies de niveau, spins, parités, intensités de branchement des transitions de dépeuplement, entre autres, sont tirées de la base de données ENSDF.

- La région au-dessus de E_{crit} où le schéma de niveau est inconnu et un ensemble complet de niveaux nucléaires est calculé par une discrétisation aléatoire d'une LD connue a priori.

FIFRELIN utilise trois régions:

- La région au-dessous d'une certaine énergie d'excitation appelée $E_{cut-off}$ fournie par RIPL-3 qui est considérée expérimentalement connue, et toutes les informations pour la simulation de la cascade sont tirées de la base de données RIPL-3.

- La région entre $E_{cut-off}$ et E_{bin} qui correspond à la limite d'énergie dans laquelle la valeur de densité de niveau par défaut est $5 \cdot 10^4$ MeV^{-1}. Dans cette région, les niveaux expérimentaux connus sont complétés par une formule LD.

- La région au-dessus de E_{bin} où le schéma de niveau est considéré comme un continuum et la discrétisation des niveaux est donnée par une LD.

Une fois créée la réalisation nucléaire, la transition vers le niveau suivant est choisie au hasard jusqu'à ce que l'état fondamental ou un état isomérique soit atteint. Afin d'avoir suffisamment de statistique et pour tenir compte des fluctuations de Porter Thomas nous devons utiliser dans la simulation 20 réalisations nucléaires et 10^5 cascades par réalisation. Après la simulation de la cascade gamma nous utilisons GEANT4 pour la simulation de l'interaction et la détection de ces rayons gamma avec le TAC. Dans la simulation GEANT4 du TAC on introduit 40 cristaux BaF_2 ainsi que leurs tubes photomultiplicateurs à l'intérieur d'un boîtier en aluminium, les deux couches de matériaux

absorbeur de neutrons, les tubes de faisceau en aluminium sous vide, le porte-échantillon au milieu du TAC et la structure en nid d'abeille qui porte l'ensemble. Enfin, dans la reconstruction d'événements, nous incluons la résolution de chaque détecteur, le seuil de 250 keV et l'effet du taux de comptage (temps mort et empilement). L'objectif principal est d'être aussi proche que possible des mesures réelles.

Ensuite, nous comparons les spectres simulés avec les spectres mesurés. Les réactions ^{234,236,238}U(n,γ) ont déjà été étudiées à partir de différentes expériences dans des travaux précédents. Une combinaison de modèles et de paramètres pour la LD et la PSF peut être extraite de la base de données RIPL-3, de l'analyse des réactions induites par d et ^{3}He sur des cibles d'actinides réalisées au laboratoire d'Oslo (OCL), et à partir de la mesure de spectres des cascades multi-étapes émis lors de la capture de neutrons par des échantillons d'uranium avec le calorimètre DANCE. Le modèle SLO est utilisé pour la PSF $M1$ dans les trois analyses alors que la combinaison de la LD et de la PSF $E1$ ne sont pas toujours les mêmes. Cependant, la plupart des différences pertinentes entre les trois analyses sont (i) la base de données RIPL-3 n'inclut pas le mode SC pour décrire la PSF $M1$, (ii) OCL introduit le mode SC et une Lorentzienne supplémentaire à environ 7 MeV appelée résonance pygmée pour définir la PSF $E1$, et (iii) l'analyse de DANCE exclut la résonance pygmée et ajuste les paramètres de la PSF $M1$ pour reproduire les données expérimentales. De la comparaison entre ces trois simulations de la distribution de multiplicité expérimentale, des spectres E_{sum} et MSC, nous pouvons conclure que l'utilisation du mode SC pour décrire la PSF $M1$ est obligatoire pour reproduire les données expérimentales, notamment le comportement des spectres MSC entre 2 et 3.5 MeV. Les meilleurs résultats ont été obtenus avec les paramètres de DANCE. Cependant, aucune des trois simulations n'a produit un bon accord dans le calcul de la largeur totale radiative Γ_γ (TRW) pour les trois uranium en utilisant la même paramétrisation. De plus, le seul ensemble de paramètres de la PSF $E1$ qui reproduise la tendance de la PSF expérimentale calculée avec la section efficace de photoabsorption de Caldwell autour du GEDR est donné par RIPL-3. Dans l'analyse OCL la PSF est surestimée parce que la paramétrisation inclus la section de photofission alors que pour DANCE la PSF est sous-estimée en raison d'un facteur d'échelle de 0.5. En revanche, les modèles semi-microscopiques de la LD basée sur les modèles combinatoire et HFB et de la PSF basée sur des calculs D1M + QRPA avec limite non nulle à E_γ ont montré un bon accord avec le données expérimentales pour ^{236}U(n,γ) tandis que pour ^{234}U(n,γ) et ^{238}U(n,γ) l'accord n'est bon que pour $m_{cr} \geq 4$. Pour des multiplicités plus faibles, $m_{cr} \leq 3$, les différences sont clairement visibles dans les spectres MSC de ces deux isotopes d'uranium et des améliorations peuvent encore être apportées.

En tenant compte de tous les résultats mentionnés précédemment, nous étudions de nombreuses combinaisons PSF + LD en utilisant différents modèles et paramètres cohérents pour la PSF $E1$ tandis que pour la contribution $M1$, les paramètres sont ajustés pour reproduire les données n_TOF. De plus, les simulations sont guidées par un coefficient ad hoc qui prend des valeurs plus faibles pour une meilleure reproduction des données expérimentales. Comme contrainte supplémentaire, nous utilisons les résultats de Γ_γ pour exclure certaines combinaisons de modèles. En regardant la dépendance par rapport à LD, la TRW calculée avec BSFG est toujours plus élevée que lors de l'utilisation du modèle CT. Ce comportement est attendu car BSFG tend à augmenter

le nombre de niveaux plus rapidement que CT en dessous de S_n. De plus, la TRW a montré une sensibilité élevée aux modèles de LD avec un comportement similaire. En ce qui concerne la PSF, la valeur de Γ_γ augmente pour une force plus élevée de la PSF. Enfin, nous devons utiliser le modèle MGLO avec $k_0 = 1.8$ et T = 0.3 MeV pour la PSF en combinaison avec le modèle CT pour la LD afin de reproduire des valeurs cohérentes de TRW pour les trois isotopes de l'uranium et un bon accord avec les spectres expérimentaux.

Nous avons validé FIFRELIN pour la modélisation de la cascade électromagnétique. Après avoir vérifié tous les paramètres par défaut utilisés par FIFRELIN dans la simulation, nous concluons que FIFRELIN ne doit pas utiliser les paramètres par défaut de RIPL-3 de la PSF afin de reproduire les données expérimentales. De plus, nous comparons FIFRELIN et DICEBOX en utilisant les mêmes modèles et paramètres pour la PSF et la LD. Les résultats sont similaires avec quelques petites variations dues à l'utilisation de différentes bases de données nucléaires (ENSDF pour DICEBOX et RIPL-3 pour FIFRELIN) pour décrire les niveaux de faible énergie.

Nous avons également étudié la sensibilité des différents paramètres de la PSF et de la LD impliqués dans la simulation. Cet exercice a été limité au cas de la variation relative du TRW aux paramètres des Lorentziennes de la PSF dans une plage de 50%. En analysant la tendance des valeurs de TRW, nous avons observé que les simulations sont plus sensibles aux changements des paramètres E que des paramètres Γ et σ. De plus, pour la PSF $E1$ les paramètres les plus sensibles correspondent à la deuxième Lorentzienne tandis que pour la PSF $M1$ ils correspondent à la première Lorentzienne du mode SC. Pour les paramètres de la LD correspondant au modèle CT, nous avons fait un exercice similaire en étudiant la variation relative de l'espacement D_0 des ondes s. Les résultats montrent une sensibilité élevée au paramètre de température du modèle CT.

Enfin, il est intéressant d'étudier la relation entre les PSF $M1$ et $E1$. Pour cela, nous étudions trois simulations avec des valeurs différentes du paramètre k_0 dans le modèle MGLO. Nous avons constaté qu'un rapport similaire $M1/E1$ est préservé lors de la reproduction des données expérimentales. Cependant, si la tendance du modèle $E1$ est très différente, le rapport $M1/E1$ sera également différent.

Summary

In this thesis the photon strength function (PSF) and the level density (LD) in the energy region below the neutron binding energy S_n have been studied for the ^{234}U(n,γ), ^{236}U(n,γ) and ^{238}U(n,γ) reactions.

The PSF was proposed as an approximation of the fundamental equations governing the gamma ray emission, and is essential in the modelling of nuclear reactions involving electromagnetic excitation and deexcitation. In addition, the knowledge of the PSF can be used as a connection point between the partial radiation width and the photoabsorption cross section. During many years many authors have studied the PSF at high energy above the neutron binding energy S_n where the gamma ray emission is dominated by a collective movement called giant dipole resonance (GDR) either electric (GEDR) or magnetic (GMDR). In the bibliography we can find a wide variety of models to reproduce these data which can be either phenomenological (SLO, ELO, GLO, MGLO, among others) or semi-microscopic. However, although these models reproduce the values at the peak of the GEDR, the behaviour of each model at lower energy below S_n is very different. Moreover, regarding the PSF below S_n an important contribution of $M1$ transitions has been identified. The $M1$ strength is described by two vibration modes – the scissor mode (SC) and the spin-flip mode (SF). However, there is still a lack of knowledge of the PSF for actinides.

The LD can be experimentally observed at very low excitation energy where a detailed description of nuclear levels and transitions exists, and slightly above S_n where levels are known from neutron reactions. However, the exponential increase in the level density makes the experimental study of overlapping levels impossible at higher energy, where the use of statistical models becomes necessary. A wide variety of formulas has been developed for the LD. In this work we only use the CT, BSFG and CGCM models which reproduce with a good agreement the s-wave spacing D_0.

The measurements of the neutron capture on the isotopes ^{234}U, ^{236}U and ^{238}U were done at the n_TOF facility at CERN. This facility consists of a proton beam provided by the proton synchrotron accelerator which interacts with a lead target to produce spallation neutrons. These neutrons are moderated by water around the spallation target and travel along the experimental line of 185 m until the experimental area EAR1 where the sample under study and the detector are located. The detector used in the three measurements was the total absorption calorimeter (TAC) which is a 4π detector segmented in 40 BaF_2 crystals. The efficiency of the TAC is nearly 100% to detect at least one gamma ray emitted from the sample in a cascade event. In addition, two layers of neutron absorber materials are introduced between the sample and the crystals because the main source of background is produced by neutrons scattered from the

sample. One layer was composed of ^{10}B wrapping each detector and the other one is a sphere composed of an inert non-flammable lithium salt $C_{12}H_{20}O_4(^6Li_2)$ encapsulated by 0.5 mm of Al for the measurement with the sample of ^{234}U, and of inert non-flammable borated polyethylene enriched to 5% of ^{10}B for the other measurements.

We study the ^{234,236,238}U(n,γ) reactions with low neutron energies up to a few tens of eV, so we can consider that the initial excitation energy of the compound nucleus is around S_n. The compound nucleus decays to the ground state mostly via a gamma cascade with typical multiplicity between 1 and 8. The cascade events are reconstructed by taking gamma rays detected in the BaF_2 detectors in a time coincidence window of 20 ns with a detector threshold of 250 keV. The observables that we can create with the TAC for the data analysis are:

- The time-of-flight spectrum which can be expressed in neutron energy E_n.
- The crystal multiplicity, m_{cr}, given by the number of hit crystals in each cascade event.
- The sum-energy E_{sum} deposited in all detectors for each cascade event.
- The multi-step cascade spectra (MSC) for each crystal multiplicity m_{cr}, which are the gamma-ray energy spectra for fully detected cascades.

The time of flight spectra give access to the resonance energy. Each resonance corresponds to a specific compound nucleus level populated after the neutron capture reaction and decaying to the ground state via an electromagnetic cascade. Inside these resonances we define a time window to create the other observables. In these spectra we note that there are no contaminations from other isotopes of uranium because the three samples have a high purity close to 100%. In addition, to reduce the dead time effect in the analysis of the data we decided to take only time windows with a counting rate below 0.20 counts/μs per pulse. On the other hand, the background subtraction has been estimated for each resonance from the spectra from neighbouring background regions after linear interpolation. This method fits very well the behaviour of the background in the spectra for the three uranium isotopes in all resonances used in this work. In the case of ^{234}U(n,γ) the background subtraction reproduces the contribution from the Ti isotopes due to the specific canning of this sample. In addition, the background can be largely removed from the spectra with a selection on the crystal multiplicity. The E_{sum} spectra for $m_{cr} = 1$ are expected to be dominated by the background below 2 MeV while for $m_{cr} \geq 2$ this background is almost subtracted. Finally, we compare some resonances with the same spin and parity, $1/2^+$, to consider possible fluctuations. The normalization of the spectra is done by the integral of E_{sum} with $m_{cr} \geq 2$ at the sum peak between $E_{sum} = 5.0 - 5.6$ MeV for ^{234}U(n,γ), $E_{sum} = 4.9 - 5.3$ for ^{236}U(n,γ) and $E_{sum} = 4.5 - 4.8$ MeV for ^{238}U(n,γ). These windows in the sum peaks are also used to create the MSC spectra and the crystal multiplicity distributions because we are only interested to study the cascade events in which all the gamma energy emitted from the sample is detected by the TAC. We can see some differences between resonances which are attributed to the Porter Thomas fluctuations in the primary intensity. These fluctuations are more obvious in the MSC spectra for $m_{cr} = 2$ because they are composed

by two transitions with a specific intensity. For an easy visualization of the experimental data we decided to show only the average spectra and its standard deviation which is representative of the Porter Thomas fluctuation.

The simulation codes used for the simulation of the gamma cascade are DICEBOX and FIFRELIN. The main goal of FIFRELIN is the simulation of the neutron/gamma emission in the fission process, so here we test the validity of this code for the modelling of the electromagnetic cascade by comparing with DICEBOX. These two codes simulate sets of levels produced from a level density formula and sets of random partial radiation widths, known as nuclear realizations. The partial radiation width for transitions between two levels following a random choice from Porter Thomas distribution is related with the PSF and the LD. The simulation of the set of levels by DICEBOX can be divided in two regions:

- The region below a certain critical excitation energy E_{crit} which is considered experimentally known, and the level energies, spins, parities, branching intensities of depopulating transitions, among others is taken from the ENSDF database.
- The region above E_{crit} where the level scheme is unknown and a full set of nuclear levels is calculated by a random discretization of an a priori known LD.

For FIFRELIN it is divided in three regions:

- The region below a certain excitation energy called $E_{cut-off}$ provided by RIPL-3 which is considered experimentally known, and all the information for the cascade simulation is taken from RIPL-3 database.
- The region between $E_{cut-off}$ and E_{bin} which corresponds to the energy limit in which the level density value by default is $5 \cdot 10^4$ MeV^{-1}. In this region known experimental levels are complemented by a LD formula.
- The region above E_{bin} where the level scheme is considered as a continuum and the discretization of the level is given by a LD.

Once created the nuclear realization, the transition to the next level is selected randomly until the ground state or an isomeric state is reached. In order to have enough statistics and to account for the Porter Thomas fluctuations we have to use in the simulation 20 nuclear realizations and 10^5 cascade events per realization. After the simulation of the gamma cascade we use GEANT4 for the simulation of the interaction and detection of these gamma rays with the TAC. In the GEANT4 simulation of the TAC we introduce the 40 BaF_2 crystals together with their photomultiplier tubes inside an aluminium housing, the two layers of neutron absorber materials, the aluminium beam pipes in vacuum, the sample holder in the middle of the TAC and the honey-comb structure that holds the complete assembly. Finally, in the event reconstruction we include the resolution of each detector, the threshold of 250 keV and the count rate effect (dead time and pile-up). The main objective is to be as close as possible to the real measurements.

Then, we compare the simulated spectra with the measured ones. The ^{234,236,238}U(n,γ) reactions have already been studied from different experiments in previous works. A combination of LD and PSF models and parameters can be taken from RIPL-3 database,

from the analysis of d- and ^{3}He-induced reactions on actinide targets performed at the Oslo Cyclotron Laboratory (OCL) and from the measurement of multi-step gamma-ray energy spectra from resonant neutron capture on uranium samples with DANCE calorimeter. The SLO model is used for the $M1$ PSF in the three analyses while the combination of LD and $E1$ PSF is not always the same. However, the most relevant differences between the three analysis are (i) the RIPL-3 database does not include the SC mode to describe the $M1$ PSF, (ii) the OCL introduces the SC mode and one more Lorentzian around 7 MeV called pygmy $E1$ resonance to define the $E1$ PSF, and (iii) the DANCE analysis remove that pygmy resonance and adjusts the parameters of $M1$ PSF to reproduce the experimental data. From the comparison between these three simulations with the experimental multiplicity distribution, E_{sum} spectra and MSC spectra we can conclude that the use of the SC mode to describe the $M1$ PSF is mandatory to reproduce the experimental data, especially the behaviour of the MSC spectra between 2 and 3.5 MeV. The best results were obtained with the DANCE parameters. However, none of the three simulations produced a good agreement in the calculation of the total radiation width Γ_γ (TRW) for the three uranium isotopes using the same parametrization. In addition, the only set of parameters of the $E1$ PSF that reproduce the trend of the experimental PSF (calculated with the photoabsorption cross section) from Caldwell for some uranium around the GEDR is given by RIPL-3. In the OCL analysis the PSF is overestimated because the parametrization includes the photofission cross section while for DANCE the PSF is underestimated because of a scaling factor of 0.5. On the other hand, the semi-microscopic models of the LD based on HFB plus combinatorial model and of the PSF from the D1M+QRPA calculations with non-zero limit at low E_γ shown a good agreement with the experimental data for ^{236}U(n, γ) while for ^{234}U(n, γ) and ^{238}U(n, γ) this is only achieved for $m_{cr} \geq 4$. For lower multiplicities, $m_{cr} \leq 3$, differences are clearly visible in the MSC spectra of these two uranium isotopes and improvements can still be done.

Taking into account all the results mentioned previously we study many PSF + LD combinations using different models and consistent parameters for the $E1$ PSF while for the $M1$ strength the parameters are adjusted to reproduce the n_TOF data. In addition, the simulations are guided by a coefficient of agreement which takes lower values for better reproduction of the experimental data. As an additional constraint we use the results of the Γ_γ to exclude some model combinations. Looking at the dependence with respect to LD, the TRW calculated with BSFG is always higher than when using the CT model. This behaviour is expected because BSFG increases the number of levels faster than CT below S_n. Moreover, the TRW showed a high sensitivity to the models of LD with similar behaviour. Regarding the PSF the value of Γ_γ increases for a higher strength of the PSF. Finally, we have to use the MGLO model with $k_0 = 1.8$ and T = 0.3 MeV for the PSF in combination with CT model for the LD to reproduce coherent values of TRW for the three uranium isotopes and a good agreement with the experimental spectra.

We have tested the validation of FIFRELIN for the modelling of the electromagnetic cascade. After checking all the default parameters used by FIFRELIN in the simulation we conclude that FIFRELIN should not use the default parameters from RIPL-3 of the PSF in order to reproduce the experimental data. In addition, we compare FIFRELIN

and DICEBOX using the same models and parameters for the PSF and LD. The results were similar with some little variations due to the use of different nuclear database (ENSDF for DICEBOX and RIPL-3 for FIFRELIN) to describe the low energy levels.

We studied also the sensitivity of the different parameters of the PSF and LD involved in the simulation. This exercise was limited to the case of the relative variation of the TRW to the parameters of the Lorentzians of the PSF in a range of 50%. When analysing the trends of the TRW values we observed that the simulations are more sensitive to changes of the E parameters than the Γ and σ parameters. In addition, for $E1$ PSF the most sensitive parameters correspond to the second Lorentzian while for $M1$ PSF they correspond to the first Lorentzian of the SC mode. For the parameters of the LD corresponding to the CT model we did a similar exercise by studying the relative variation of the s-wave spacing D_0. The results show a high sensitivity to the temperature parameter of the CT model.

Finally, we are interested to study the relationship between $M1$ and $E1$ PSFs. For that we study three simulations with different values of the k_0 parameter in the MGLO model. We found that a similar ratio $M1/E1$ is preserved when reproducing the experimental data. However, if the trend of the $E1$ model is very different the ratio $M1/E1$ will be also different.

Introduction

The main goal of this thesis work is the study of the statistiscal models describing the gamma decay and in particular the two main ingredients which are the photon strength function (PSF) and the level density (LD). The PSF, also called gamma ray or radiative strength function, was proposed in 60's by Bartholomew [1] following the Brink-Axel hypothesis [2] to bypass the extreme complexity to formulate the fundamental equations governing the gamma ray emission from an excited nucleus produced by non-relativistic nuclear reaction. Therefore, the PSF is a very useful simplified model to characterize the capacity of the nuclei to absorb or emit photons. However, the use of the PSF is only justified at high excitation energy when the number of radiation is large enough to observe it as a continuum spectrum, so even if the single transition information is lost we can predict some smooth, average properties of the gamma-ray spectrum.

The PSF is essential in the modelling of nuclear reactions involving electromagnetic excitation or deexcitation. From its introduction many experiments have been carried out on this topic. Firstly, photonuclear experiments and slow-neutron capture reaction were used for the study of the PSFs, although later other reactions using beams of different particles were analyzed – elastic and inelastic scattering of electrons, protons, photons and neutron at various energies. In addition, it was already well known that at high energy above the neutron separation energy S_n the gamma ray emission is dominated by electric dipole, $E1$, transitions presenting a giant resonance structure called giant electric dipole resonance (GEDR). The GEDR is produced by the collective dipole vibration of many nucleons which could be studied by measuring the photoabsorption cross section. According to the detailed-balance principle the knowledge of the PSF can be used as a connection point between the partial radiation width in the gamma ray emission and the photoabsorption cross section. A large number of authors have developed different models to define the PSF: ELO, GLO, MGLO, among others which are presented in Sec. 1.2. These models reproduce the experimental data at the peak of the GEDR but at low energy below S_n the trend of the models are very different as seen in Fig. 1. Regarding the PSF below the neutron separation energy S_n an important contribution of magnetic dipole, $M1$, transitions was predicted using the geometrical two-rotor model and the interacting boson model [3, 4]. This contribution were experimentally tested thanks to the high resolution inelastic electron scattering from rare-earth nuclei, experiment using the technique nuclear resonance fluorescence (NRF) [5], among other type of reactions. However, there is still a lack of knowledge of the PSF below S_n for some actinides.

On the other hand, the LD can be experimentally deduced at low energy where a detailed description of nuclear levels and transitions exists, and around S_n where level

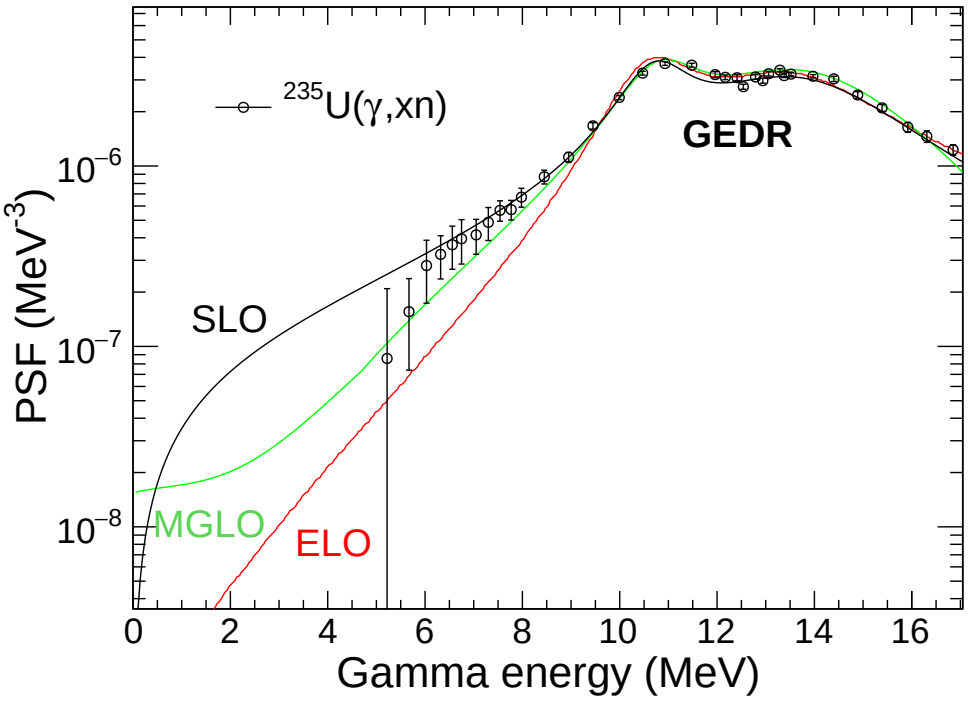

Figure 1: Comparison between different models of the $E1$ PSF.

mean spacing is known from neutron reactions. However, the exponential increase in the level density makes impossible the experimental study of high-energy levels due to the decreasing spacing between levels, so the use of statistical models at higher excitation energy is necessary. A wide variety of formulas were developed for the LD by fitting the experimental levels at low energy and at S_n which are shown in Sec. 1.1.

In this thesis work we study the PSF and LD through the gamma decay after a neutron capture reaction. The resonance structure above S_n has very narrow widths of the order of tenths of eV corresponding to the lifetime of the state $\approx 10^{-14}$ s. Therefore, the compound nucleus can be assumed in the first place as a remarkably stable system, so the subsequent decay by emission of particles or gamma rays must be considered as a process separated from the creation of the compound nucleus. When a neutron capture reaction takes place on a nucleus of mass A the resulting nucleus will have a mass $A+1$ with an excitation energy corresponding to the sum of the neutron binding energy S_n and the neutron kinetic energy E_n. In our case we study the ^{234,236,238}U(n, γ) reactions with low neutron energies up to a few tens of eV, so we can consider that the excitation energy is around S_n whose value are 5.30 MeV, 5.13 MeV and 4.80 MeV respectively. After the compound nucleus is created, it decays to the gound state via gamma cascades in the case of a radiative capture reaction. For actinides the number of levels and transitions is so high between the ground state and S_n, so the electromagnetic cascade results in a very complex spectrum. The number of gamma rays emited in the cascade is called multiplicity which typically varies between 1 and 8. All these gamma-ray spectra provide information about the PSF and LD.

The gamma cascade for the ^{234,236,238}U(n, γ) reactions were measured with the total absoption calorimeter (TAC) of the n_TOF collaboration at CERN, shown in Sec. 2.2. This facility allows to select the neutron resonances through the neutron time-of-flight technique while the high granularity of the TAC allows separating the different gamma rays from the same cascade for an accurate analysis. With this detector we can access to the different observables needed to study the PSF and the LD: the crystal multiplicity distribution, the sum energy spectra and the multi-step cascades introduced in Sec. 3.1.

The codes used for the simulation of the gamma cascades after a neutron capture reaction are DICEBOX and FIFRELIN presented in Sec. 1.3. These two codes model the characteristics of gamma cascades involving a large number of presumably unmeasured intermediate nuclear levels by using models of the PSFs and LD. In addition, GEANT4 is used for the simulation of the interaction of these gamma rays with the TAC materials. Through the comparison of the spectra resulting from the simulations with the experimental data we can obtain important information about the PSF and the LD.

The gamma decay of actinides was also studied in the charged-particle-induced experiments of the Oslo cyclotron laboratory, the LDs and PSFs were in particular deduced for the neighbouring odd isotope ^{237}U [6]. The analysis of gamma-rays spectra following resonance neutron capture on even-even uranium targets was also performed with the detector for advanced neutron capture experiments (DANCE) at Los Alamos neutron science center of Los Alamos national laboratory [7]. Both analyses revealed a significant contribution of low-lying $M1$ strength – the scissors mode (SC). The two SC resonances were found to be centered just above 2 MeV and just below 3 MeV, their deduced strengths however differ – they were found up to two times lower in the Oslo data [6] compared to the DANCE data [7] depending on the $E1$ PSF and LD models used in conjunction. The n_TOF total absorption calorimeter (TAC) data were previously analysed without considering the SC contribution [8]. The present study aims to perform a comprehensive analysis of the n_TOF data taking into account the latest experimental and theoretical results.

In summary this work allows a better knowledge and a validation of the PSF at low energy, and an improvement of the electromagnetic cascade modeling which are important for the simulation of the astrophysical nucleosynthesis [9, 10] and nuclear reactors [11].

Chapter 1

Nuclear de-excitation modelling

1.1 Nuclear level density models

The nuclear level density $\rho(E, J, \pi)$ is defined as the derivative of the number of levels characterized by a spin J and parity π with respect to a given energy E. It is one of the elements needed in model-based calculations of nuclear reaction cross sections and for the prediction of gamma decay at high excitation energies where discrete levels information is not available or incomplete. At low energy, approximately ~ 0.8 MeV for the actinides used in this work, the number of levels is small so the average spacing between levels is large. Therefore, it is assumed that this region is experimentally resolved and the nuclear level properties (quantum numbers and decay properties) are well known. As the excitation energy increases the level density is greater and consequently the spacing between levels is reduced, so its experimental study is more difficult resulting in a lack of information. The nuclear levels of this region are obtained from the discretization of a known level density formula which localy reproduces the energy spacing between the levels for a given spin and parity according to a Wigner distribution. Nevertheless, in the region just above the neutron separation energy S_n nuclear levels can be measured experimentally using the neutron time-of-flight method.

The level density formula is usually calculated as the product of three factors

$$\rho\left(E, J, \pi\right) = \rho_{tot}\left(E\right) \cdot f\left(E, J\right) \cdot g\left(\pi\right) \tag{1.1}$$

where $g\left(\pi\right)$ is the parity distribution, $f\left(E, J\right)$ the spin distribution, and $\rho_{tot}\left(E\right)$ is the total level density. In this work, the parity distribution is assumed to be equiprobable for the phenomenological formulas regardless of the excitation energy $g\left(\pi\right) = 1/2$ for positive and negative parities, while $f\left(E, J\right)$ was derived by Gilbert and Cameron [12, 13]:

$$\begin{aligned} f\left(E, J\right) &= \exp\left(-\frac{J^2}{2\sigma_c^2}\right) - \exp\left(-\frac{\left(J+1\right)^2}{2\sigma_c^2}\right) \\ &\approx \frac{2J+1}{2\sigma_c^2} \exp\left(-\frac{\left(J+1/2\right)^2}{2\sigma_c^2}\right) \end{aligned} \tag{1.2}$$

$f\left(E, J\right)$ can depend on E through the spin cut-off factor σ_c which can be constant or not as seen in following subsection. Finally, several models such as the constant temperature

(CT), the back-shifted Fermi gas (BSFG), and the composite Gilbert and Cameron (CGCM), among others have been developed for $\rho_{tot}(E)$ which will be described in the next subsections.

1.1.1 Constant temperature model

The constant temperature (CT) formula was proposed by Gilbert and Cameron [13]. For low excitation energies this formula describes the experimental data in a better way than other models. In addition, earlier in [14] it was observed that the CT formula can reproduce the level density near the neutron binding energy. It is based on the experimental evidence which showed that the number of levels increases according to an exponential formula $N(E) \sim \exp\left(\frac{E-E_0}{T}\right)$. Therefore, the level density function is given by

$$\rho_{tot}(E) = \frac{1}{T}\exp\left(\frac{E-E_0}{T}\right) \tag{1.3}$$

where E_0 is the backshift energy and T is the nuclear temperature which are adjusted to the experimetal discrete levels. T can be assumed to be nearly constant below few MeV of excitation energy, hence the name of the model. The spin cut-off factor for the CT model in ref. [15] has been fitted as a function of the mass number A only from a dataset of 310 nuclei

$$\sigma_c = 0.98 \cdot A^{0.29}. \tag{1.4}$$

In a later work [16] a new formula for the spin cut-off is introduced for a better description of experimental data

$$\sigma_c^2 = 0.391 \cdot A^{0.675}(E - 0.5P_a)^{0.312} \tag{1.5}$$

with re-evaluated values for the free parameters (E_0 and T). The parameter P_a is the deuteron pairing energy calculated from mass or mass excess values $M(A,Z)$ of the mass tables [17] with the formula:

$$P_a = \frac{1}{2}\left[M(A+2,Z+1) - 2M(A,Z) + M(A-2,Z-1)\right] \tag{1.6}$$

1.1.2 Back-shifted Fermi gas model

The origin of the back-shifted Fermi gas (BSFG) model lies in Bethe's work in 1936 [12]. Bethe used a method adopted from statistical physics and assumed that the knowledge of the partition function of a system is equivalent to the complete information on the spectrum of the system. The level density formula that Bethe derived considering a gas of non-interacting fermions was

$$\rho_{tot}(E) = \frac{\exp\left(2\sqrt{aE}\right)}{4\sqrt{3}E} \tag{1.7}$$

with a being the level density parameter.

A more realistic expression of this model is to consider that the fermions have a tendency to create pairs so an additional amount of energy is required to separate them.

This energy is taken into account introducing an energy backshift E_1 in the Bethe formula. That is why this approach is referred as BSFG model. The corresponding equation is

$$\rho_{tot}(E) = \frac{\exp\left(2\sqrt{a(E-E_1)}\right)}{12\sqrt{2}\sigma_c a^{1/4}(E-E_1)^{5/4}} \tag{1.8}$$

in which both E_1 and a are adjusted to experimental data. For the BSFG formula the spin cut-off parameter is energy dependent and is given from [13]

$$\sigma_c^2 = 0.0888A^{2/3}\sqrt{a(E-E_1)} \tag{1.9}$$

However, in ref. [15] the spin cut-off is given by another expresion which adjusts with adequate agreement the region at low excitation energy

$$\sigma_c^2 = 0.0146A^{5/3}\frac{1+\sqrt{1+4a(E-E_1)}}{2a} \tag{1.10}$$

Finally, eq. 1.5 is proposed in ref. [16] to describe the spin cut-off as used for the CT formula.

1.1.3 Shell effects for level density parameter and spin cut-off

So far the parameter a has only been considered energy independent. However, previous studies [18, 19] noted that in microscopic calculations of LD the damping of the shell effects appears at high excitation energy. To take into account this effect a parameter a is used which is energy dependent following the prescription of Ignatyuk [20]

$$a \equiv a(E,Z,A) = \tilde{a}(A)\left\{1+\frac{\delta W(Z,A)}{E-\Delta}\left[1-\exp\left(-\gamma(E-\Delta)\right)\right]\right\} \tag{1.11}$$

where $\tilde{a}(A)$ is the asymptotic level density value obtained when all shell effects are damped, γ is the damping parameter, $\delta W(Z,A)$ is the shell correction energy which reflects the difference between the experimental nuclear mass and the mass obtained by liquid drop formula, and Δ is the pairing shift based on the average pairing shift $\Delta = n\frac{12}{\sqrt{A}}$ where n= 0, 1 and 2 for odd-odd, odd-A and even-even nuclei, respectively. To apply eq. 1.11 at all excitation energies the limiting value for $E \leq \Delta$ is given by the first order Taylor expansion

$$\lim_{E-\Delta\to 0}(a(E)) = \tilde{a}\left[1+\gamma\delta W\right] \tag{1.12}$$

Within the RIPL-3 project [21] is also considered that the spin cut-off presents marked shell effects as well as parameter a. This effect can be taken into account by adopting the following expression [19]

$$\sigma_F^2(E) = 0.01389\frac{A^{5/3}}{\tilde{a}}\sqrt{a(E-\Delta)} \tag{1.13}$$

Analogous to the level density parameter a, for small excitation energies $E \leq \Delta$ the spin cut-off can be determined when the discrete levels are known, or is given by the systematic equation:

$$\sigma_d^2 = \left(0.83A^{0.26}\right)^2 \tag{1.14}$$

The functional form that is used in RIPL-3 for spin cut-off parameter is a linear combination between σ_d^2 and $\sigma_F^2(E)$. Defining E_d as a energy at the mid-point of a region where the total level density agrees well with the discrete level scheme, it is assumed

$$\sigma_c^2(E) = \begin{cases} \sigma_d^2 & \text{for } 0 \leq E < E_d \\ \sigma_d^2 + \frac{E-E_d}{S_n-E_d}\left[\sigma_F^2(S_n) - \sigma_d^2\right] & \text{for } E_d \leq E < S_n \\ \sigma_F^2(E) & \text{for } E \geq S_n \end{cases} \tag{1.15}$$

where the matching point is chosen to be the neutron separation energy S_n of the nucleus under consideration.

1.1.4 Composite Gilbert and Cameron model

Gilbert and Cameron [13] proposed a model (CGCM) which is a combination between CT and BSFG formulas. The CGCM uses the CT formula at low energy because it best describes the experimental levels up to certain energy E_x above which BSFG is used for a better reproduction of the level density at S_n. The E_x is the point of tangency between both LD formulas. In the original formula E_x is given by the systematic expression:

$$E_x = 2.5 + \frac{150}{A} + P(Z) + P(N) \quad (MeV) \tag{1.16}$$

while σ_c is given by eq. 1.9. However, there are more complicated calculation schemes for E_x in the RIPL-3 project and CGCM uses the parameters a and σ_c described in previous subsection.

1.1.5 Microscopic level density

When experimental data are not available and extrapolation from the experimentally known region is not reliable we have to use preferably microscopic and semi-microscopic global predictions of the LD. The microscopic method used in this work to describe the LD is the combinatorial method [22] which is capable to compete with phenomenological LD. Nowadays, this method accounts for pairing correlations when a pair of nucleons is broken and it assumes that once a pair has been broken the pairing correlations vanish. The LD obtained uses the single-particle level scheme from axially symmetric Hartree-Fock-Bogoliubov (HFB) model to create incoherent particle-hole state densities. The final energy, spin and parity are calculated adding the contribution of rotational and vibrational enhancements and the disappearence of deformation effects at high energies [23, 24].

Since these microscopical level densities have not been adjusted to experimental data, one may add adjustment flexibility through a scaling function [25]

$$\rho(E, J, \pi) = \exp\left(C\sqrt{E-\delta}\right)\rho_{HFB}(E-\delta, J, \pi) \tag{1.17}$$

where ρ_{HFB} is the microscopic LD, δ is the pairing shift to obtain the LD from values tabulated at other energies, and the parameter C plays the same role as the level density parameter a introduced in the phenomenological models.

1.1.6 Comparison of level density models

In the literature there is a great variety of LD models. A part of them has been shown in the previous subsections where the formulas for LD depending on the excitation energy range, parameter a, spin cut-off σ_c and pairing energy chosen. In this work and for simplicity we focus the analysis on these LD formulas. Henceforth, to differentiate CT and BSFG formulas from different sources we call VE05 from ref. [15] and VE09 from ref. [16] while the CGCM model is that given by the eq. 1.11 and 1.15 considering shell effects for a and σ_c.

The phenomenological LD models for a given spin and parity $1/2^+$ are shown in Fig. 1.1 above a critical energy explained in Sec. 1.3.1 from which the experimental data are no longer comprehensive. Some small differences are observed in the trends between LDs from VE05 and VE09, especially for CT which are related to the different σ_c. The CGCM model is equivalent to the CT formula because the E_x are close to S_n ($E_x > S_n - 2$ MeV). On the other hand, table. 1.1 shows that the different models reproduce with reasonable precision the average level spacing D_0 of s-waves whose values are calculated by $1/\rho(S_n, 1/2, +)$ which depends strongly on the spin cutoff factors. We note that BSFG and CGCM reproduce better the evaluated D_0 than CT, while the semi-microscopic model are in a good agreement with the evaluated values of the three uranium isotopes.

Table 1.1: s-wave average level spacing D_0 for n + ^{234}U, n + ^{236}U and n + ^{238}U calculated for different LD formulas.

	D_0 (eV)		
Model	n + ^{234}U	n + ^{236}U	n + ^{238}U
CT VE05	10.7	12.5	23.6
CT VE09	11.7	11.9	18.3
BSFG VE05	12.0	14.8	20.5
BSFG VE09	12.1	14.9	20.8
CGCM	12.0	15.0	20.8
HFB	11.2	16.9	18.4
Evaluated [16, 26]	12.0(8)	15(1)	20.8(3)

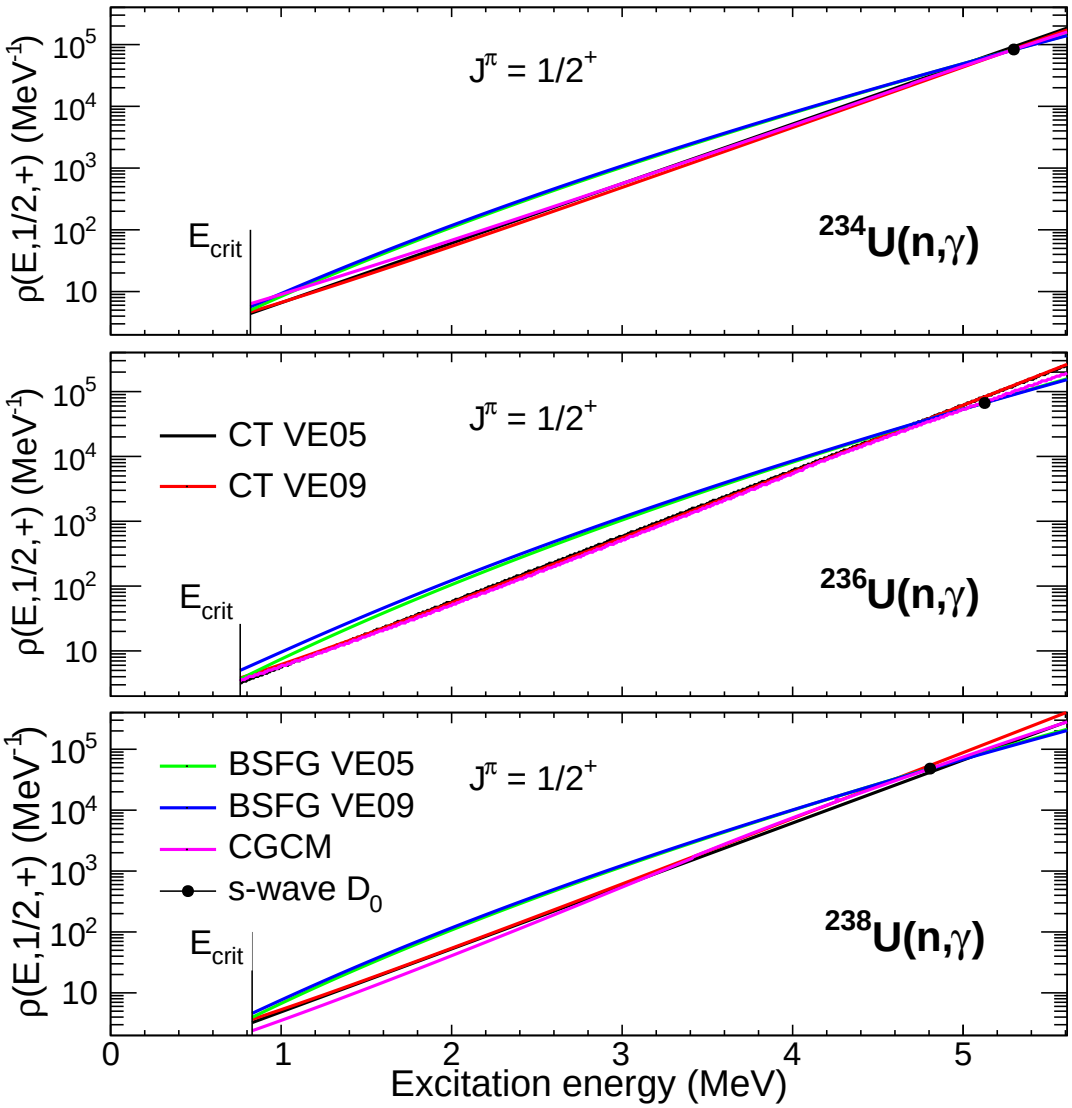

Figure 1.1: LD for spin and parity $1/2^+$ for n + ^{234}U (top), n + ^{236}U (middle) and n + ^{238}U (bottom) according to CT, BSFG and CGCM models. The point corresponds to the evaluated s-wave resonance density $1/D_0$. The parameter E_{crit} is the energy above which a LD model is used in the simulations of this work.

1.2 Photon strength functions

The electromagnetic transitions of an excited nucleus from an initial level defined by (E_i, J_i, π_i) to any accessible final state (E_f, J_f, π_f) are controled by the following selection rules. The photon emitted with a energy $E_\gamma = E_i - E_f$ can be of type X, where X = E electric or X = M magnetic, and multipolarity L. The accessible multipolarities in a transition from spin $J_i \rightarrow J_f$ are determined by

$$| J_f - J_i | \leq L \leq | J_f + J_i |$$

while the parities in the transition $\pi_i \rightarrow \pi_f$ satisfy the rules:

- $\pi_i\pi_f = (-1)^L$ for electric transition.
- $\pi_i\pi_f = (-1)^{L+1}$ for magnetic transition.

The probability of a XL transition is determined by the partial radiation width [27]

$$\Gamma_{i\gamma f}^{XL} = \frac{8\pi(L+1)}{L[(2L+1)!!]^2}\left(\frac{E_\gamma}{\hbar c}\right)^{2L+1} B(XL)\downarrow \tag{1.18}$$

Here $\hbar$ is the reduced Planck constant and c is the speed of light. $B(XL)\downarrow$ is the reduced transition probability for desexcitation of the nucleus

$$B(XL)\downarrow = \frac{|\langle i||M^{XL}||f\rangle|^2}{2J_i+1} \tag{1.19}$$

where $\langle i|$ and $|f\rangle$ are the wavefunctions of the inital and final states, while M^{XL} is the electromagnetic transition operator.

At high excitation energy when the level density becomes significantly high, the average partial radiation width $\overline{\Gamma}_{i\gamma f}^{XL}$ is used. It is estimated from the Fermi's golden rule that the average reduced transition probability $\overline{B}_{if}^{XL}$ is inversely proportional to the LD of the initial state. This assumption reflects that around E_i the sum of transition rates is constant independently of the number of levels. The photon strength function (PSF) is defined as a function of the average partial radiation width and it is dependent on the transition energy E_γ:

$$f^{XL}(E_\gamma) = \frac{\overline{\Gamma}_{i\gamma f}^{XL}\ \rho(E_i, J_i, \pi_i)}{E_\gamma^{2L+1}} \tag{1.20}$$

The PSF characterizes the average electromagnetic properties of excited nuclei and represents the distribution of the average transition probability between levels. It is an essential tool for applied nuclear reaction model calculations. The PSF can be expressed according to the electromagnetic transition operator M^{XL} as $E1$ referred to the electric dipole PSF, $M1$ referred to the magnetic dipole PSF and $E2$ referred to the electric quadrupole PSF.

The simplest model of the PSF is the single particle model in which the PSF is a constant independent on transition energy E_γ. The reduced transition probability $B(XL)\downarrow$ can be related to the lowest multipolarity transitions of the PSF from

$$\begin{aligned}
&\overline{B}(E1) = \tfrac{1}{\triangle}\textstyle\sum_{\triangle} B(E1)\ [\mathrm{e^2fm^2}] = 0.956\times10^6 f^{E1}[\mathrm{MeV^{-3}}] \\
&\overline{B}(M1)\tfrac{1}{\triangle}\textstyle\sum_{\triangle} B(M1)\ [\mu_N^2] = 86.6\times10^6 f^{M1}[\mathrm{MeV^{-3}}] \\
&\overline{B}(E2)\tfrac{1}{\triangle}\textstyle\sum_{\triangle} B(E2)\ [\mathrm{e^2fm^4}] = 1.25\times10^{12} f^{E2}[\mathrm{MeV^{-5}}]
\end{aligned} \tag{1.21}$$

where the summations are performed over an energy interval $\triangle$. In addition, it is frequent to compare the PSF for electromagnetic transitions from a bound state to

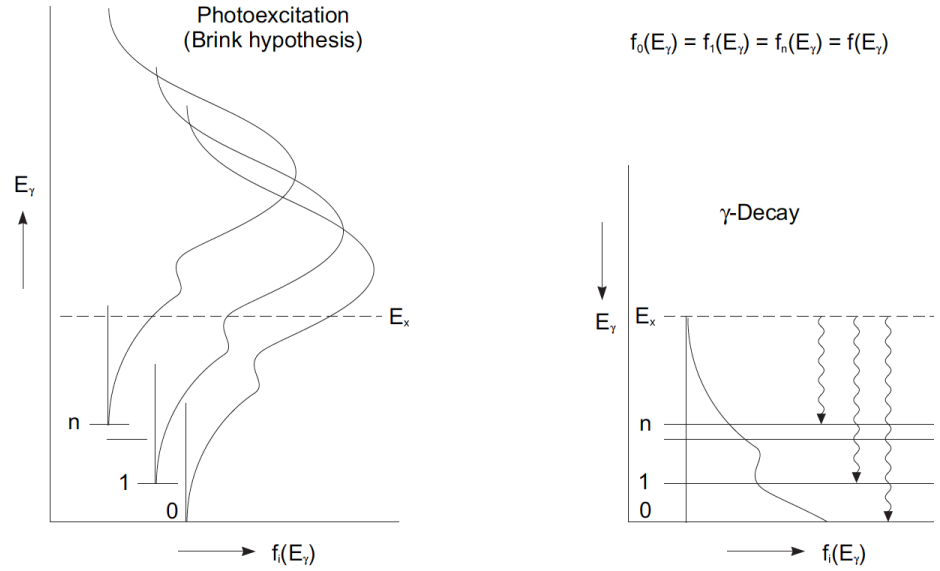

Figure 1.2: Schematic representation of the Brink hypothesis for photoexcitation and gamma decay of an excited nucleus, for example after neutron capture [28].

ground state with the Weisskopf estimates of the $B(XL)\downarrow$ to have an evaluation of the fragmentation of the transition strength.

According to the detailed-balance principle, there is a relation between photoemission characterized by the partial radiation width $\Gamma^{XL}_{i\gamma f}$ and photoabsorption cross section $\sigma^{XL}_{f\gamma i}$. The relation is given by

$$\Gamma^{XL}_{i\gamma f} = \frac{E_\gamma^2}{(\pi\hbar c)^2}\frac{2J_f+1}{2J_i+1}\sigma^{XL}_{f\gamma i} \tag{1.22}$$

Based on the idea that collective vibrations are independent of the intrinsic nuclear motion, Brink [2] assumed that the photoabsoption cross section depends only on the E_γ of the photon emitted in the XL transitions and it is independent of the properties of the initial state. As a consequence, the total photoabsorption cross section σ^{XL}_T depends only on the transition energy E_γ. This assumption is called the Brink-Axel hypothesis. A schematic representation is shown in Fig. 1.2. Now the average partial radiation width $\overline{\Gamma}^{XL}_{i\gamma f}$ and the total photoabsorption cross section $\overline{\sigma}^{XL}_T$ are considered. The detailed-balance principle can be written as

$$\overline{\Gamma}^{XL}_{i\gamma f}(E_\gamma)\ \rho(E_i, J_i, \pi_i) = \frac{E_\gamma^2}{(\pi\hbar c)^2}\frac{\overline{\sigma}^{XL}_T(E_\gamma)}{2L+1} \tag{1.23}$$

From eq. 1.20, the left hand side of eq. 1.23 is equal to $f^{XL}(E_\gamma)\ E_\gamma^{2L+1}$ and hence

$$f^{XL}(E_\gamma) = \frac{1}{(\pi\hbar c)^2}\frac{\overline{\sigma}^{XL}_T(E_\gamma)}{(2L+1)E_\gamma^{2L-1}} \tag{1.24}$$

Finally, the PSF can be obtained through experimental information of $\overline{\Gamma}^{XL}_{i\gamma f}$ in which the level density is always needed or $\overline{\sigma}^{XL}_T$ from photon-induced reactions, and on the contrary, the knowledge of the PSF can be used to estimate the values of $\overline{\Gamma}^{XL}_{i\gamma f}$ and $\overline{\sigma}^{XL}_T$.

1.2.1 Nature of the photon strength function

The PSF can be deduced from measurements of the total photoabsorption cross section. Baldwin and Klaiber [29] showed that a broad resonance dominates the photoabsorption cross section above the neutron separation energy S_n. This resonance is explained by collective vibrations of neutrons and protons with opposite phase induced by the electric field of the incoming radiation. This motion with dipole character was called giant electric dipole resonance (GEDR).

The photoabsorption experiments are usually restricted to the energy region above S_n where the GEDR is located. Therefore, the PSFs are not well known below S_n and theoretical models have to be proposed. However, the GEDR is not the only possible collective vibration. It depends if the nucleons vibrate in phase (isoscalar) or out of phase (isovector), and if nucleons with spin up ($\uparrow$) and spin down ($\downarrow$) vibrate in the same direction (electric) or against (magnetic) following a multipole pattern. The resonance can be classified as giant magnetic dipole resonance (GMDR), giant electric quadrupole resonance (GEQR) and so on.

1.2.2 Electric dipole photon strength function

The GEDR is produced when most of the nucleons of a nucleus move together. There are two macroscopic models of the motion in GEDR. One of the macroscopic model was developed by Steinwedel and Jensen [30]. This model describes protons and neutrons as two fluid liquid within a fixed surface. The GEDR consists in a vibration of proton against neutron fluid and the restoring force is proportional to the density gradient of those fluids. For this model the centroid energy of the resonance depends on mass number following $A^{-1/3}$ dependence. The other model was proposed by Goldhaber and Teller [31]. The GEDR is considered as an oscillation of protons and neutrons against each other in two different incompresible spheres. The restoring force is proportional to the nuclear surface area. For this model the excitation energy of the resonance is proportional to $A^{-1/6}$. However, the results of many years of experimental work [32] on the GEDR shows that the centroid energy is roughly given by

$$E_c = 31.2A^{-1/3} + 20.6\ A^{-1/6} \quad \text{MeV} \tag{1.25}$$

so the real GEDR is probably a mixture of the two models presented before.

On the other hand, the integration of the photoabsorption cross section that belongs to GEDR is expected to satisfy the Thomas-Reiche-Kuhn sum rule [33]

$$\int_{E_{min}}^{E_{max}} \sigma_T^{E1}\ dE \cong \frac{60NZ}{A}(1+\kappa) \quad \text{MeV mb} \tag{1.26}$$

where κ is a factor due to meson-exchange contributions which takes the values $\kappa = 0.1 - 0.3$ for nuclei with $A > 100$ when E_{min} is the binding neutron energy S_n and $E_{max} = 25$ MeV. It is assumed that the statistical decay of neutron capture gamma cascades starting from an excitation energy above 5 MeV is dominated by the E1 PSF resulting from the GEDR.

The shape of the E1 PSF for deformed nuclei is usually described by a sum of two standard Lorentzians [34], as a consequence of vibration modes along the symmetry axis and perpendicular to it. This is known as standard Brink-Axel Lorentzian model (SLO) [2, 35]. The Lorentz form of $\overline{\sigma}_T^{XL}$ is assumed in eq. 1.24 and the PSF is given by

$$f_{SLO}^{E1}(E_\gamma) = \frac{1}{3(\pi\hbar c)^2} \sum_{i=1}^{2} \frac{\sigma_{G_i} E_\gamma \Gamma_{G_i}^2}{\left(E_\gamma^2 - E_{G_i}^2\right)^2 + E_\gamma^2 \Gamma_{G_i}^2} \tag{1.27}$$

where the parameters E_G, Γ_G, σ_G are the energy, width and cross section of the GEDR. This model depends only on E_γ. However, the SLO model is inadequate at energies below the neutron binding energy [36].

The problem of the behaviour at low energy was solved using the Fermi liquid theory of finite systems [37] and considering microscopic properties of the GDR. Kadmenskii, Markushev and Furman (KMF) [38] emphasized that $E_\gamma \to 0$ limit of the Lorentzian function is unjustified. In addition, they proposed that the width Γ_T of the GEDR should depend on E_γ and the nuclear temperature T of the state due to quasiparticle collisions

$$\Gamma_T\left(E_\gamma, T\right) = \frac{\Gamma_G}{E_G^2}\left(E_\gamma^2 + 4\pi^2 T^2\right) \tag{1.28}$$

The nuclear temperature of the final level is given in this work by the expression

$$T = \sqrt{\frac{E_f - P_a}{a}} \tag{1.29}$$

where E_f is the energy of the final state in the transition and P_a and a is the deuteron pairing energy and the level density parameter introduced in Sec. 1.1.2.

The KMF model incorporates the above described features and the E1 PSF reads

$$f_{KMF}^{E1}(E_\gamma, T_f) = \frac{1}{3(\pi\hbar c)^2} F_k \sum_{i=1}^{2} \sigma_{G_i} \Gamma_{G_i} \frac{E_{G_i} \Gamma_{T_i}}{\left(E_\gamma^2 - E_{G_i}^2\right)^2} \tag{1.30}$$

where the dimensionless Fermi liquid parameter F_k takes the value 0.7 [38]. The shape of KMF model achieves a reasonable agreement with spherical nuclei [39]. However, this model diverges at $E_\gamma = E_G$ so it is not applicable near the peaks of GEDR.

A variation used by Kopecky et al. [40, 41] called Lorentzian with energy dependent width (ELO) includes in the SLO model the width $\Gamma_T(E_\gamma, T)$ and E1 PSF is given by

$$f_{ELO}^{E1}(E_\gamma) = \frac{1}{3(\pi\hbar c)^2} \sum_{i=1}^{2} \sigma_{G_i} \Gamma_{G_i} \frac{E_\gamma \Gamma_{Ti}}{\left(E_\gamma^2 - E_{G_i}^2\right)^2 + E_\gamma^2 \Gamma_{Ti}^2} \tag{1.31}$$

There are some models similar to the KMF and ELO models but with a width $\Gamma_T(E_\gamma, T)$ that depends on the temperature in different ways, for instance the modified Lorentzian (MLO) [21, 42], the generalized Fermi liquid (GFL) [43] and the hybrid model [44]. However, in this work these models are not used.

An empirical model called generalized Lorentzian (GLO) [41, 45] was proposed to correct the difficulties in both low energy and GEDR energy in spherical nuclei. Therefore, the GLO model is valid over the whole region of gamma-ray energy. The E1 PSF has the functional form

$$f^{E1}_{GLO}(E_\gamma, T) = \frac{1}{3(\pi\hbar c)^2}\sum_{i=1}^{2}\sigma_{G_i}\Gamma_{G_i}\left[\frac{E_\gamma\Gamma_{T_i}}{\left(E_\gamma^2 - E_{G_i}^2\right)^2 + E_\gamma^2\Gamma_{T_i}^2} + F_k\frac{4\pi^2T^2\Gamma_{G_i}}{E_{G_i}^5}\right] \tag{1.32}$$

The function connects the KMF model at low energy with the ELO model for energy near to the GEDR. The GLO model takes into account a nonzero limit of the E1 PSF when $E_\gamma \to 0$ and $T \neq 0$, and it does not diverge at $E_\gamma = E_G$.

To solve the difficulty with deformed nuclei, a phenomenological modification of the width of eq. 1.28 was proposed by Kopecky et al. [45]. This model is referred as the enhanced generalized Lorentzian (EGLO) and the E1 PSF is given by

$$f^{E1}_{EGLO}(E_\gamma, T) = \frac{1}{3(\pi\hbar c)^2}\sum_{i=1}^{2}\sigma_{G_i}\Gamma_{G_i}\left[\frac{E_\gamma\Gamma'_{T_i}}{\left(E_\gamma^2 - E_{G_i}^2\right)^2 + E_\gamma^2\Gamma_{T_i}^{\prime 2}} + F_k\frac{\Gamma'_{T_i}(E_\gamma = 0, T_f)}{E_{G_i}^3}\right] \tag{1.33}$$

with empirical factors k_0 and E_0 introduced into the width formula

$$\Gamma'_T(E_\gamma, T) = \left[k_0 + (1-k_0)\frac{E_\gamma - E_0}{E_G - E_0}\right]\frac{\Gamma_G}{E_G^2}\left(E_\gamma^2 + 4\pi^2T^2\right) \tag{1.34}$$

where $E_0 \approx 4.5$ MeV [46] and the parameter k_0 is recommended to be a function of mass number A and is strongly correlated to the level density. For BSFG model it has the form

$$k_0 = \begin{cases} 1.0 & \text{for } A < 148 \\ 1.0 + 0.09(A-148)^2\exp\left[-0.18(A-148)\right] & \text{for } A \geq 148 \end{cases} \tag{1.35}$$

while for CT it has the form

$$k_0 = \begin{cases} 1.5 & \text{for } A < 145 \\ 1.5 + 0.131(A-145)^2\exp\left[-0.154(A-145)\right] & \text{for } A \geq 145 \end{cases} \tag{1.36}$$

However, k_0 is a free parameter which can take any value. Another generalized model denoted as modified generalized Lorentzian (MGLO) was introduced in ref. [47]. MGLO differs from EGLO in the second term on the right hand of eq. 1.33 which describes the behaviour at very low energy. MGLO assumes a factor $k_0 = 1$ in this second term, so the formula is the same as GLO in eq. 1.32 but using the width formula of eq. 1.34 for the first term.

1.2.3 Magnetic dipole photon strength function

The gamma decay of excited nuclear states above S_n is dominated by the E1 PSF so there is not much information about other types of decay. However, below S_n the decay

in actinide nuclei is influenced by the magnetic dipole (M1) transition and for which experimental information are available.

The values of f^{M1} were estimated from average resonance capture (ARC) measurements [48, 49, 50] of primary γ-transitions after capture reaction and taking an average of partial radiation width over a high number of resonances to take into account the fluctuations of the partial radiation width around the expected value. Collective excitations (GMDR) were found, so a good description of the M1 PSF at excitation energies below S_n can be made considering two types of excitation: the spin-flip mode (SF) and the scissors mode (SC).

The SF mode is interpreted in the liquid drop model as nucleons oscillating in phase or in opposite phase. For this vibration mode a Lorentzian shape given by SLO model in eq. 1.27 is assumed. Experimental results of the SF mode corresponding to the M1 PSF were obtained for some rare-earth nuclei in different works [40, 45, 51, 52]. The results show a position of the center of the resonance shifts as $E_{SF} \approx 41A^{-1/3}$ and a width of $\Gamma \approx 4$ MeV.

The SC mode describes a small amplitude rotation of the neutrons against the protons. It was predicted using the geometrical two-rotor model and the interacting boson model [3, 4]. The experimental observation of this mode was made thanks to high resolution inelastic electron scattering from rare-earth nuclei [53, 54]. Another method called nuclear resonance fluorescence (NRF) in which a (γ, γ') reaction takes place is specially useful to locate low lying M1 PSF because of its high sensitivity [5]. NRF studies of individual transition to ground state allow to obtain information about intensities and transition strengths $B(XL)\downarrow$ on some gamma energy intervals. This type of experiment on well deformed even-even rare-earth nuclei usually resulted in a total M1 strength approximately of $3\mu_N^2$ which is proportional to the square of the nuclear deformation δ and the energy center E_{SC} is close to 3 MeV. NRF analysis were performed for some uranium isotopes [55, 56, 57]. The results for ^{238}U showed a strong contribution of $M1$ states around 2.5 MeV with a total strength of $8\mu_N^2$ which doubles the approximated valued for rare-earth nuclei. The ^{236}U showed also a $M1$ distribution concentrated at $\approx$2.22 MeV and $\approx$2.5 MeV with a total $\sum B(XL)\downarrow = 2.94 \pm 0.3\mu_N^2$, while for ^{235}U a $M1$ strength was estimated from 1.6 to 3.0 MeV with the peak located at 1.8 MeV with a total $\sum B(XL)\downarrow = 0.3\mu_N^2$ which is much smaller than expected. Because of all these differences it is not clear that NRF measurements provide an adequate characterization of the SC mode.

The SC mode was observed also in reactions $(d, p\gamma)$, $(d, d'\gamma)$, $(d, t\gamma)$, among others. The isotopes ^{237,238,239}U were studied with these reactions in ref. [6] using the Oslo method. The outgoing charged particle is measured to obtain the excitation energy of the compound nucleus and with an iterative subtraction technique called "Oslo method" the primary gammas are extracted. Briefly, the method consists in generating a first generation matrix which expresses the probability of the transition gammas which is connected to the LD and PSF. They showed a SC mode centred at energies around 2 MeV and 2.9 MeV and a total M1 strength $\approx 9\mu_N^2$. Futhermore, the SC mode has been studied using gamma cascades after a neutron capture reaction [7, 58]. For ^{234,236,238}U(n, γ) reactions the SC mode was represented by two Lorentzians near to 2.15 MeV and 2.9 MeV. The introduction of the SC mode was essential for a better

representation of the shape of the gamma-ray spectra.

1.2.4 Electric quadrupole photon strength function

Despite the fact that the dipole transitions dominates the gamma decay of a nucleus, the electric quadrupole ($E2$) transitions might give a small contribution in the cascade after a neutron capture reaction. Even if the $E2$ strength is not extremely strong some effect will be noticed. The information of the $E2$ strength comes mainly from the cross section of inelastic scattering of charged particles bacause it contains multipole matrix elements [59]. The $E2$ strength is interpreted as isoscalar giant quadrupole electric resonance (GEQR) which corresponds to surface oscillation of neutrons moving together with protons. Sometimes the $E2$ PSF is approximated by the single-particle model where f^{E2} is a constant, but in this work we use the SLO model with a single Lorentzian as recommended in ref. [46]. The parameters of the GEQR are calculated from

$$E_G = 63\ A^{-\frac{1}{3}} \qquad \text{(MeV)} \tag{1.37}$$

$$\Gamma_G = 6.11 - 0.021\ A \qquad \text{(MeV)} \tag{1.38}$$

$$\sigma_G = 0.00014 \frac{Z^2 E_G}{A^{1/3}\Gamma_G} \qquad \text{(mb)} \tag{1.39}$$

Anyway, note that the contribution of $E2$ PSF under these conditions does not affect our results.

1.2.5 Microscopic photon strength function

As for LD the microscopic and semi-microscopic models for PSF are very important for a safe extrapolation to regions where there are no experimental data. A lot of works [60, 61, 62] were dedicated to the calculation of microscopic $E1$ and $M1$ PSFs. They were derived from quasiparticle random phase approximation (QRPA) method. However, most of these QRPA calculations assumed spherical symmetries and some phenomenological corrections were needed to reproduce the experimental data where effects beyond the particle-hole excitations and phonon coupling are taken into account [63, 64, 65]. For the isotopes studied in this work semi-microscopic models for both $E1$ and $M1$ PSFs are available from QRPA calculations based on HFB calculations using the finite-range D1M Gogny interaction [61, 66, 67].

To consider in the semi-microscopic D1M+QRPA model [68] the effects beyond the particle-hole excitations, an energy shift is included for both $E1$ and $M1$ PSFs that increases with the energy. The renormalization procedure to reproduce both the experimental GDR properties and low-energy vibrational states consists in an energy shift of $\Delta = 0.5$ MeV for $E_\gamma \leq 0.5$ MeV, $\Delta = 2.5$ MeV for $E_\gamma = 18$ MeV and $\Delta = 5$ MeV for $E_\gamma \geq 21$ MeV connected by a linear interpolation. In addition, the empirical damping of the collective motions is introduced by folding the D1M+QRPA PSF with a SLO function with the broadening width Γ_{X1}. For the $E1$ PSF the width Γ_{E1} has been adjusted on photoabsorption data and it is assumed to depend only on the atomic mass A. More specifically $\Gamma_{E1} = 7 - A/45$ MeV for $A \leq 200$ and $\Gamma_{E1} = 2.5$ MeV otherwise. For the $M1$ PSF a constant value of $\Gamma_{M1} = 0.5$ MeV was adopted [67].

Nowadays, it is well accepted that PSF may differ from photoabsorption data at low E_γ. The final expresions for $E1$ and $M1$ PSFs include a non-zero limit given by [69]:

$$f^{E1}(E_\gamma) = f^{E1}_{QRPA}(E_\gamma) + \frac{f_0 E_i}{1 + e^{(E_\gamma - E_0)}} \tag{1.40}$$

$$f^{M1}(E_\gamma) = f^{M1}_{QRPA}(E_\gamma) + Ce^{-\eta E_\gamma} \tag{1.41}$$

where $f^{X1}_{QRPA}(E_\gamma)$ is the D1M+QRPA dipole strength. The second part is related with the phenomenological non-zero limit at low E_γ where E_i is the excitation energy of the decaying state and f_0, η, E_0 and C are free parameters. These free parameters are adjusted using the shell model calculations [70, 71, 72] and available experimental data at low E_γ such as the ones obtained with the Oslo method [73, 74, 75], or the average radiative widths [21].

1.2.6 Comparison of photon strength function models

As we saw in previous subsections, there is a wide variety of models to define the PSFs. In addition, depending on the region of E_γ the strength of specific XL transitions dominates the total gamma strength. Fig. 1.3 (top) shows the behaviour of the models SLO, ELO, GLO, and MGLO and EGLO with $k_0 = 2.5$ for the $E1$ PSF. The set of parameters for each model was chosen to adjust the experimental value at GEDR (9 MeV – 16 MeV) from Caldwell et al. [76] for ^{235,236,238}U(γ,xn) because at lower energy the behaviour of each uranium isotope presents considerable differences. The KMF model given by eq. 1.30 is not included because it diverges when $E_\gamma = E_G$ so you can not reproduce the experimental value at GEDR. We can observe that all models reproduce in a similar way the experimental data near the peak of the GEDR. However, the trend of each model presents great differences at lower energies, below S_n. Finally, a comparison of the strength between the $M1$ PSF using the SLO model and the $E1$ PSF using the MGLO model with $k_0 = 1.8$ and $T = 0.3$ MeV with parameters taken from table 3.4 is shown in Fig. 1.3 (bottom). The $E1$ PSF dominates at the peak of the GEDR while the $M1$ PSF is stronger around the energies where the SC mode is located. We compare also the behaviour of these phenomenological models with the semi-microscopic model for the PSFs. We can see that the trends of these two kind of models are different at low energy, and the intensity of the $M1$ PSF is higher with respect to the $E1$ PSF in the phenomenological case around the SC mode.

1.3 Simulation of capture cascades

A code known as DICEBOX was developed by F. Bečvář in 1998 [77]. The aim of this code was to simulate nuclear gamma cascades using the Monte-Carlo method. The main advantage of DICEBOX is the full quantitative control of the Porter Thomas fluctuations (PTF) in individual transition intensities which are assumed to follow a χ^2 distribution with one degree of freedom. DICEBOX has become a good tool for the description of gamma decay, for intance after a thermal neutron capture reactions, and it has been used in many works for different purposes [47, 78].

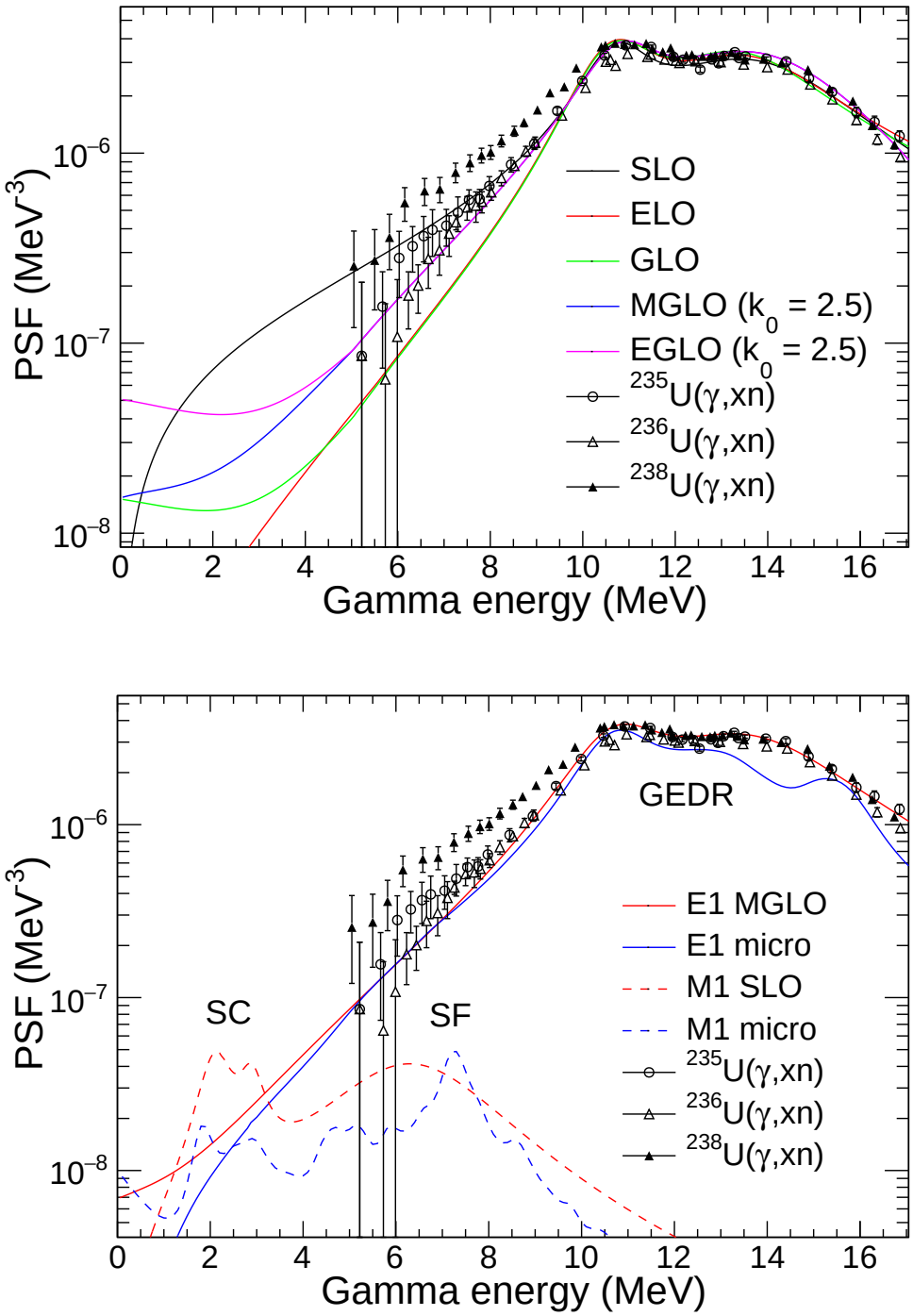

Figure 1.3: Comparison of different models for the $E1$ PSF for the uranium isotopes studied in this work from the ^{234,236,238}U(n, γ) reactions (top). The different symbols correspond to the experimental values from Caldwell et al. [76]. Comparison between the phenomenological models given by MGLO model with $k_0 = 1.8$ and $T = 0.3$ MeV for $E1$ PSF and SLO model for $M1$ PSF with the semi-microscopic model in the whole range of energy (bottom).

In this work we used an updated version of DICEBOX code by M. Krtička and S. Valenta [79] and another code called FIFRELIN [80, 81] developed at CEA Cadarache which is also based on the algorithm proposed by F. Bečvář but used in the simulation of the fission process (the cascade is extended to the neutron/gamma coupled emission).

1.3.1 DICEBOX

DICEBOX is based on the validity of the statistical model. It models the characteristics of gamma cascades involving a large number of presumably unmeasured intermediate nuclear levels in medium and heavy nucleus. To describe the gamma decay for a transition from initial level i to final level f with an emission of a gamma ray with energy $E_\gamma = E_i - E_f$, it is necessary to know the partial width Γ_{if}^{XL} expressed in eq. 1.43. In addition, it is well known that the partial radiation width presents very strong fluctuations around the expected value $\overline{\Gamma}_{i\gamma f}^{XL}$. These fluctuations can be described by the Porter Thomas distribution [82]. The probability density function for this distribution is expressed by the equation

$$P(x)dx = \frac{1}{\sqrt{2\pi x}} \exp\left(-\frac{x}{2}\right) dx \qquad \text{where} \quad x = \Gamma_{i\gamma f}^{XL}/\overline{\Gamma}_{i\gamma f}^{XL}. \tag{1.42}$$

The following assumptions have to be mentioned :

- The region below a certain critical excitation energy E_{crit} is considered experimentally known (all the level energies, spins, parities and branching intensities of depopulating transitions).
- In the region above E_{crit} the level scheme is unknown and a full set of nuclear levels is calculated by a random discretization of an a priori known LD.
- Each gamma cascade starts from a single, well-defined initial level (E_i, J_i, π_i). For neutron capture reactions the energy of the excitation level is $E_i = S_n + E_n$.
- The simulation only takes into account the electromagnetic channels (gamma rays and internal conversion electrons). The role of particle channels is completely neglected.
- It is assumed that pairs of partial widths Γ_{if} and $\Gamma_{if'}$ with $f \neq f'$ are not correlated.
- The partial width Γ_{if} for a transition of type X (electric or magnetic, X = E, M) and multipolarity L (L = 1, 2, 3...) is given by

$$\Gamma_{if}^{XL} = (1 + \alpha_{if}^{XL}) \cdot \Gamma_{i\gamma f}^{XL} = (1 + \alpha_{if}^{XL}) \cdot y^2 \cdot \frac{(E_i - E_f)^{2L+1} f^{XL}(E_i - E_f)}{\rho(E_i, J_i, \pi_i)}. \tag{1.43}$$

Where α_{if}^{XL} gives the contribution of the internal conversion, $\rho(E_i, J_i, \pi_i)$ is the LD at the initial excitation level and $f^{XL}(E_i - E_f)$ is the PSF. The factor y is a random number taken from a normal distribution with a zero mean and unit variance $y \in \mathcal{N}(0, 1)$.

This factor ensures that the partial radiation width $\Gamma_{i\gamma f}^{XL}$ fluctuates according to the PTF distribution. In the code, only $E1$, $M1$ and $E2$ transitions are simulated, so only $M1 + E2$ mixed transitions are considered. For these mixed transitions the internal conversion coefficient is given by

$$\alpha_{if} = \frac{\alpha_{if}^{M1} + \delta^2 \alpha_{if}^{E2}}{1 + \delta^2}, \qquad \text{where} \quad \delta^2 = \frac{\Gamma_{i\gamma f}^{E2}}{\Gamma_{i\gamma f}^{M1}} \tag{1.44}$$

The partial width for a $M1+E2$ mixed transitions is done for the sum of each individual transition within this notation

$$\Gamma_{if}^{M1+E2} = (1 + \alpha_{if})(\Gamma_{i\gamma f}^{M1} + \Gamma_{i\gamma f}^{E2}) = (1 + \alpha_{if}^{M1})\Gamma_{i\gamma f}^{M1} + (1 + \alpha_{if}^{E2})\Gamma_{i\gamma f}^{E2} \tag{1.45}$$

with two separate y factors for each individual partial radiation widths. In fact, for $M1 + E2$ transitions the resulting fluctuations are not PTF, but the fluctuations of the separate $M1$ and $E2$ parts are. Finally, the total width for any initial level is calculated by the sum of all partial widths for every final level:

$$\Gamma_\gamma = \sum_f \Gamma_{if}^{XL} = \sum_f (1 + \alpha_{if}^{XL}) \cdot y^2 \cdot \frac{(E_i - E_f)^{2L+1} f^{XL}(E_i - E_f)}{\rho(E_i, J_i, \pi_i)}. \tag{1.46}$$

In nuclei with high LD (and without non-statistical effects) such as actinides and rare-earths, the total width is expected to show very small, albeit non-zero fluctuations as a large number of partial widths is summed.

Hereafter, the term nuclear realization is used to call the set of levels produced for a LD formula together with the set of random partial widths.

The algorithm of DICEBOX

The electromagnetic cascades are generated within the assumptions mentioned above for the discretization of LD and randomization of partial width using the Monte-Carlo technique. The process of getting a nuclear realization is assumed to involve a deterministic random number generator r which has a uniform distribution in the interval $[0, 1)$. The operation of r to produce a sequence of quasi-random numbers is controlled by an adjustable parameter known as the generator seed α.

The algorithm DICEBOX is illustrated in Fig. 1.4. The following enumerated items explain how the gamma cascades are created.

1. For the discretization of the LD, bins are created between E_{crit} and the initial level (S_n+E_n). The width of the bin is typically ∼10 keV. The LD is calculated in the center of the bin and multiplied by the width of the bin to get the average number of levels. For this calculation the spin distribution of the LD is not normalized because the integral is rather close to the unity. Then, a random number is drafted from Poisson distribution with that mean value to get the actual number of level which are located equidistantly in the bin. Finally, the LD is discretized to yield energies E_a, spins J_a and parities π_a for individual levels $a = 2, 3..., a_2$ above a critical energy E_{crit} until the energy of the initial level E_1.

2. The generator seed α_a is ascribed to each level with energy $E_a > E_{crit}$. It is randomly distributed to individuals levels using the aid of succesive calls of the above-mentioned random number generator r.

3. After a generator seed, α_1, is ascribed to the initial level a set of partial width $\Gamma_{1a'}$ from initial level to all possible final levels a' with energy $E_{a'} < E_1$ is generated. The random number generator is preset using the generator seed α_1.

4. For the initial level a total width is calculated by

$$\Gamma_1 = \sum_{a'>1} \Gamma_{1a'} \tag{1.47}$$

   A set of branching intensities for all these transitions from the initial level are obtained following the expression

$$I_{1a'} = \frac{\Gamma_{1a'}}{\Gamma_1} \tag{1.48}$$

   These intensities satisfy the normalization condition

$$\sum_{a'>1} I_{1a'} = 1 \tag{1.49}$$

5. The decay at other level called a_1 is detemined from a random number s_1. The choice of a_1 level follows the requirement

$$\sum_{a'=2}^{a_1-1} I_{1a'} \leq s_1 < \sum_{a'=2}^{a_1} I_{1a'} \tag{1.50}$$

   As a result the level a_1 reached by the first decay in the cascade is known, so the energy E_{a_1}, spin J_{a_1} and parity π_{a_1} are determined.

6. If $E_{a_1} > E_{crit}$ steps 3, 4 and 5 are repeated but considering that the initial level is given by a_1. The generator seed α_{a_1} presets the new random number generator and the total width Γ_{a_1} and the full set of branching intensities $I_{a_1a'}$ are calculated. Then, decays at level a_2 are determined from a random number s_2 given by

$$\sum_{a'=a_1+1}^{a_2-1} I_{a_1a'} \leq s_2 < \sum_{a'=a_1+1}^{a_2} I_{a_1a'} \tag{1.51}$$

7. The procedure in item 6 is repeated until reaching a level a_i which has an excitation energy $E_{a_i} < E_{crit}$. When $E_{a_i} < E_{crit}$ the decays follow the known values calculated from experimental data. Whenever the ground or a non-decaying isomeric state is reached, all data characterizing a single cascade are available: energies E_a, spins J_a, parities π_a and the total widths Γ_a. In addition, the multipolarities L and types X and possibly mixing of different XL of individual transitions in the cascade are available. In principle, any cascade-related quantity of interest can be calculated.

8. The procedure described in steps 5-7 is repeated many times with the same nuclear realization to ensure satisfactory statistical accuracy of a quantity of interest.

9. In order to asses the influence of the Porter Thomas fluctuations of transition intensities and fluctuations in the random discretization of the LD, the algorithm described in items 1-8 is to be repeated many times with different nuclear realizations.

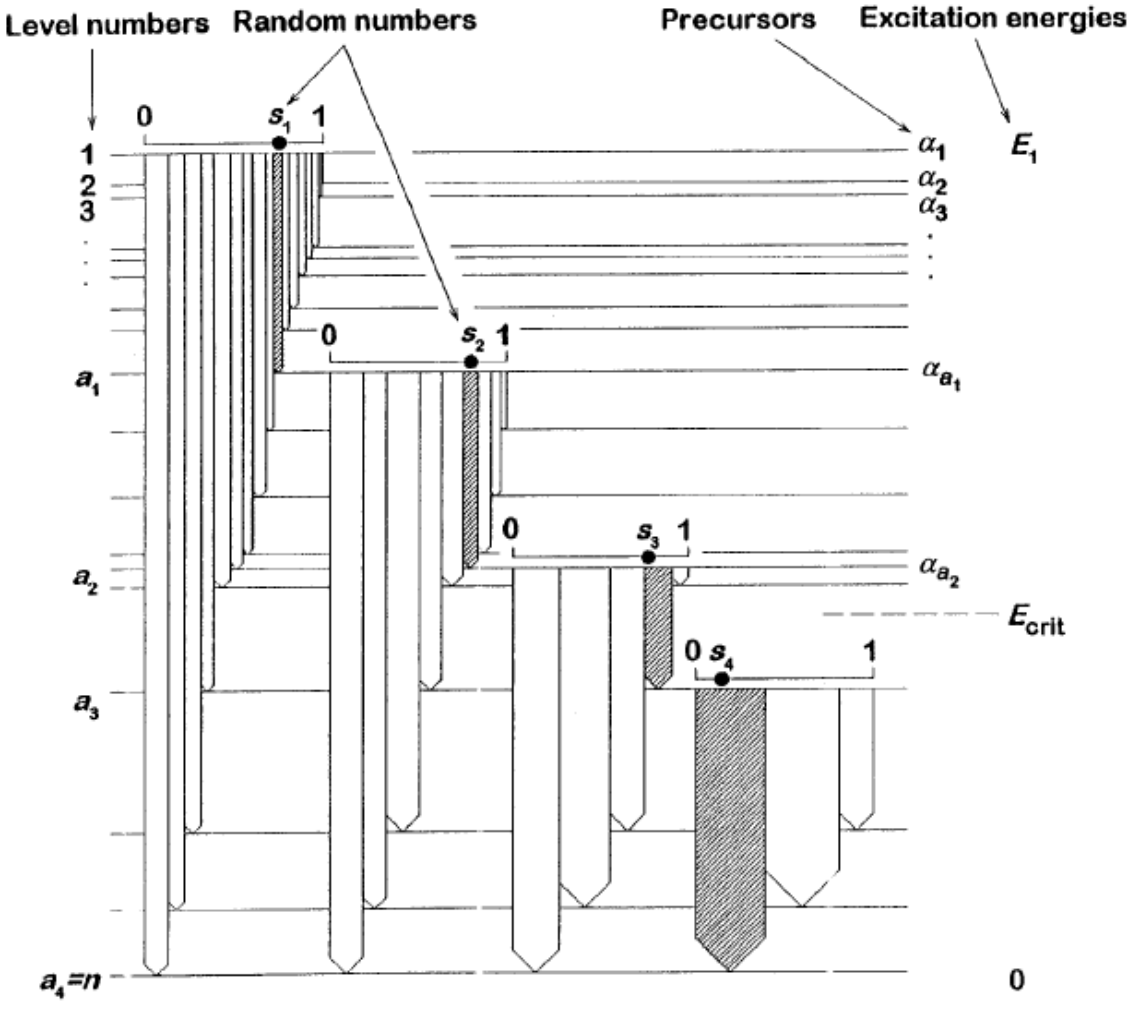

Figure 1.4: Schematic description of random cascading where four gamma rays are emitted [77].

Features and parametrization of DICEBOX

DICEBOX uses LDs and PSFs to create a complete set of nuclear levels above a certain energy E_{crit} and for each level creates a probability distribution function for a gamma decay to lower-lying states. Then Monte-Carlo technique is used to calculate each decay until the ground or a non-decaying isomeric state is reached. In the region above E_{crit}

the decay is purely statistical, no transitions are preferred as no structure is assigned to the states. The partial radiation widths are subject to Porter Thomas fluctuations. The current attributes of DICEBOX for the simulation of gamma cascades are:

- It is a stand-alone Fortran77 code available at [83].
- A great variety of models for LD and PSF is available, both analytically parametrized models and numerical interpolation files. The models used in this work are explained in Sec. 1.1 and 1.2.
- The gamma ray transition probabilities are corrected for internal conversion using a user input table, usually obtained from the BrIcc database [84].
- Levels and transitions from ENSDF [85] are used in form translated to simple text file for further adjustments (level exclusion, spin-parity refinements).
- Simplified user input file with keyword-value structure.
- Output in form of text files gives full information about the cascades within each nuclear realization, in particular about the number of pure and mixed XL transitions in the simulation, the primary intensities, etc.

Finally, the following parametrizations are considered:

- The value of E_{crit} is chosen by a dedicated study of the experimental level density. Fig. 1.5 shows the number of known levels in a bin of 0.1 MeV for a spin window of 1/2 – 5/2. For the low lying discrete levels the number of levels is expected to fluctuate as a result of collective effects such as rotations, vibrations, among others. After that the level density increases up to a certain energy from which it starts to decrease because too many levels are missing. The value of E_{crit} is established around this energy. However, for ^{236}U(n,γ) we chose 0.760 MeV to avoid considering some levels which present questionable information. For instance, the levels at 0.872 MeV, 0.909 MeV and 0.920 MeV present transitions whose intensities do not keep the population-depopulation balance of the levels and, in addition, the spin value is unknown for the 0.909 MeV level. The values of E_{crit} are collected in table 1.2 while the list of experimental nuclear levels used for each uranium isotope is shown in appendix C. Note that only levels with spin $\leq 7/2$ are important in the simulation of the cascade with a feeding higher than 1% because for the uranium isotopes studied here the initial excited states have a spin of 1/2. In addition, different E_{crit} with lower values were tested showing a negligible influence in the results.
- The total radiation width (TRW) is calculated for a fictitious initial $1/2^+$ level at S_n due to the low neutron energy used in this work. Using the s-wave level spacing D_0 the expression for the TRW results in:

$$\Gamma_\gamma = \sum_f \Gamma_{if}^{XL} = \sum_f (1 + \alpha_{if}^{XL}) \cdot y^2 \cdot (E_i - E_f)^{2L+1} f^{XL}(E_i - E_f) \cdot D_0. \quad (1.52)$$

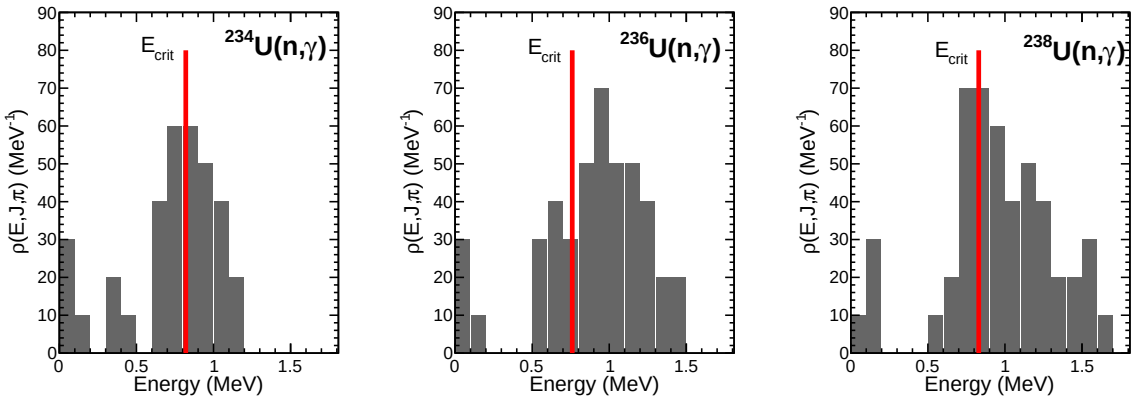

Figure 1.5: Number of levels using a spin window of $1/2 - 5/2$ for bins of 0.1 MeV for ^{234,236,238}U(n,γ). The red line corresponds to the E_{crit} used in DICEBOX.

1.3.2 FIFRELIN

FIFRELIN is a C++ code which simulates the gamma cascade in a similar way to that presented before for DICEBOX. The main goal of FIFRELIN is the simulation of the fission process with neutron/gamma emission but here we only present the technical differences in gamma emission between both codes.

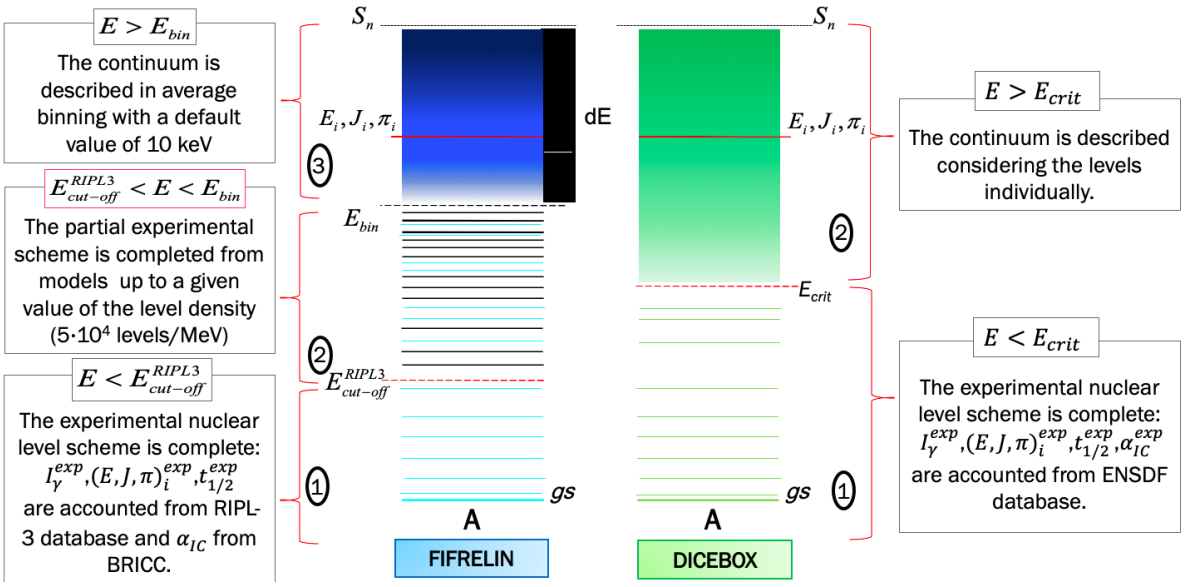

Figure 1.6: Comparison of FIFRELIN and DICEBOX schemes in the simulation of a set of nuclear levels. In the FIFRELIN scheme the blue levels represent the experimental ones while the black levels are sampled.

The main difference is in the simulation of a set of nuclear levels, FIFRELIN divides in three regions the description of the nuclear level scheme while DICEBOX considers only two regions. The schemes of FIFRELIN and DICEBOX are compared in Fig. 1.6. The database used in FIFRELIN for the description of the experimental levels is the 2015

update of RIPL-3 [86].

The first region located between the ground state and a cut-off energy $E_{cut-off}$ provided by RIPL-3 database is considered to be experimentally fully known. It is equivalent to the region below E_{crit} for DICEBOX. The values of $E_{cut-off}$ are collected in table 1.2 for the three systems studied in this work. We can see different values with respect to E_{crit} considered in the DICEBOX code because the value of $E_{cut-off}$ is estimated in a different way. In RIPL-3 $E_{cut-off}$ is calculated by fitting the CT model to discrete levels from N_{min} to N_{max} level number. Some iterations are performed to obtain the minimal χ^2 of the fit whose N_{max} value corresponds to $E_{cut-off}$. The second region is located between the $E_{cut-off}$ and other energy called E_{bin} where E_{bin} corresponds to the energy limit in which the level density value by default is $5 \cdot 10^4$ MeV^{-1} and above this energy the level scheme is considered as a continuum. In this second region some additional experimental levels are taken up to E_{bin} but the level scheme is completed with a LD formula. In addition, contrary to DICEBOX the spin distribution is normalized to the integral of the distribution to calculate the level density. Fig. 1.7 shows the spin distribution $f(E, J)$ given by eq. 1.2 for different σ_c values and the cumulative spectra. We can observe that the cumulative values of the spin distribution are not equal to one for half-integer spins, so a normalization is needed. FIFRELIN uses the approximative spin distribution formula which gives a cumulative result very close to the exact value

$$\sum_{J=1/2}^{\infty} f(J) = \exp\left(-\frac{1}{8\sigma_c^2}\right). \tag{1.53}$$

Finally, in the third region above E_{bin} the nuclear level scheme is only described on average from a LD formula through a default 10 keV binning. The nuclear levels are set in the center of each bin.

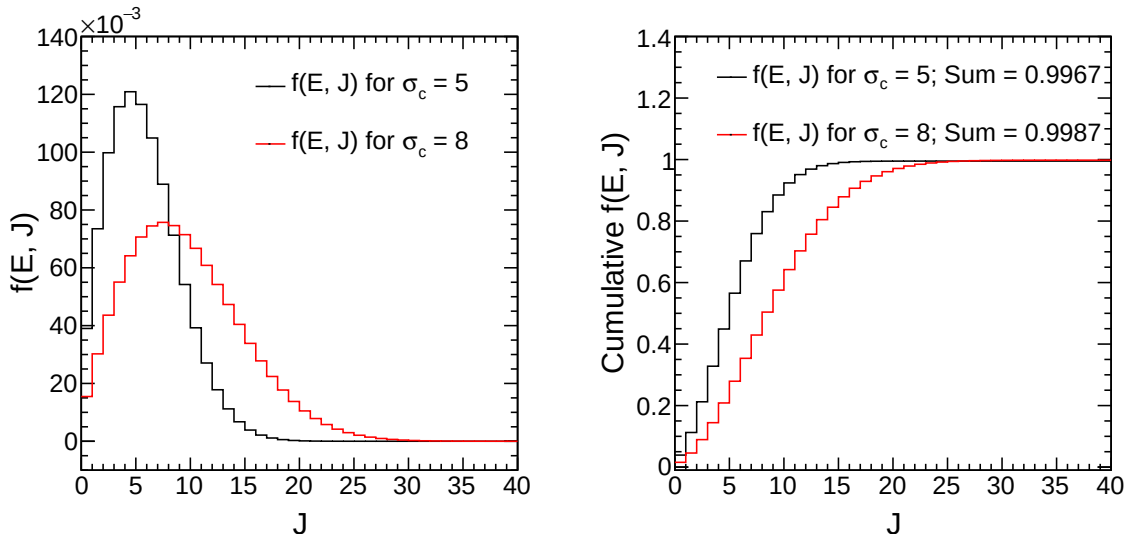

Figure 1.7: Spin distribution for different σ_c values (left) and cumulative spin distribution (right).

Table 1.2: Values of E_{crit} for DICEBOX and $E_{cut-off}$ for FIFRELIN.

Nucleus	E_{crit} (MeV)	$E_{cut-off}$ (MeV)
^{234}U(n,γ)	0.820	0.722
^{236}U(n,γ)	0.760	0.952
^{238}U(n,γ)	0.830	0.373

Concerning the electromagnetic transitions, the partial width Γ_{if}^{XL} for XL transitions and the TRW from an initial level with energy corresponding to S_n are given in FIFRELIN with the same formulas as DICEBOX expressed in eq. 1.43 and 1.52 respectively. In addition, FIFRELIN uses the values for the internal conversion processed by BrIcc [84]. Finally, because FIFRELIN takes the PSF and LD models and parameters from RIPL-3, we had to change the input file to introduce the same input models as used in DICEBOX. The results of the simulations will be used as input data for the Monte-Carlo simulations of the experimental setup Sec. 2.3 and the results of the simulations and the comparison to experimental data will be presented in Sec. 3.2.

Chapter 2

Experimental set-up and simulation

2.1 The n_TOF facility at CERN

This work was performed in the frame of the n_TOF collaboration (neutron Time-Of-Flight), in which 40 laboratories from European countries, Japan, Russian Federation and U.S.A participate. The aim of this chapter is to understand how the experimental data have been obtained and to give a detailed description of the major components of the experimental setup. The measurements were carried out in phase I for ^{234}U(n,γ) (2004) and phase II for ^{236,238}U(n,γ) (2011) data-taking periods of the n_TOF collaboration, so some characteristics of the facility are different.

We can divide the description of the facility in four parts:

- The proton beam.
- The spallation target.
- The TOF beam line or neutron tube.
- The experimental area.

The overall arrangement of the facility is shown in Fig. 2.1

The construction of the n_TOF facility originated from the idea of C. Rubbia *et al.* [88] of using a high energy proton beam provided by the proton synchrotron (PS) of CERN to create a neutron source. These neutrons are produced by the spallation reaction of a pulsed proton beam of 20 GeV/c with a lead target. The spallation target is surrounded by a layer of water for cooling purpose and for moderating the original fast neutron spectrum. The neutron beam travels through the TOF line to the experimental area (EAR1 for our experiment) where the sample of interest and the detection system are installed. In this work we are only interested in the data obtained with the total absorption calorimeter (TAC). Therefore, we will only give a detailed description of this detector in Sec. 2.2. Finally, the energies of the neutrons incident on the samples is calculated using the time-of-flight (TOF) method. The long distance (185 m) of the neutron tube allows for a good neutron energy resolution.

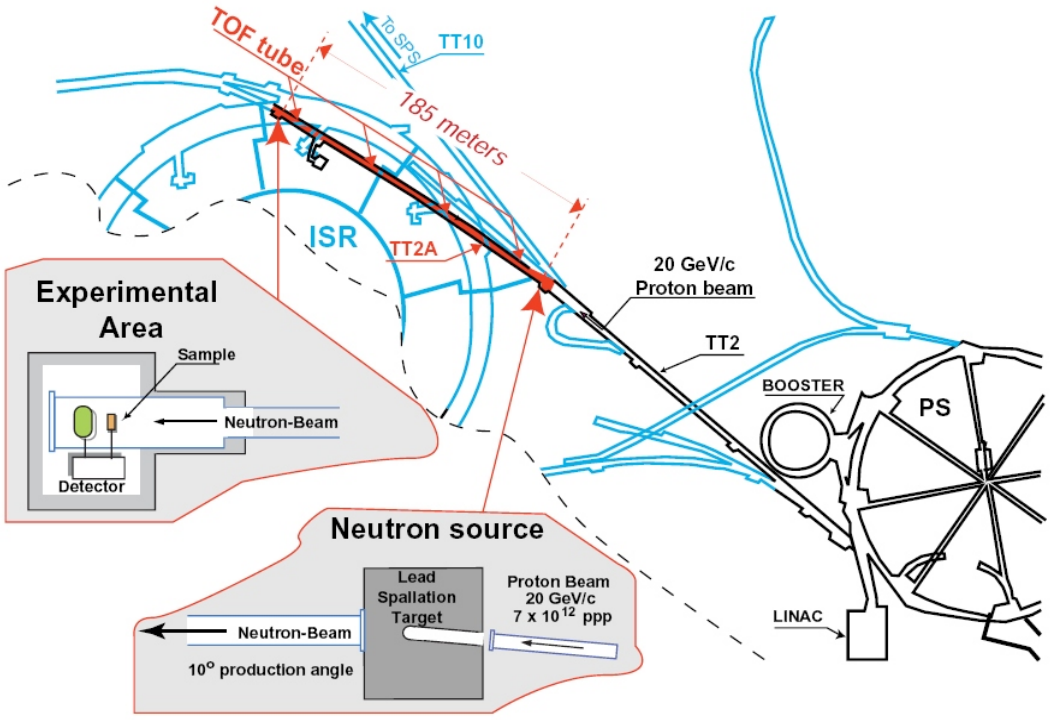

Figure 2.1: General view of n_TOF - experimental area 1 (EAR1) including the Proton Synchrotron. A detailed zoom on the position of the spallation target and experimental area is made [87].

2.1.1 The proton beam

The proton beam is accelerated by a combination of a linear accelerator (LINAC) and a circular accelerator, the proton synchrotron (PS), coupled to a booster (preaccelerator) which allows to reach higher energies. Finally, the proton beam is carried to the spallation target through a proton extraction line TT2, see Fig. 2.1. The proton beam can be delivered in two different operational modes: dedicated mode and parasitic mode.

When the PS operates in dedicated mode an intensity of approximately 7×10^{12} protons per pulse of 7 ns width is sent to the spallation target with a minimum interval of 1.2 s. In the parasitic mode, the PS facility delivers less intense beams with a typical fluence between 3 to 4×10^{12} protons per pulse. These additional protons are distributed to various experiments for optimizing the proton beam use.

2.1.2 The spallation target

The neutron source of n_TOF is produced from a spallation target which is made of lead. The pulsed proton beam of 20 GeV/c interacts with the lead target and high-energy neutrons are emitted via spallation reaction. To increase the neutron population at low energy below 1 MeV, the spallation target is surrounded with a layer of water between the lead target and the window which connects to the TOF tube. Starting from phase II borated water (H_20 + 1.28% H_3B0_3) is used in place of normal water. In addition, the water is used to cool the spallation target. Fig. 2.2 shows a scheme of the

spallation target for phase II.

The geometry of the lead target was studied in detail by Monte-Carlos simulations using codes such as FLUKA [89] for considering the intensity, energy resolution, size, purity and homogeneity of the neutrons beam. These simulations also took into account the water moderator surrounding the lead. In phase I the geometry of the spallation target had a total volume of $80 \times 80 \times 60$ cm^3 while in phase II the target is cylindrical with 60 cm diameter and 40 cm length. To minimize the contamination of the neutron beam with forward-peaked high-energy particles or gamma rays created in the spallation reaction, the proton beam impinges with a tilt of 10° in the horizontal plane between the neutron tube and the proton beam line.

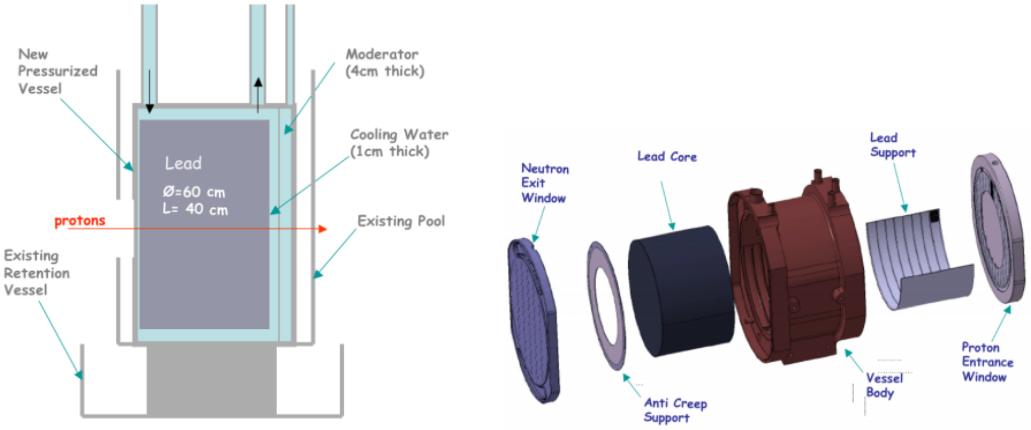

Figure 2.2: Schematic of the sapallation target (left) and target assembly layout (right).

The moderator and the neutron tube are separated by a neutron exit window, Fig. 2.2 right. This window should be as light as possible to avoid the diffusion of neutrons and be composed of a material with minimal neutron absorption. On the other hand, it should be resistant to radiation, since the dose rates accumulated in one year could reach 10^6 Gray depending on the period of use. In addition, the window should be strong enough to separate the water moderator from the neutron tube which is in vacuum (pressure difference of 1.2 bar) and it should not deform (2 mm maximum deflection allowed in the center) in order to ensure a constant moderation in the water. Under these constraints the neutron exit window is made of aluminum with 80 cm diameter and 1.6 mm thick, reinforced by a grid 5 cm thick with sides of 10 cm in length. The struts of the grid have a thickness of 5.5 mm.

2.1.3 The neutron tube

The TOF tube starts directly behind the neutron exit window and ends about 200 m away at the end of the escape line. The neutron tube is equipped with several tube diameter reductions, two collimators and a sweeping magnet. A diagram of the TOF tube is shown in Fig. 2.3. According to the diameter, the tube is divided into three sections:

- The first section of 70 m long with 80 cm diameter.

- The second section of 68.4 m long with 60 cm diameter.
- The third section of 61.6 m long with 40 cm diameter.

Several shielding elements were implemented to reduce the background due to the interactions of the neutrons with the different materials of the facility and to avoid the propagation of neutrons and other particles outside of TOF tube. After the first beam tube reduction an iron shielding of 1.8 m embedded in 40 cm of concrete is placed to moderate the very high energy neutrons. After the second reduction is located the first collimator with 1 m of iron shielding embedded in concrete with a total thickness of 2 m. In addition, after the sweeping magnet, which is placed at a distance of 145.4 m and is used to remove all the remaining charged particles, a Muon shielding of 3 m of iron was placed. Finally, the neutron tube crosses a 3.2 m thick concrete shielding before arriving to the experimental area.

The neutron beam is shaped thanks to two collimators installed along the TOF tube. The first collimator is located at 136.7 m from the spallation target. This collimator is called "source screening collimator" (SSC) because it limits the neutron source area seen by the sample and the number of neutrons reaching the second collimator. The collimator is composed of 1 m of iron and 1 m of concrete and has 5.5 cm radius.

The second collimator is placed at 178 m from the spallation target. This collimator is called "beam shaping collimator" (BSC). It limits the amount of beam intersecting the sample avoiding also interactions with components very near the sample and limiting the background in the experimental area. The diameter of the collimator can be chosen between 18 mm (capture mode with 235 cm of iron plus 50 cm of borated polyethylene) and 80 mm (fission mode with 50 cm of borated polyethylene plus 125 cm of iron plus 75 cm of borated polyethylene) to accommodate the needs of each measurement [90].

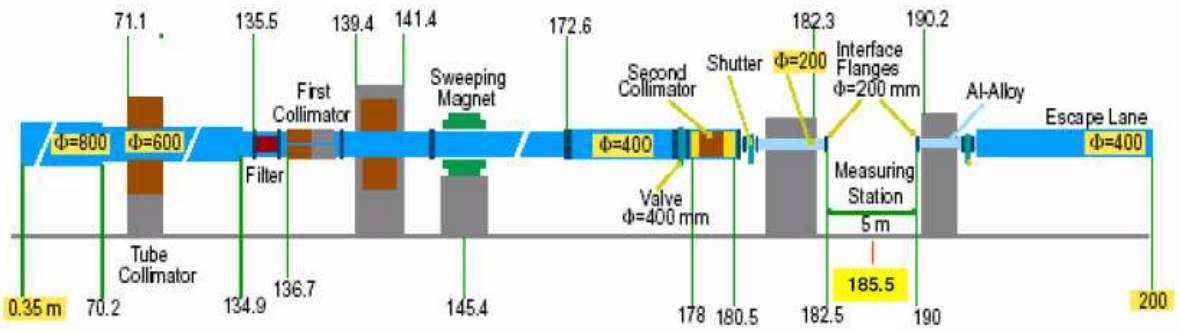

Figure 2.3: The Time-Of-Flight tube. All the distances are given from the target system [91].

2.1.4 The experimental area

The experimental area or measuring station is located after a 3 m thick concrete baffle which is placed just after the second collimator. This area starts at 182.5 m from the spallation target and it extends up to 190 m. Monitors and detectors are installed in this part. The vacuum in this area is between $1.4 \cdot 10^{-1}$ and $3 \cdot 10^{-2}$ mbar.

After the experimental area, a concrete block baffle positioned at 190 m separates the measurement station and the neutron escape line. This zone is used to avoid neutron retrodifusion in the experimental area. The escape line have a length of 10 m and a block of boron Polyethylene located at the end of the tube to absorb the neutrons.

2.1.5 The time-of-flight technique

The aim of the TOF technique is to deduce the kinetic energy of the neutron from the time that the neutron takes to reach the sample from the source position. The kinetic energy of neutrons E_n with a speed $v = L/T$ can be expressed relativistically as

$$E_n = mc^2 \left(\frac{1}{\sqrt{1-\beta^2}-1} \right) \quad \text{with} \quad \beta = \frac{v}{c} = \frac{L}{cT} \tag{2.1}$$

Where L is the distance between the source and the sample, T is the time of flight, m is the neutron mass and c is the speed of light. The first term of the series expansion gives the classical expression for the neutron kinetic energy.

$$E_n = \frac{1}{2}mv^2 = \alpha^2 \frac{L^2}{T^2} \tag{2.2}$$

Taking the values for the speed of light $c = 299792458$ m/s and the neutron mass $m = 939.6$ MeV/c^2 we get

$$E_n = \left(72.298 \cdot \frac{L}{T} \right)^2 \tag{2.3}$$

when L is expressed in meters and T in microseconds.

For each pulse of the proton beam, see Fig. 2.4, a signal (pretrigger) emitted during the acceleration of the protons initializes the acquisition.The acquisition will start at the time t_{ps} which corresponds to the 0 instant of the acquisition system. As soon as the proton pulse reaches the lead target, the neutrons are created at the time t_0, they travel a distance L and are detected at the time t_n. The value for the time of flight is given by $T = t_n - t_0$.

The t_n instant is well known thanks to the detectors in the experimental area. However, the moment of creation of the neutrons after t_{ps} has a distribution. To measure this instant we use the intense radiation called "gamma flash" which is created in the interaction of the proton beam with the spallation target at the same time as the neutrons. The "gamma flash" is detected at a distance L from the lead target by the detectors located in the experimental area at a time t_γ. The instant of creation of the "gamma flash" and therefore of the neutrons is $t_0 = t_\gamma - T_\gamma$, where T_γ is the time it takes for light to travel a distance L, so $t_0 = t_\gamma - \frac{L}{c}$. Therefore, the time of flight of the neutrons is given by:

$$T = t_n - t_\gamma + \frac{L}{c} \tag{2.4}$$

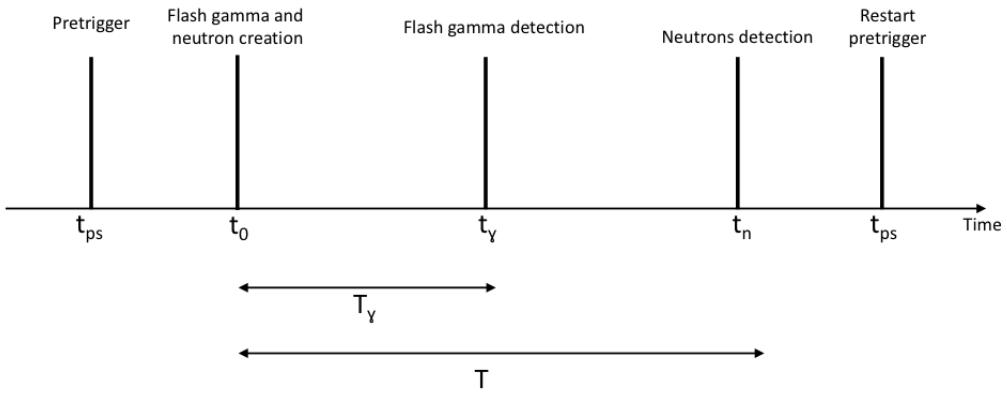

Figure 2.4: diagram of the signals that take part in the measurement of the time of flight of the neutrons for each proton pulse.

2.2 The total absorption calorimeter

The Total Absorption Calorimeter (TAC) at the n_TOF facility (CERN) is based on the BaF_2 calorimeter built at Forschungszentrum Karlsruhe [92]. The TAC is a 4π detector with a high efficiency ($\sim 100\%$ to detect at least the signal of one gamma ray from the cascade) segmented in 40 BaF_2 crystals to detect simultaneously all the gamma rays emitted in a cascade event. The division of a sphere in the TAC is done with 12 pentagonal and 28 hexagonal BaF_2 crystals which cover 95% of 4π. The dimensions of the crystal are 14 cm in diameter and 15 cm in thickness to stop gamma rays with an energy of 10 MeV. Each crystal is connected to a photomultiplier and this module is attached to an aluminum honeycomb structure, which holds the complete assembly. In Fig. 2.5 one hemisphere of the TAC is shown. The sample is placed in the center and after a neutron capture reaction emits gamma rays which are detected by the BaF_2 detectors. Thanks to the segmentation of the detector it is possible to discriminate against different reactions by putting conditions on the crystal multiplicity and the total deposited energy of events registered by the TAC which will be explained in detail in sec 3.1.

2.2.1 The neutron absorber

The main source of background in the TAC are the neutrons scattered by the sample which interact with the different materials of the experimental setup to induce capture reactions. To reduce the contribution of this background two layers of neutron absorber are placed between the sample and the detectors. As mentioned in previous sections the ^{234}U(n,γ) measurement was performed in phase I while the ^{236,238}U(n,γ) measurements belong to phase II, so the materials used for the neutron absorber are different.

The material ^{6}LiH is best suited for the absorber because the hydrogen moderates the neutrons while ^{6}Li absorbs them by the reaction $^6\mathrm{Li}(n,\alpha)\mathrm{T}$. However, ^{6}LiH was excluded for security reasons. In phase I the neutron absorber materials were carefully selected by GEANT4 simulations. Finally, one layer consisted of carbon shells doped with

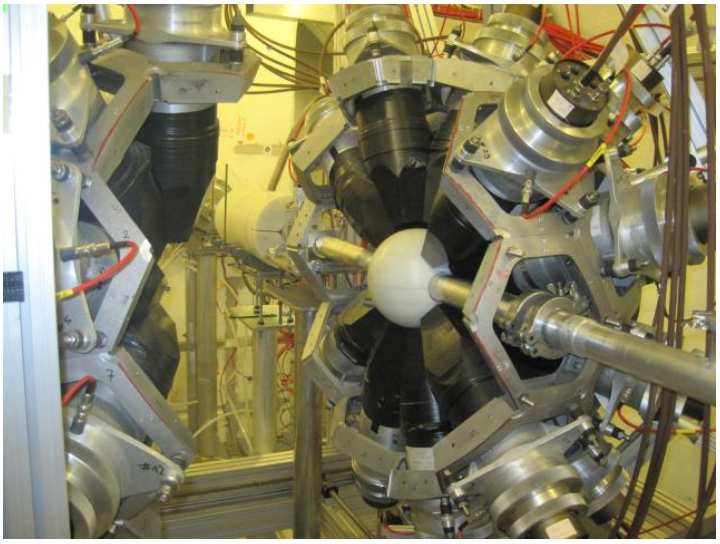

Figure 2.5: One hemisphere of the TAC consisting of the BaF_2 detectors, the neutron beam tube and the neutron absorber.

^{10}B wrapping each BaF_2 crystal. The neutrons are captured through the $^{10}B(n,\alpha)^7Li$ reaction which is responsible for a well-known gamma ray line at 478 keV. The other layer is a sphere composed of an inert non-flammable lithium salt $C_{12}H_{20}O_4(^6Li_2)$ encapsulated by 0.5 mm of Al. In phase II the sphere was composed of an inert non-flammable borated polyethylene enriched to 5% of ^{10}B [93]. Fig. 2.6 shows a hemisphere of these two neutron absorbers.

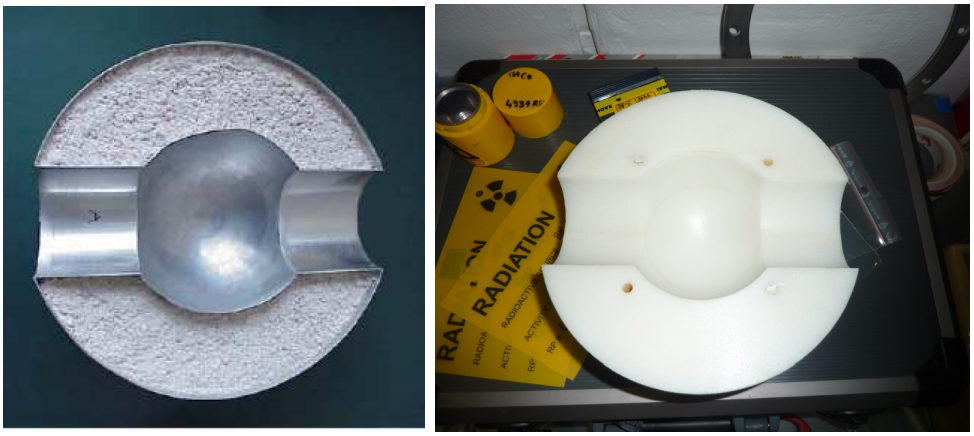

Figure 2.6: One hemisphere of the $C_{12}H_{20}O_4(^6Li_2)$ neutron absorber used during the measurement of ^{234}U (left) and one hemisphere of the borated polyethylene neutron absorber used for ^{236,238}U (right).

2.2.2 Samples for the capture measurements

The knowledge of the characteristics of the samples are crucial because they play an important role in the accuracy that can be reached in the measurement.

The sample of ^{234}U, provided by the institute of physics and power engineering

(IPPE) in Obninsk, is composed of 38.7 mg of U_30_8 of which 32.7 mg are from ^{234}U. The purity of this uranium isotope is more than 99% but there is no detailed isotopic and chemical information available. The sample has a diameter of 10 mm and is inserted between two 0.15 mm foils of Al and encapsulated in 0.2 mm of Ti.

The sample of ^{236}U was manufactured also by IPPE and it is composed by 399 mg of U_30_8 of which 338 mg correspond to ^{236}U. The purity of the sample is 99.85% with traces of ^{235}U (0.05%) and ^{238}U (0.1%). It has a 10 mm diameter and is encapsulated in 0.25 mm of Al and two 25 μm Kapton foils.

The ^{238}U metallic(tbc) sample was provided by the EC-JRC-IRMM [94] with a mass of 6125 mg and an extreme purity of 99.999%. The traces in this sample are ^{234}U (< 1 ppm), ^{235}U (~ 11 ppm) and ^{236}U (< 1 ppm). It is rectangular with dimensions of $\sim 53.90 \times 30.30$ mm and it is envelopped inside a 20 μm aluminum and a 25 μm kapton thick foils.

Each sample was placed in the middle of the TAC and aligned with the n_TOF neutron beam center. The count rate is related with the mass of the sample being higher for high areal density. The ^{236,238}U samples are heavy enough to achieve count rates which produce important dead time and pile-up effects. The analysis to minimize or avoid these effects will be shown later. The characteristics of the samples are summarized in Table 2.1.

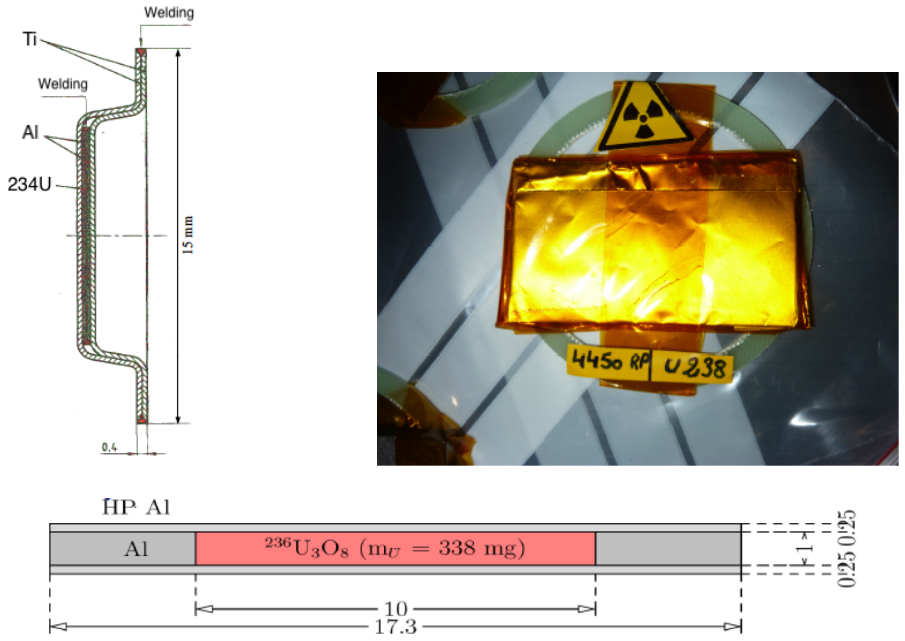

Figure 2.7: The uranium samples used in the different measurements. Diagram of the ^{234}U (left) and ^{236}U (bottom) samples, and ^{238}U sample (right).

2.2.3 Energy calibration and resolution

The sources for the energy calibration of the 40 BaF_2 crystals were different for the ^{234}U(n,γ) and ^{236,238}U(n,γ) experiments. Here we only show the process for ^{236,238}U(n,γ). The procedure is the same for ^{234}U(n,γ) but with sources of ^{88}Y and ^{24}Na.

Table 2.1: Characteristics of the samples and experimental conditions for each measurement.

	^{234}U(n,γ)	^{236}U(n,γ)	^{238}U(n,γ)
Mass (mg)	32.7	338	6125
Areal density (atoms/barn)	1.07×10^{-4}	1.09×10^{-3}	9.56×10^{-4}
Surface (mm^2)	78.54	78.54	1621.22
Encapsulation	0.15 mm Al 0.2 mm Ti	0.25 mm Al 25 μm Kapton	20 μm Al 25 μm Kapton
Purity	^{234}U > 99 %	^{236}U (99.85%) ^{235}U (0.05%) ^{238}U (0.1%)	^{238}U (99.999 %) ^{234}U (< 1 ppm) ^{235}U ($\sim$ 11 ppm) ^{236}U (< 1 ppm)
S_n (MeV)	5.297	5.126	4.806
Detector resolution	13–17%	12–20%	12–20%
Pulse intensity (protons per pulse)	$\sim 7 \times 10^{12}$	$\sim 7 \times 10^{12}$	$\sim 1 \times 10^{12}$
Absorber	$C_{12}H_{20}O_4(^6Li_2)$	borated polyethylene	borated polyethylene

The energy calibration for ^{236,238}U(n,γ) measurements were made with three sources which give four different energy points covering a large part of the gamma energy range of interest. These calibration sources were: ^{137}Cs (E_γ = 0.662 MeV), ^{88}Y (E_γ = 0.898 MeV, 1.836 MeV) and AmBe (E_γ = 4.44 MeV). The measurements with the calibrations sources were performed without the neutron absorber. Fig. 2.8 shows the amplitude spectra of the three sources for an individual detector with the fitted peak. The fitting of the peaks was done with a Gaussian after adjusting the background contribution with a polynomial

$$f(x) = A \exp\left(\frac{-(x-\mu)^2}{2\sigma^2}\right) \cdot \sum_{n=0}^{n_{max}} a_n x^n \tag{2.5}$$

where the order of the polynomial n_{max} varies to adjust better the background. A is the amplitude, μ is the center of the Gaussian and σ is the standard deviation or the half-width of the Gaussian. With this information we can assign an energy to each channel given by μ and calculate the detector resolution from

$$\Delta E = FWHM = 2\sqrt{2\ln 2}\sigma \approx 2.35\sigma \tag{2.6}$$

A second order fit was used to obtain an accurate energy calibration for each crystal as shown in Fig. 2.9 for one crystal. Several calibration measurements were taken at

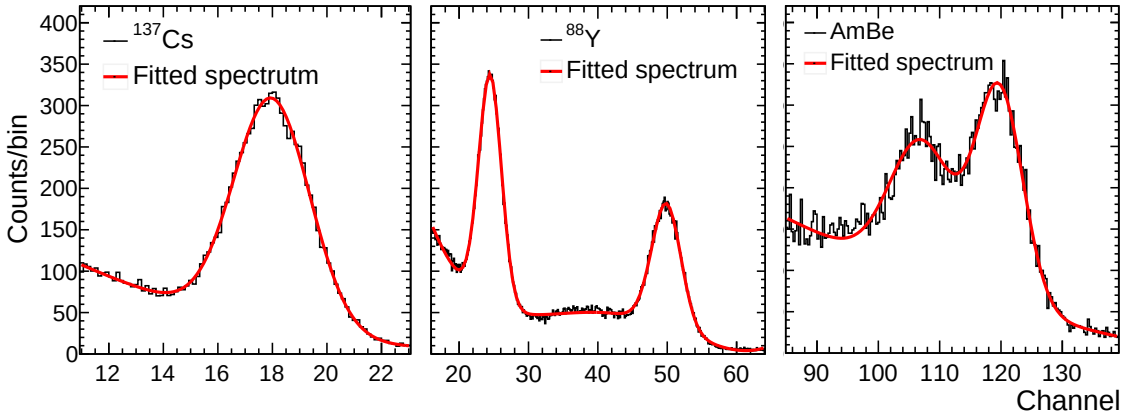

Figure 2.8: Spectra of the ^{137}Cs, ^{88}Y and AmBe sources used for the energy calibration showing the sum of the fitted peak and the adjusted background. The three amplitude spectra correspond to detector 14.

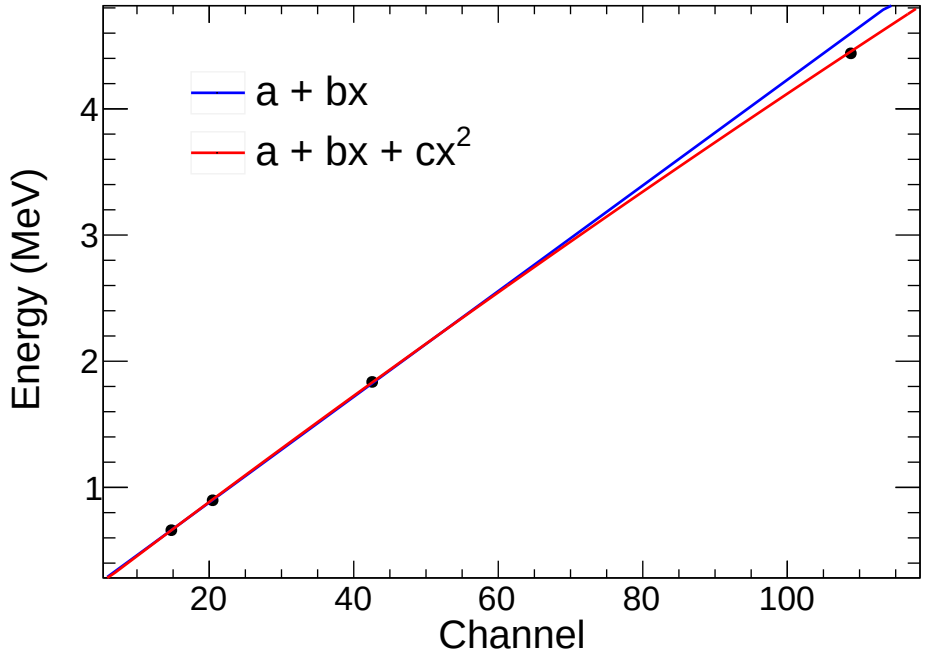

Figure 2.9: Quadratic fit in red solid line for the calibration points obtained with a Gaussian fits from the three calibration samples for detector 1. The blue solid line corresponds to a linear fit which presents a worse adjust of the calibration points.

different times to account for a possible detector drift. However, we can appreciate from Fig. 2.10 that the detectors were stable during the measurements. The drift in each detector was below one channel which corresponds to about 70 keV so we can consider the drift negligible.

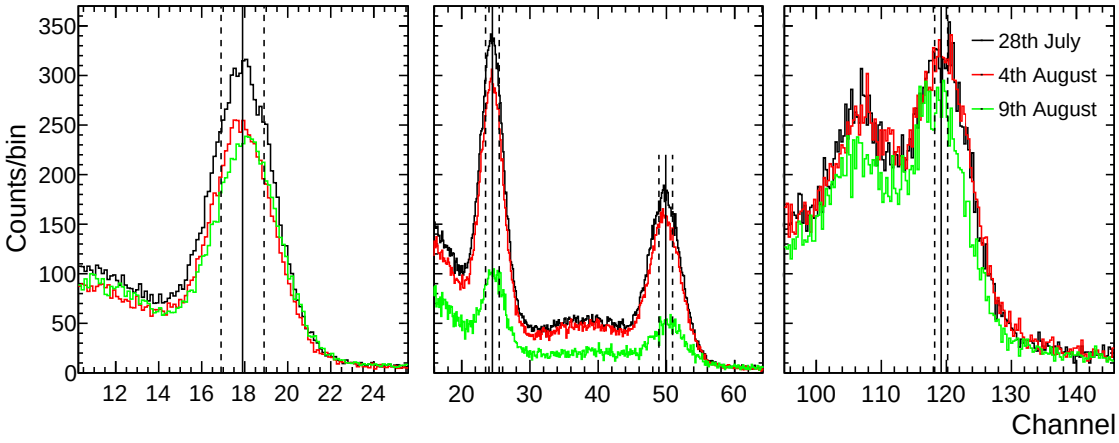

Figure 2.10: Drift of an individual BaF_2 crystal. Three measurements for each calibration source on different times are compared. The vertical line shows the average center of the peak and the dashed lines are placed one channel from the center.

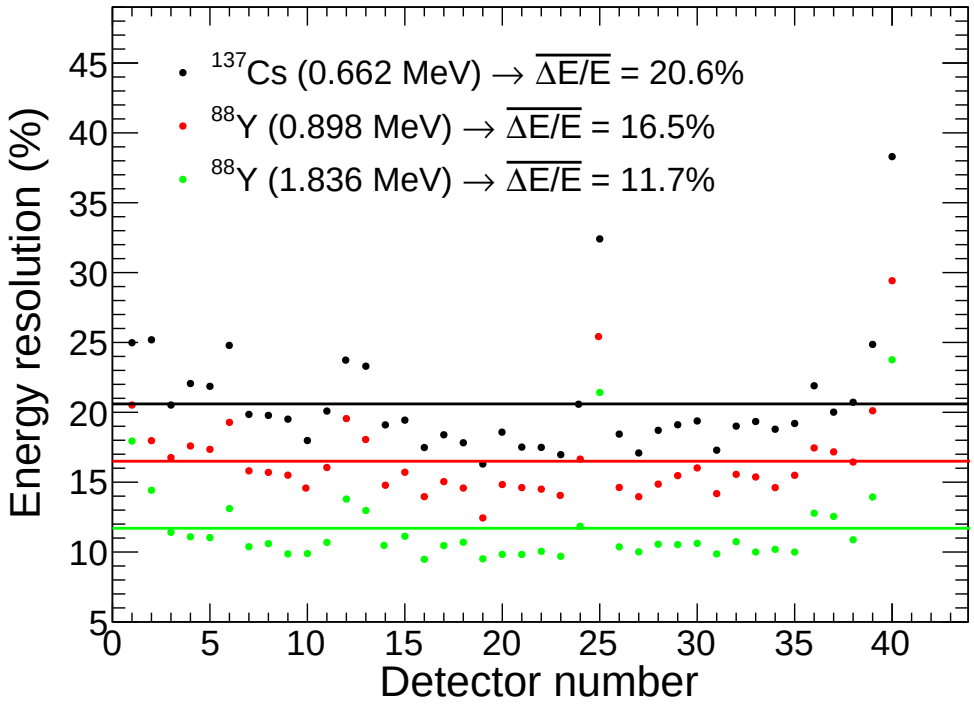

Figure 2.11: Relative resolution at three energies given by the calibration sources for each crystal of the TAC for the ^{238}U campaign. Similar spread was obtained for the other two uraniums but with lower average resolution for ^{234}U campaign. The coloured lines are the average resolution.

The detector resolutions ($\Delta E/E$) are shown for each detector in Fig. 2.11 using the ^{137}Cs and ^{88}Y sources. We can see larger values for the energy resolution of detectors 25 and 40 than for the others. The average energy resolutions of the TAC are 20.6% (0.662 MeV), 16.5% (0.898 MeV) and 11.7% (1.836 MeV). If we compare with the average energy resolutions obtained for ^{234}U(n,γ): 17% (0.662 MeV), 14.5% (0.898 MeV) and 10.1% (1.836 MeV) we note that the resolutions got worse in phase II due to the degradation of detector performance. However, that was enough to discriminate between the background and the events of interest.

2.2.4 Time calibration

The output signals coming from the 40 crystals of the TAC are grouped into 10 acquisition crates each holding different flash-ADC modules and an internal clock. Although the accuracy of the frequency is of the order of ppm, the deviations on time between modules can give an important time offset. Therefore, a time calibration is necessary to performe an accurate analysis.

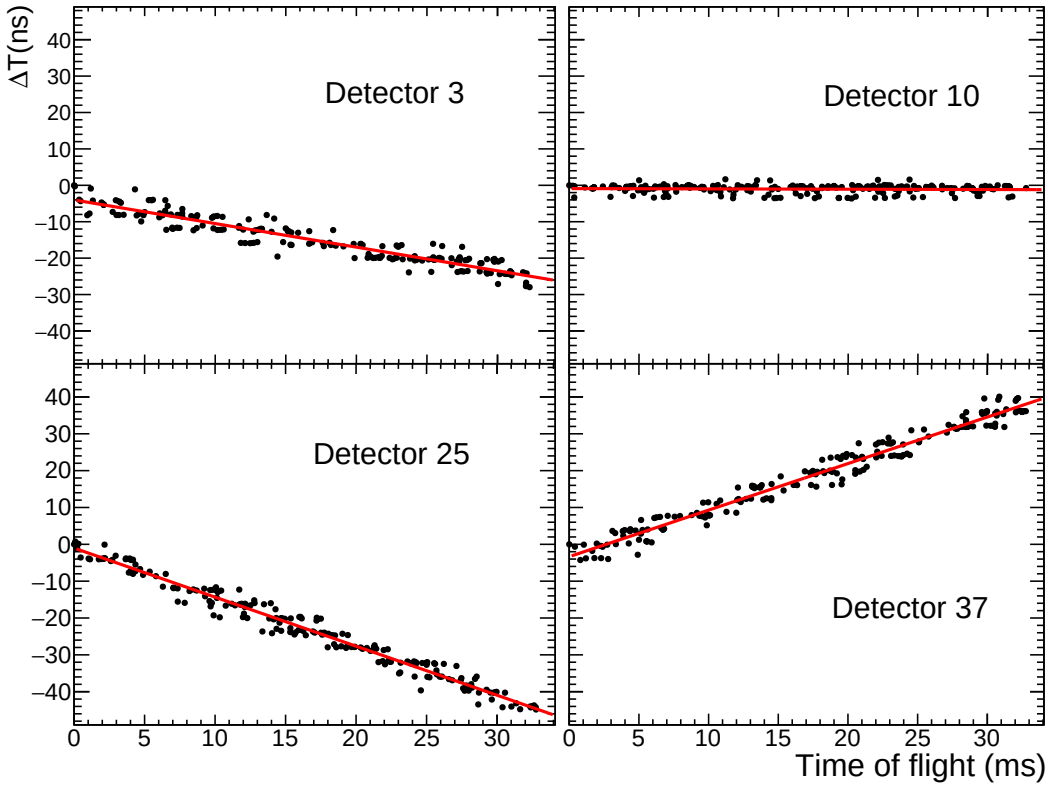

Figure 2.12: Time calibration of the internal clock of four different detectors using detector 11 as reference. The detection time difference between the two gamma rays emitted by the ^{88}Y is fitted by a linear fit.

We use the ^{88}Y source to calibrate the modules in time. The ^{88}Y emits two gamma rays considered instantaneous for the TAC so when a first gamma ray is detected by

one detector taken as reference we can calculate the time delay for the second gamma ray to be detected by another crystal. Fig. 2.12 shows the time calibration for some detectors using detector 11 as a reference. The time calibration is done with a linear fit. The different time at the beginning of the acquisition represents the offset which is produced by different tripping times of the different flash ADCs. On the other hand, the slope is due to the very small difference in the sampling rate of each flash ADC.

2.2.5 Data acquisition system

The n_TOF data acquisition system (DAQ) [95] digitizes the signals from 40 modules with a 8 bits flash-ADC (analog to digital converters) operating at 500 MSamples/s. The BaF_2 signal induced from a detected photon is characterized by a fast and a slow component with $\tau_{fast} = 0.7$ ns and $\tau_{slow} = 630$ ns, respectively. The slow component of the BaF_2 signal is produced by delayed fluorescence and phosphorescence. It takes the most of the light output and is the origin of the pile-up and the dead time in the measurement. The digital pulses are analyzed by a dedicated pulse shape analysis routine (PSA) which fits the fast component with a Lorentzian and the slow component with an exponential. All the information obtained from the PSA (time of flight, amplitude and area for each crystal) and the zero suppresed raw data are stored on CERN's advanced storage manager (CASTOR) [96]. Finally, the extracted parameters for each signal are written in a ROOT file for each run.

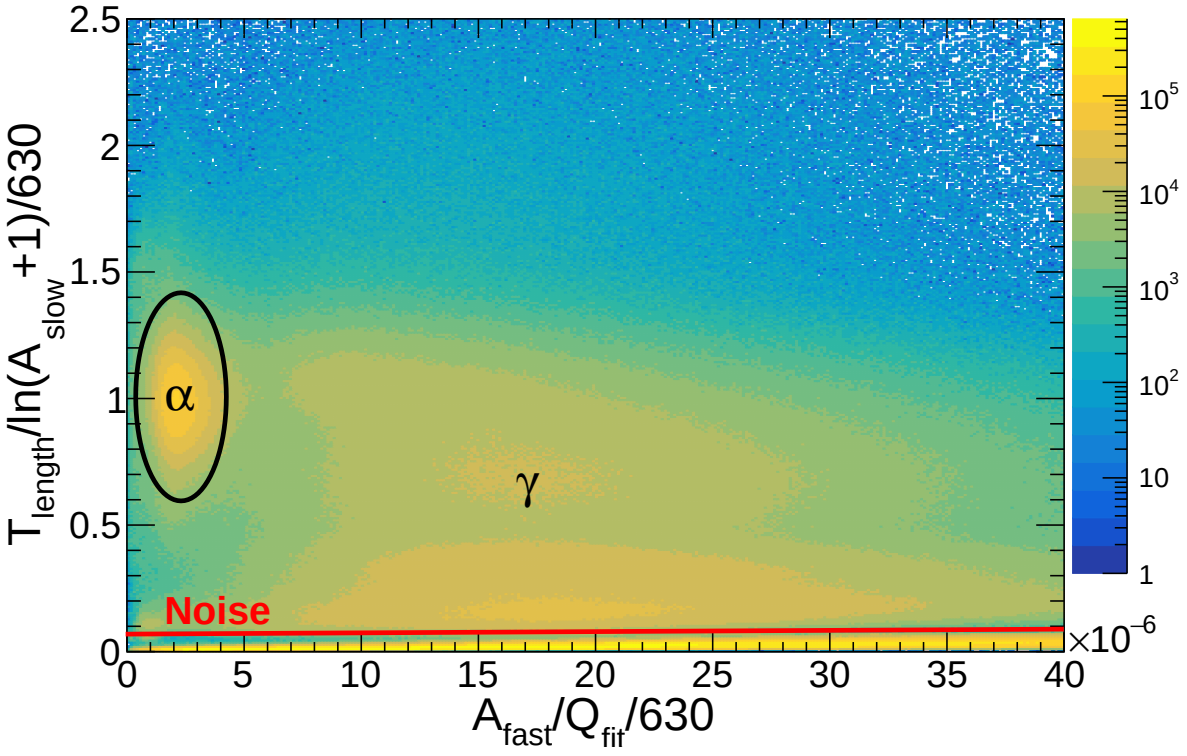

Figure 2.13: Discrimination between different radiation sources from signals by PSA.

An intrinsic background of the BaF_2 crystal is produced by α emission from the radium impurities, ^{226}Ra. These signals lack fast component and can be discriminated by PSA. Fig. 2.13 shows the contribution of the signals for the different radiation in the BaF_2. The α radiation is expected to have a low ratio between the fast amplitude (A_{fast}) and the integral (Q_{fit}) of the signal due to the absence of the fast component in the signal, while the gamma radiation is located at higher values of the ratio. Finally, the noise is characterized by a low value of the ratio between the duration of the measured and expected signal, that is, the signal from the noise quickly returns to the baseline.

2.2.6 Dead time and pile up

The dead time is the minimum time interval between two consecutive signals to identify them as two different events. This effect results in the loss of counts in the TAC. On the other hand, the pile-up takes place when two or more events are close in time and their signals are registered as one signal making difficult its identification by the PSA. The result is the loss of counts and a deposited energy equal to as much as the sum of the signals.

The dead time and pile-up are effects which can appear in the dectector when the counting rate is high. The counting rate of the measurement is related with the intensity of the pulsed proton beam introduced in Sec. 2.1.1 and increases for higher intensities. For the data analysis in this work we are interested to have the lowest count rate to avoid or minimize the effects of the dead time and pile-up. In order to keep good statistics for the data analysis we were able to use the usual nominal intensity of 7×10^{12} protons per pulse for both the ^{234}U(n, γ) and the ^{236}U(n, γ) experiment, while for the ^{238}U(n, γ) measurement we could use only intensity of $\sim 1 \times 10^{12}$ protons per pulse due to the large mass of the sample.

The dead time is studied at the peak of the first resonance as representative of the TAC response to capture events in each uranium isotope and to have a reasonably constant count rate. For statistical reasons, the dead time per detector is approximated to consider the average dead time of all the detectors. Using the interval time (t) between consecutive events detected in a given crystal detector of the TAC we can create an interval time distribution $\Delta T(t)$. To build ΔT a software threshold of 250 keV with elimination of the α radiation and a noise suppression by rejecting events having a short time over threshold with respect to the slow amplitude are applied. For ^{234}U(n,γ) these conditions were enough for the dead time analysis while for ^{236,238}U(n,γ), due to the degradation of detector performance, an interval time dependent term was added to the noise removal criteria. This gave a much higher dead time of up to ~ 6 μs for low amplitude signals. The dead time was estimated by studying the interval time spectra as a function of the second event deposited energy. Finally, $\Delta T(t)$ follows the expression:

$$\Delta T(t) = \exp(a + b \cdot t) \cdot 0.5 \cdot \left[1 + \frac{2}{\sqrt{\pi}} \int_0^{\frac{t-y(E)}{z(E)}} \exp\left(-x^2\right) dx \right] \tag{2.7}$$

For an ideal situation of a non-extendible dead time τ for Poisson-distributed events, the distribution $\Delta T(t)$ would have the form

$$\Delta T(t) = \exp(a + b \cdot t) U(t - \tau) \tag{2.8}$$

where U is the unit step function. The deviation from a sharply defined dead time τ is given by the error function which is normalized to have a function ranging from 0 to 1. The parameters $y(E)$ and $z(E)$ are two polynoms which give the dependence on the energy of the second gamma deposited in the same crystal. In Fig. 2.14 the $\Delta T(t)$ curve is shown for two different ranges of the second gamma energy and the fit of the parameters $y(E)$ and $z(E)$.

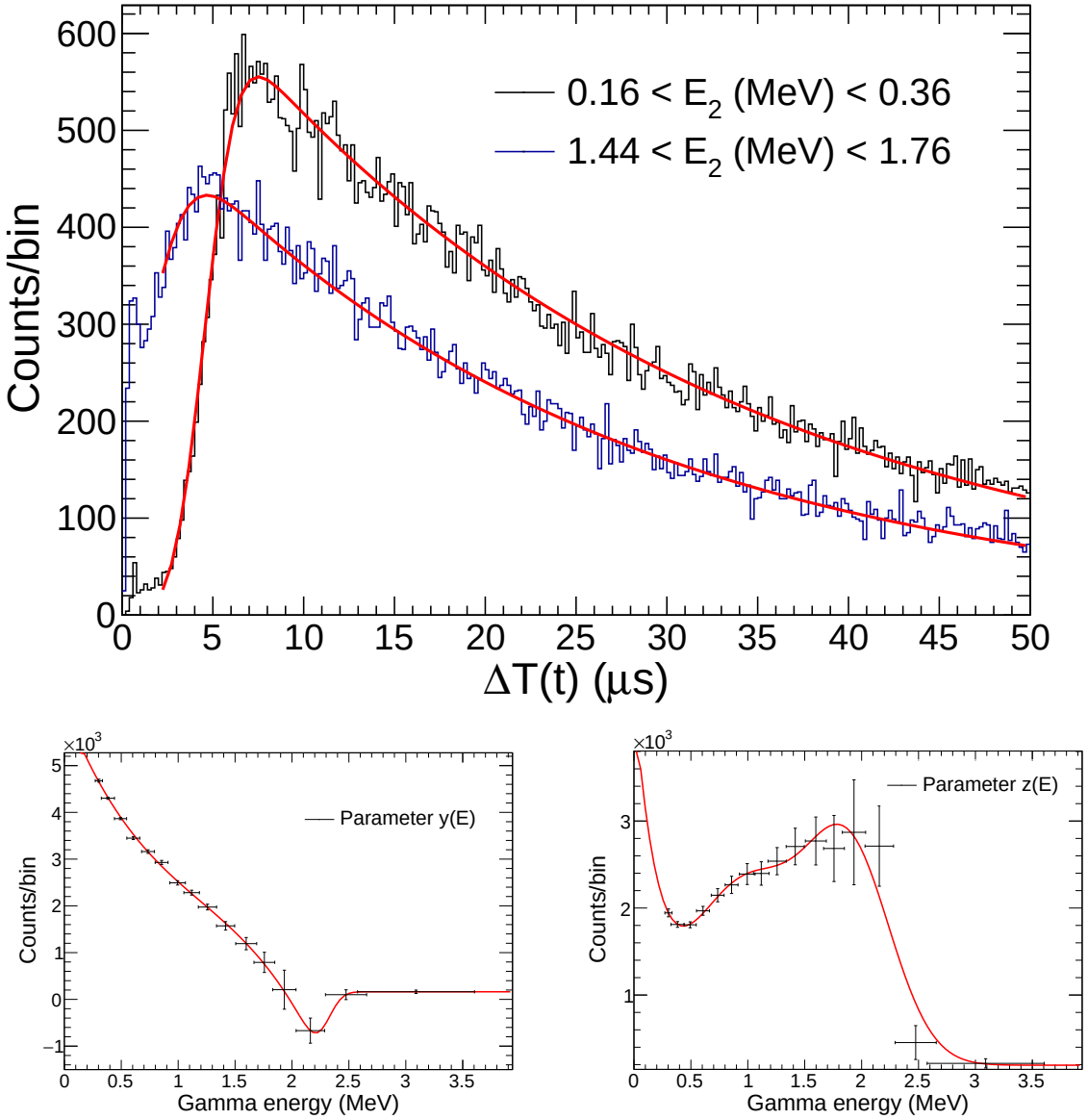

Figure 2.14: Interval time spectra $\Delta T(t)$ as a function of the two ranges of the second event deposited energy (top) and parameters $y(E)$ and $z(E)$ (bottom).

2.3 Simulation Monte-Carlo of the TAC

GEANT4 is a toolkit which serves for the simulation of the interaction of particles through matter using the Monte-Carlo method [97, 98]. It uses the programming language C++ which allows a flexibility in the parametrization of geometry and physical processes. The reasons to simulate the TAC in GEANT4 are:

- Versatility in the modeling of volumes as detector geometry.
- The particle trajectory can be characterized with extensive physics models for the transport of particles through matter.
- Powerful tracking capabilities.
- A great variety of physical processes with a larger set of particles.

In this work we are interested in the detailed treatment of electromagnetic interactions which deals with the transport and detection of γ-rays. The physics processes are modeled using the GEANT4 standard electromagnetic package [99]. This package allows to simulate the different ways of interaction between photons and matter: the photoelectric effect in which the photon is absorbed by an atomic electron, the Compton effect in which the photon loses a part of its energy when it interacts with matter and the pair production in which a positron-electron pair is produced after interaction.

2.3.1 TAC geometry in GEANT4

The TAC's geometry has been modeled following the computer aided design (CAD) drawings of the engineering design and direct measurements of the real geometry. Therefore, the GEANT4 simulations of the TAC have a high fidelity with the real TAC. The 40 BaF_2 crystals are simulated together with their photomultiplier tubes inside an aluminium housing. The two neutron absorbers are simulated using ^{10}B for the capsules enclosing the crystals and the corresponding (^{6}Li or ^{10}B based) material for the sphere around the uranium sample. We used ^{6}Li enriched for the ^{234}U sample and borated polyethylene for the ^{236,238}U samples, as explained in Sec. 2.2.1. Finally, the simulated geometry also includes the aluminium beam pipes in vacuum, the sample holder in the middle of the TAC and the honey-comb structure that holds the complete assembly. Fig. 2.15 shows the GEANT4 geometry for one hemisphere of the detectors and the whole TAC.

However, the distances of each individual module from the centre of the TAC and the density of the neutron absorber can not be determined with accuracy from a direct measurement. This is because the distance varies slightly from module to module and the density of the phase I absorber is not uniform. Therefore, simulations are necessary to adjust these parameters as best as possible.

2.3.2 Determination of the radius of the TAC

The GEANT4 simulation of the TAC only allows the use of a single internal radius, so the slight variation of the distance between each module will not be considered. To

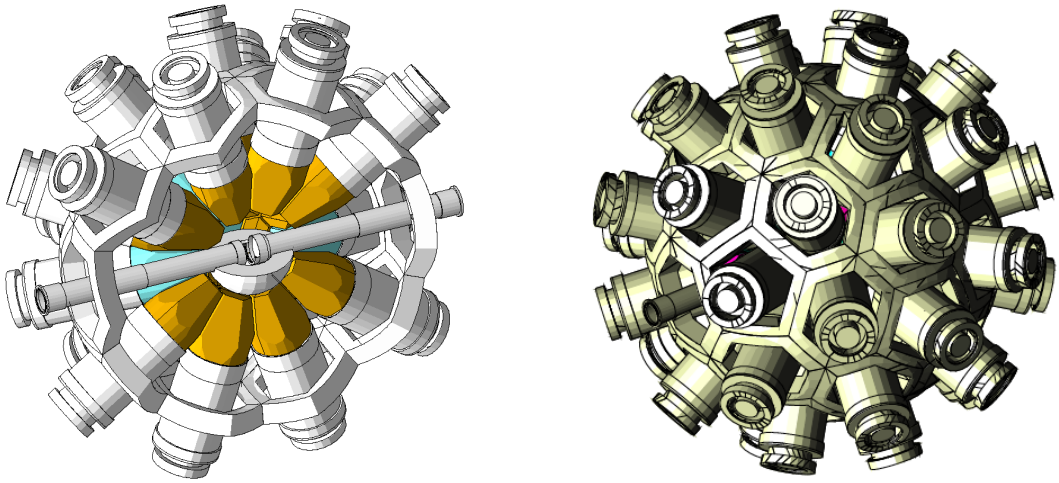

Figure 2.15: Hemisphere of the TAC (left) showing the BaF_2 detectors, the beam pipe and the neutron absorber. The geometry of the full TAC as implemented in GEANT4 (right).

determine the average distance of the modules from the sample in the centre of the TAC some simulations are compared with the experimental data. We used the measurements without the sphere of neutron absorber of the sources of ^{60}Co, ^{24}Na and ^{88}Y after subtraction of the background from a measurement without source. These sources emit two successive γ-rays which are correlated with each other, so the simulations have to take into account the angular correlation given by

$$W(\theta) = 1 + \sum_{i=1}^{l} a_i \ \cos^{2i}\theta \tag{2.9}$$

which determines the probability that a γ-ray is emitted along a given direction in a solid angle Ω if the other γ-ray is emitted at an angle θ relative to the first. Explicit calculations of the angular correlation of succesive γ-rays for all possible combinations of pure dipole and quadrupole radiation are given by Hamilton [100] and Goertzel [101]. For the case of ^{60}Co and ^{24}Na the angular correlation is expressed by the equation from ref. [102]

$$W(\theta) = 1 + \frac{1}{8}\cdot\cos^2\theta + \frac{1}{24}\cdot\cos^4\theta \tag{2.10}$$

and for ^{88}Y

$$W(\theta) = 1 - \frac{3}{29}\cdot\cos^2\theta. \tag{2.11}$$

The left column of Fig. 2.16 shows the decay schemes of ^{24}Na, ^{60}Co and ^{88}Y while in the right column the comparison of the experimental data with the simulation is shown. The normalization of the spectra was done by the total number of counts in the spectra. The radius obtained for each source are:

$$R_{TAC}^{^{24}Na} = 11.10 \text{ cm}, \quad R_{TAC}^{^{60}Co} = 10.80 \text{ cm}, \quad R_{TAC}^{^{88}Y} = 11.05 \text{ cm}.$$

Finally, as could be seen, the internal radius considered in the TAC is slightly different for each source. Therefore, to get a radius that fits as good as possible all measurements the adopted value of the radius of the TAC is determined by averaging the different values obtained to

$$R_{TAC} = 10.98 \text{ cm} \tag{2.12}$$

2.3.3 Determination of the density of the neutron absorber

As noted in Sec. 2.2.1, the neutron absorber was made of $C_{12}H_{20}O_4(^6Li\ )_2$ for the $^{234}U(n,\gamma)$ measurement. The given density of the absorber was 1.1 g/cm^3. To verify this value, the response produced by GEANT4 is compared with the experimental data for ^{60}Co. Fig. 2.17 (top) illustrates the results of the simulations with different density values for the absorber. Finally, to reproduce the experimental data measured with the neutron absorber, it is necessary to reduce the density by 60% of its nominal value. On the other hand, the borated polyethylene neutron absorber for the $^{236,238}U(n,\gamma)$ measurements was well decribed with a density of 1.03 g/cm^3 as seen in Fig. 2.17 (bottom).

2.3.4 Event reconstruction algorithm

The cascade events simulated by the DICEBOX and FIFRELIN codes are the input data for the simulation of the transport and detection in the TAC. The input file consists of the γ-ray energies and the multiplicity of each cascade. All these γ-rays are emitted randomly inside the sample geometry in the middle of the TAC. The γ-rays belonging to the same cascade are emitted isotropically and simultaneously, and transported by GEANT4 standard routines until they are completely detected or have escaped the simulated "world" volume around the TAC set to 2 m. The output file of the GEANT4 simulation collects the energy deposited in each BaF_2 crystal and the crystal multiplicity. This crystal multiplicity will be different from the multiplicity given by the DICEBOX and FIFRELIN codes because the γ-rays could be lost or suffer Compton scattering in the TAC.

So far each event is treated independently. In order for the simulation to be as close as possible to the experiment carried out in the TAC at n_TOF some characteristics have been included.

- We assumed an energy-dependent amplitude resolution for individual crystals based on the study performed in Sec. 2.2.3. The amplitude resolution ranging from about 10% to 17% for $^{234}U(n,\gamma)$ depending on the detector while for $^{236,238}U(n,\gamma)$ the amplitude resolution range from about 12% to 21% as was shown in Fig. 2.11 for each detector.

- A threshold of 250 keV for $^{234,236,238}U(n,\gamma)$ is set for all detectors to suppress the low energy background (same as in the experiment).

- A capture event is considered to be a set of gammas which leave an energy higher than the threshold in the BaF_2 crystals in a time coincidence window of 20 ns.

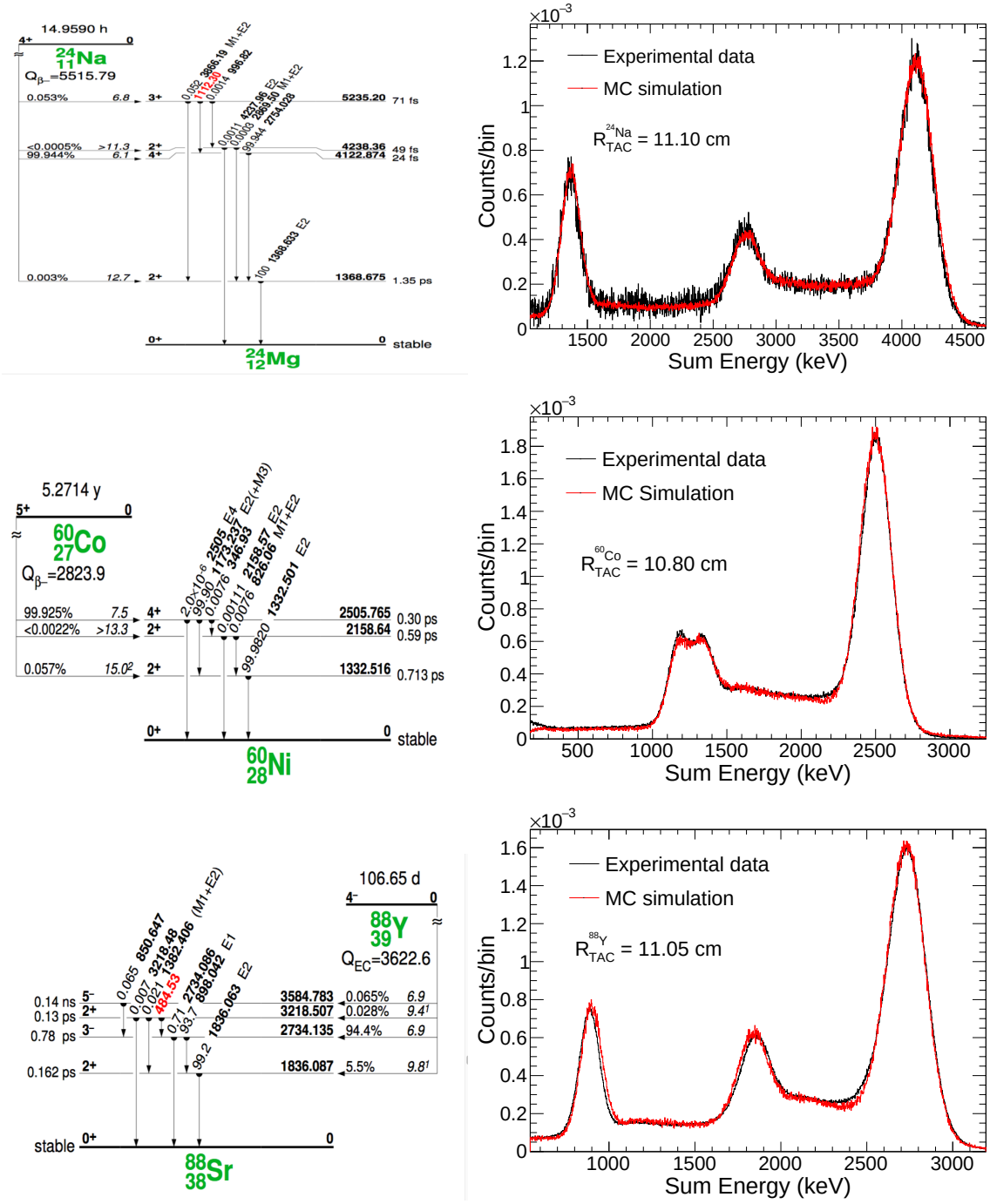

Figure 2.16: Decay scheme of ^{24}Na, ^{60}Co and ^{88}Y (left). Response of the TAC without neutron absorber compared to the simulation with specific values for the internal radius (right).

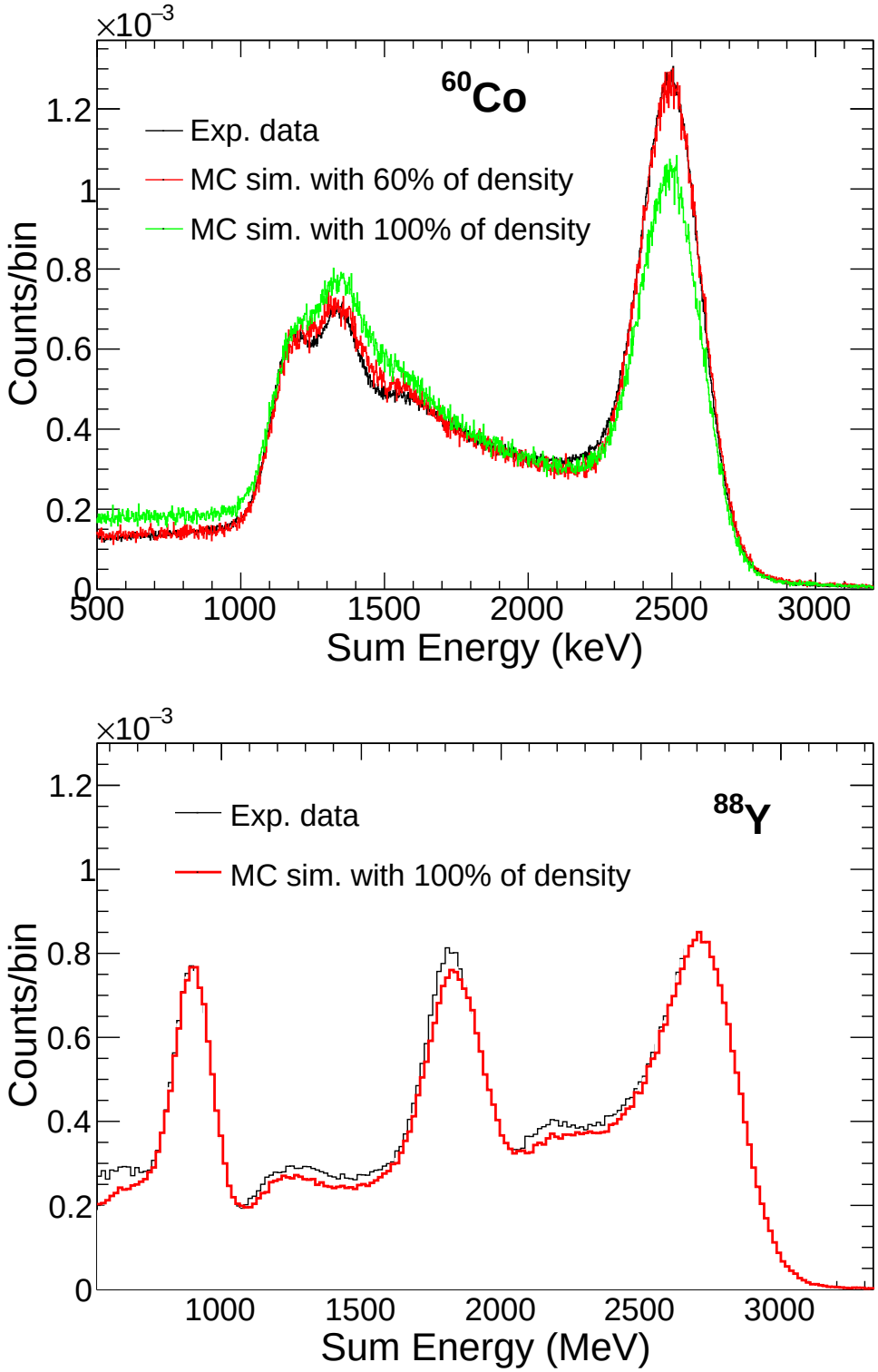

Figure 2.17: Comparison of the spectra obtained for ^{60}Co using a density of the $C_{12}H_{20}O_4(^6Li)_2$ neutron absorber of 60% (red) and 100% (green) of its nominal value, with the experimental data (top). Comparison of the spectra obtained for ^{88}Y using 100% of the nominal density for the borated polyethylene neutron absorber (bottom).

- The effect of dead time and pile-up in the cascade is assumed to influence the spectra as explained in Sec. 2.2.6.

In the simulations, the dead time is computed using a Monte-Carlo technique. A time interval according to a Poisson law for a given count rate is chosen with a random number. The considered count rate is the number of capture reactions detected in the sample per time unit, which is tuneable in the simulation, and which can be assessed experimentally by counting all events detected in the TAC in the considered time window, assuming an 100% efficiency for the TAC response to capture events. Then, a second random number is given following an uniform law. This second random number is compared with the error function normalized between 0 and 1 of the eq. 2.7 corresponding to the time interval given by the first random numbers, if this number is below the normalized error function the event is kept but if it is above the event is lost.

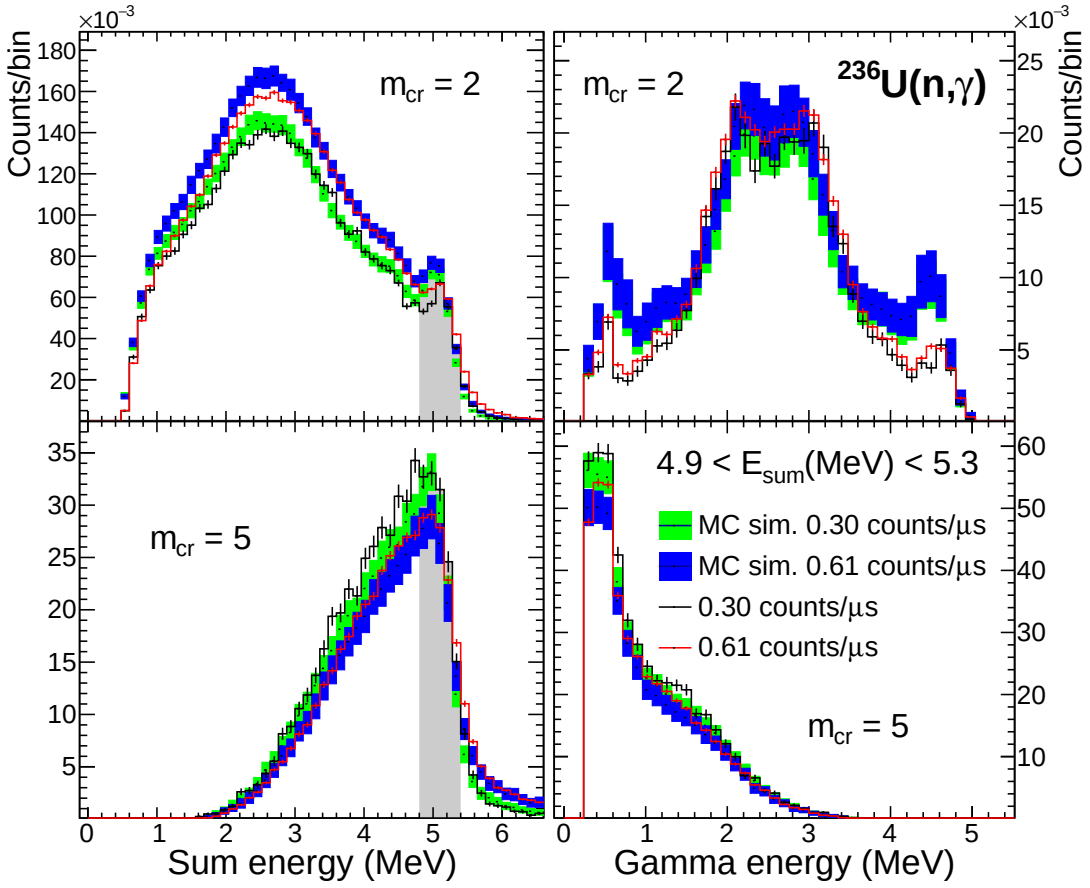

Figure 2.18: Comparison of E_{sum} (left) and MSC (right) spectra from experimental data and simulations for different count rates per pulse.

Finally, to estimate which count rate can be considered to have a negligible effect of the dead time and pile-up, we compared the behaviour of the sum energy and multi-step cascade spectra presented in Sec. 3.1 for different count rates with simulations. In Fig. 2.18 the experimental data and simulations for ^{236}U(n,γ) with different count

rates are compared. The spectra are normalized by dividing by the integral in the sum-energy spectrum for crystal multplicity $m_{cr} \geq 2$ between $E_{sum} = 4.9 - 5.3$ MeV which corresponds to the sum-peak. We observe that the simulations reproduce with reasonable agreement the effect of the dead time and pile-up. The count rate limit obtained with simulations below which the behaviour of the spectra are free from dead time and pile-up are for ^{234}U(n,γ) $\sim$0.35 counts/μs per pulse while for ^{236}U(n,γ) and ^{238}U(n,γ) due to a larger dead time from the degradation of detector performance the count rate limit is $\sim$0.10 counts/μs per pulse. This count rate limit determines the upper neutron energy limit of the resonance analysis of the present thesis to 150 eV in Sec. 3.1

Chapter 3

Analysis and results

3.1 TAC responses from neutron capture reactions

In this chapter all the data analyses for the systems n + ^{234,236,238}U are explained. After a neutron capture reaction the compound nucleus is excited with an energy E_x equal to the sum of the neutron binding energy S_n and the neutron energy E_n ($E_x = S_n + E_n$). It decays to the ground state through a cascade of gamma rays or by internal conversion where an electron is emmited. This process occurs in a very small time interval of a few ns so the cascade events are reconstructed by taking gamma rays detected in the BaF_2 crystals in a time coincidence window of 20 ns. In addition, a software threshold of 250 keV was set for all BaF_2 detectors to suppress the low energy background. In this section we only show the results most relevant to our purpose, for more details about data processing for ^{234,236,238}U(n, γ) reactions please refer to the thesis works performed by W. Dridi [103], M.J. Vermeulen [104] and T. Wright [105].

3.1.1 Observables of the TAC

The experimental information from the waveforms of TAC signals are collected for each detector. From the waveforms it is possible to extract the time of flight of the neutrons t_n, the signal pulse height related to the energy deposited in the crystal and the particle type (alpha or gamma). From this information the observables used for the analysis can be built:

- The time-of-flight spectrum which gives access to the resonance energy.
- The crystal multiplicity, m_{cr}, corresponding to the number of hit crystals for each detected cascade event.
- The cluster multiplicity, m_{cl}, corresponding to the number of hit clusters (crystals and all direct neighbouring crystals) in the cascade event. However, results using m_{cr} and m_{cl} should be similar due to the large crystal size.
- The sum-energy E_{sum} deposited in all detectors for each cascade event.

- The multi-step cascade spectra (MSC) for each crystal multiplicity m_{cr}, which are the gamma-ray energy spectra for fully detected cascades.

The resonance structure which represents the excited levels of the compound nucleus in ^{234,236,238}U(n,γ) reactions are shown in the time-of-flight spectra of Fig. 3.1. The blue shaded areas show the time windows used in the resonances for the data analysis while the red shaded areas correspond to the time windows used for the background subtraction. We only use resonances below 150 eV to stay under the count rate limit estimated to keep the influence from dead time and pile-up discussed in Sec. 2.3.4 negligible and have enough statistic for the analysis. In addition, Fig. 3.2 shows the E_{sum} versus time of flight for ^{238}U(n,γ). We can observe that all resonances are affected by pile-up in the peak. To decrease the value of the count rate we have to choose a time window on the tail of the resonance. In the range examined only s-wave resonances are observed. Moreover, the structures of uranium resonances dominate in this range of time of flight as no contamination from other isotopes is present.

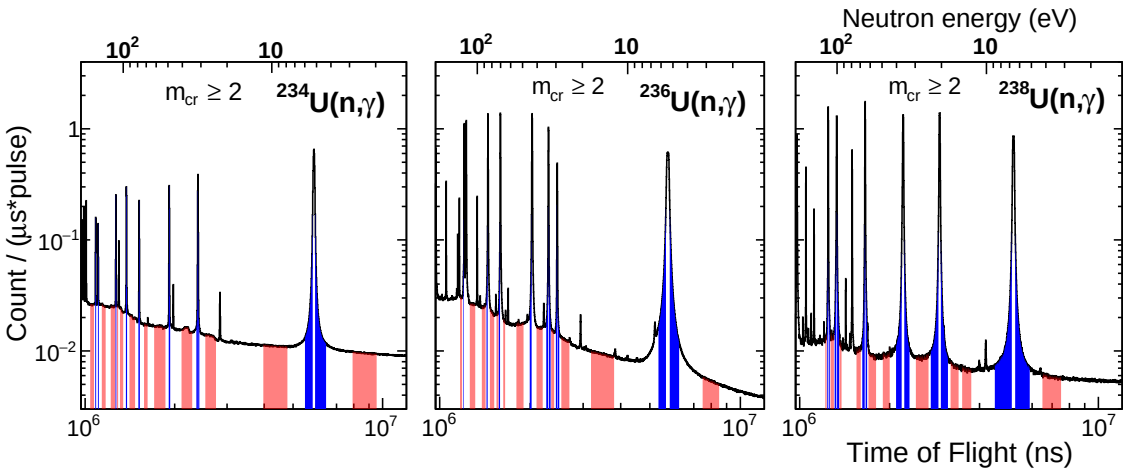

Figure 3.1: Time of flight spectra as a function of the count rate given per μs per pulse with $m_{cr} \geq 2$ for ^{234,236,238}U(n,γ). The top axis show an approximate energy scale. The blue bars show the resonances used for the analysis while the red bars correspond to the windows for the background subtraction. The energies and characteristics of the resonances analysed for each sample can be found in the appendix A.

One of the advantages of the TAC is the ability to discriminate between different types of reactions by choosing m_{cr} and E_{sum} [106]. Fig. 3.3 shows the E_{sum} spectra in the first resonance of the three uranium isotopes for different crystal multiplicity criteria. The spectra present a sum peak with an energy corresponding to the Q value of the reaction which for the neutron energy used in this work is approximately equal to S_n. However, for ^{236,238}U(n,γ) the sum peak is a bit lower than the Q value due to a worse resolution of the detectors. Below the sum peak the spectra present a behaviour produced by the gamma rays which escape from the TAC without leaving all their energy in the crystals or are not detected, in particular when decaying by internal conversion, and by the background. The background from the sample activity or other decays is

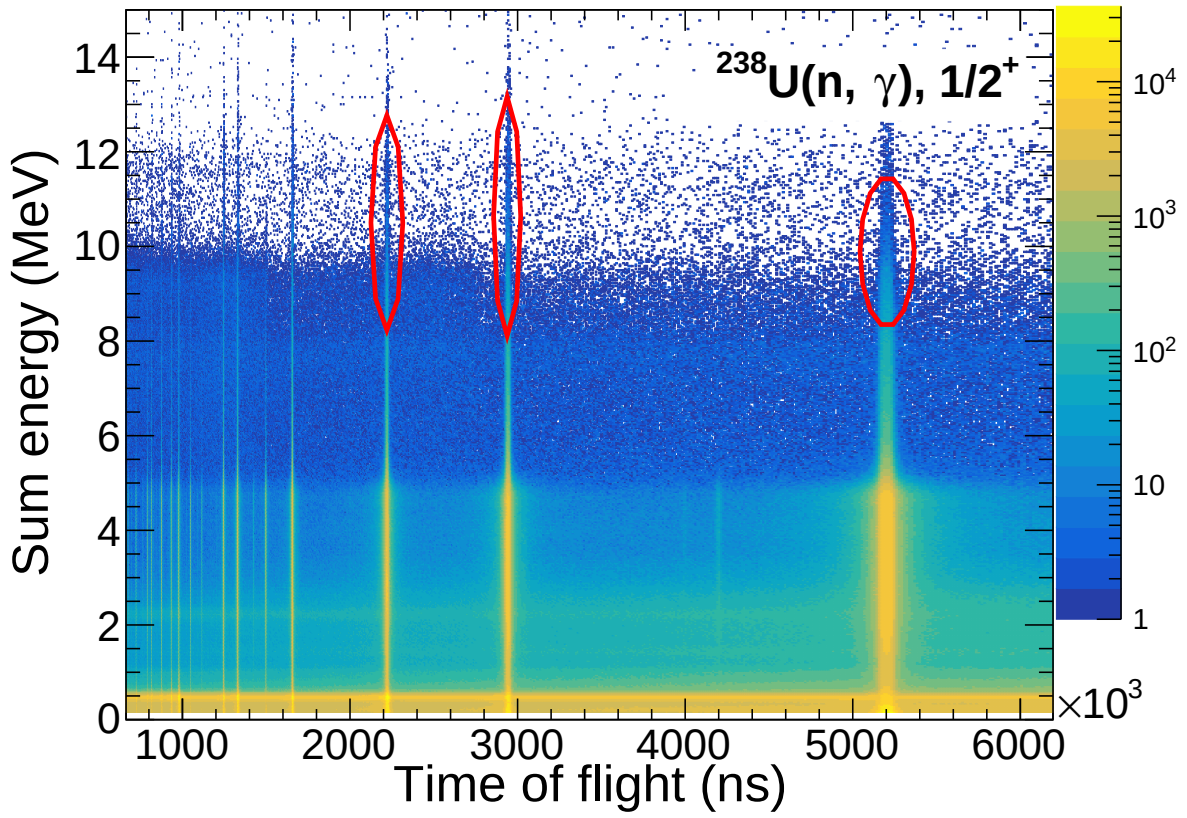

Figure 3.2: E_{sum} versus time of flight spectrum for ^{238}U(n, γ). The red circles indicate pile-up in the resonances where E_{sum} is much larger than the neutron binding energy (S_n = 4.8 MeV).

characterized by a low crystal multiplicity while electromagnetic cascades from neutron capture reactions have a larger crystal multiplicity. We can see in Fig. 3.3 that the $m_{cr} = 1$ spectra (black lines) are dominated by a large number of counts going up to 120×10^3 counts/bin below a sum energy of 1 MeV which we associate with the background while for $m_{cr} \geq 2$ this background is essentially absent. For the present study, only cascades with $m_{cr} \geq 2$ are considered to ensure that the background is correctly subtracted. Finally, the MSC spectra and crystal multiplicity distribution will be studied for events in a window at the sum peak between $E_{sum} = 5.0 - 5.6$ MeV for ^{234}U(n,γ), $E_{sum} = 4.9 - 5.3$ for ^{236}U(n,γ) and $E_{sum} = 4.5 - 4.8$ MeV for ^{238}U(n,γ), which correspond to nearly complete cascades. The normalization of all spectra is done by dividing the spectra by the integral in the sum-energy spectrum for $m_{cr} \geq 2$ in the above mentioned ranges.

3.1.2 Background of the TAC and its subtraction

The background subtraction is very important for an accurate analysis. Although two layers of neutron absorber have been placed between the sample and the detector to

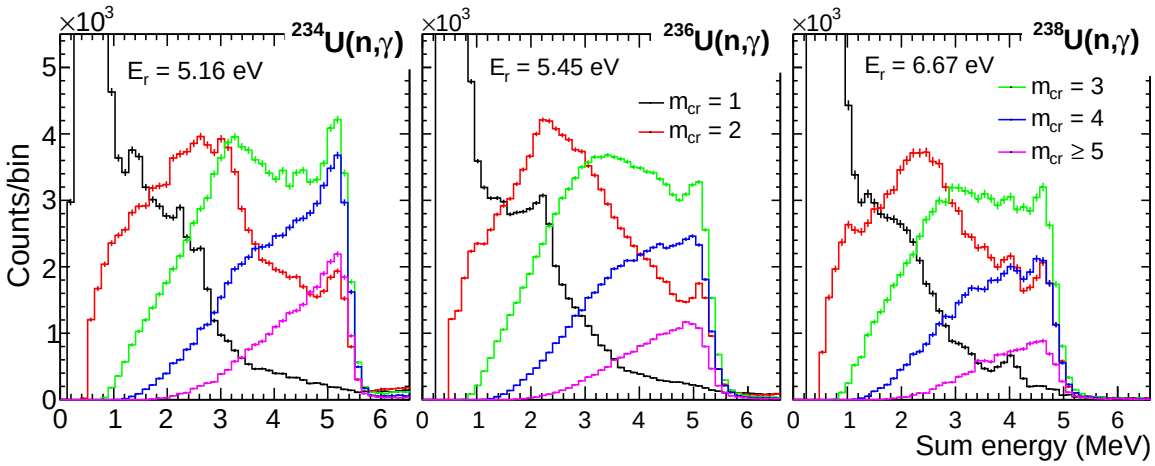

Figure 3.3: Sum energy spectra for the first resonance of ^{234,236,238}U(n,γ) for different crystal multiplicity criteria.

reduce its contribution, the remaining background needs to be subtracted. The main sources of background are correlated with the neutron beam which interacts with the different materials of the experimental setup [107]:

- Gamma rays present in the neutron beam which are produced by neutrons captured in the hydrogen of the water moderator of the spallation target. This is especially true for the ^{234}U(n,γ) measurement, which was not performed using a borated-water moderator which strongly suppresses the 2.2 MeV in-beam gamma ray background.

- Gamma rays and neutrons emitted in the fission process at the sample. However, in our case this is negligible because $\sigma_f \ll \sigma_\gamma$ at low energy, as can be seen from the fission and capture widths for the first resonances, shown in the appendix table A1.

- Capture reactions produced in the sample canning, especially for the sample of ^{234}U which is canned with Ti.

- Neutrons scattered in the samples and captured in the elements composing the TAC and its environment. These captures take place in the neutron absorber ^{10}B, in the Ba isotopes of the crystals and in the Al structure of the TAC.

The ^{10}B produces ^{7}Li* after the (n,α) reaction which emits gamma rays of 0.478 MeV while the other isotopes have a contribution corresponding to the Q value of the reaction collected in table 3.1. In addition, the background is produced by the sample's radioactivity which can deposit energies up to a few MeV and the ambient background dominated by ^{40}K which emits gamma rays of 1.5 MeV.

In this section we only discuss the background to be subtracted from the spectra. However, an exhaustive analysis of the background for these uranium isotopes has already been carried out in the thesis works [103, 104, 105]. All spectra corresponding

Table 3.1: Q values of the neutron capture reactions in the different material of the facility and the samples of uranium.

Reaction	Q (MeV)	Reaction	Q (MeV)	Reaction	Q (MeV)
^{1}H(n,γ)	2.2	^{135}Ba(n,γ)	9.1	^{234}U(n,γ)	5.3
^{48}Ti(n,γ)	8.1	^{137}Ba(n,γ)	8.6	^{236}U(n,γ)	5.12
^{50}Ti(n,γ)	6.4	^{27}Al(n,γ)	7.7	^{238}U(n,γ)	4.8

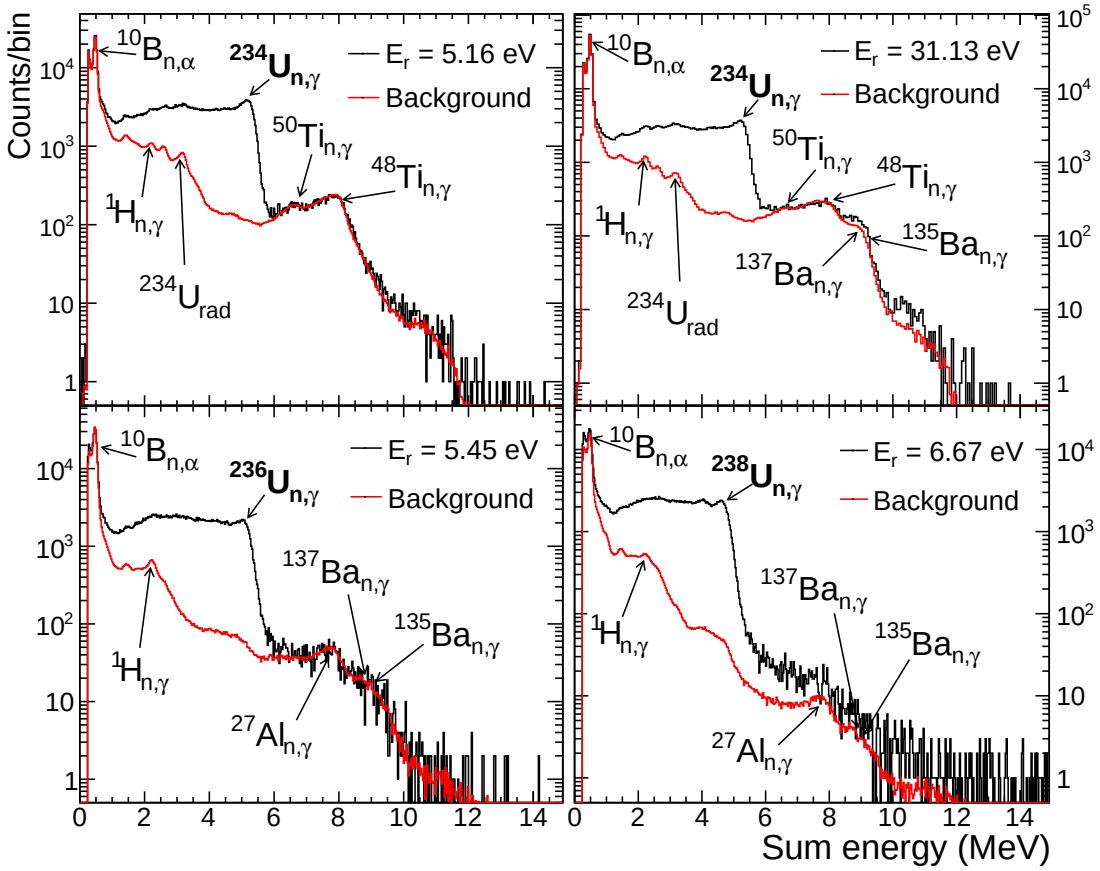

Figure 3.4: Background of the s-wave $1/2^{+}$ resonances for ^{234,236,238}U(n, γ). The black line corresponds to the E_{sum} spectra without conditions for all m_{cr} and the red line is the background to be subtracted from each spectrum.

to each resonance region have been subtracted by a background estimated from the spectra from neighbouring background regions after linear interpolation as shown in Fig. 3.1. This method of background subtraction is very effective to reduce the different components of the background and their contribution to the spectra. The E_{sum} spectra for all m_{cr} of some s-wave $1/2^{+}$ resonances for ^{234,236,238}U(n,γ) and the background to be subtracted with this method are shown in Fig. 3.4. The other resonances used in this work present similar background subtractions. The contribution of the sample's

radioactivity is more important for the sample of ^{234}U and is significant up to ∼3 MeV. This difference is because the sample of ^{234}U has impurities of ^{232}U in very small quantities and it decays in a complex path to ^{208}Pb with emission of two strong gamma rays of 3.198 MeV and 2.614 MeV, among others. In addition, the background from the Ti is only present for ^{234}U(n,γ) because of its specific canning. Thus, for ^{236,238}U(n,γ) the contribution of the ^{27}Al can be seen because this energy range is not dominated by the Ti contribution. Studying the behaviour of the background in different resonances we noted some variations, especially for the Ba isotopes in the BaF_2 crystals for ^{234}U(n,γ) as seen in Fig. 3.4. The background due to ^{135,137}Ba(n,γ) reactions are observed at $E_r = 31.13$ eV and higher resonances while for $E_r = 5.16$ eV this range of energy is dominated by the Ti isotopes in the case of ^{234}U(n,γ). These differences are related to a larger neutron scattering width Γ_n in the higher energy resonance and it follows the resonant behaviour specific to the Ba capture cross sections. This behaviour occurs for all the isotopes in the materials composing the experimental setup. In the background subtraction of ^{238}U(n,γ) we can see some differences with respect to the E_{sum} spectra after the sum peak. These differences are negligible and are produced by the pile-up effect which was checked using other time window with lower count rate. Finally, the method of background subtraction with the criteria on the crystal multiplicity ensures a good elimination of the background in most spectra and keeps only the gamma rays from the reactions of interest.

3.1.3 Comparison of different resonances

Resonances with the same spin and parity $1/2^+$ are compared between them to consider possible fluctuations. As explained in previous subsections only part of the resonances are studied to have a count rate below a limit estimated by the analysis of the dead time and pile-up with simulations. Unfortunately for ^{238}U(n,γ) not all resonances present enough statistics for the data analysis while for ^{236}U(n,γ) we need to choose a time window with a count rate around 0.20 counts/μs per pulse so the influence of dead time and pile-up on the spectra is negligible. In the appendix table A1 the energy E_r, spin and parityJ^π, neutron width Γ_n, gamma witdh Γ_γ, fission width Γ_f and count rate for the resonances used in each uranium isotope are collected.

In order to increase the statistics of the analysis we sum the spectra obtained in both the low-energy and high-energy tails of the resonance. We only do the sum of them in the resonances in which the spectra present similar behaviour. Fig. 3.5 shows two representative cases in which the spectra in both tails of the resonance have different trends. For ^{238}U(n,γ) we note that the E_{sum} spectra present a different behaviour related to the accuracy of the background subtraction while the MSC spectra are similar in both tails. On the other hand, for ^{236}U(n,γ) we can observe differences in the spectra probably related to the possible presence of a p-wave in the tail, the background subtraction or the dead time effect.

Figs. 3.6, 3.7 and 3.8 show the E_{sum} and MSC spectra for ^{234,236,238}U(n, γ) after summing the tails when possible. We can observe that these two observables present notable fluctuations mainly attributed to the Porter-Thomas fluctuations (PTF) of primary transition intensities among the resonances. These fluctuations are stronger for the

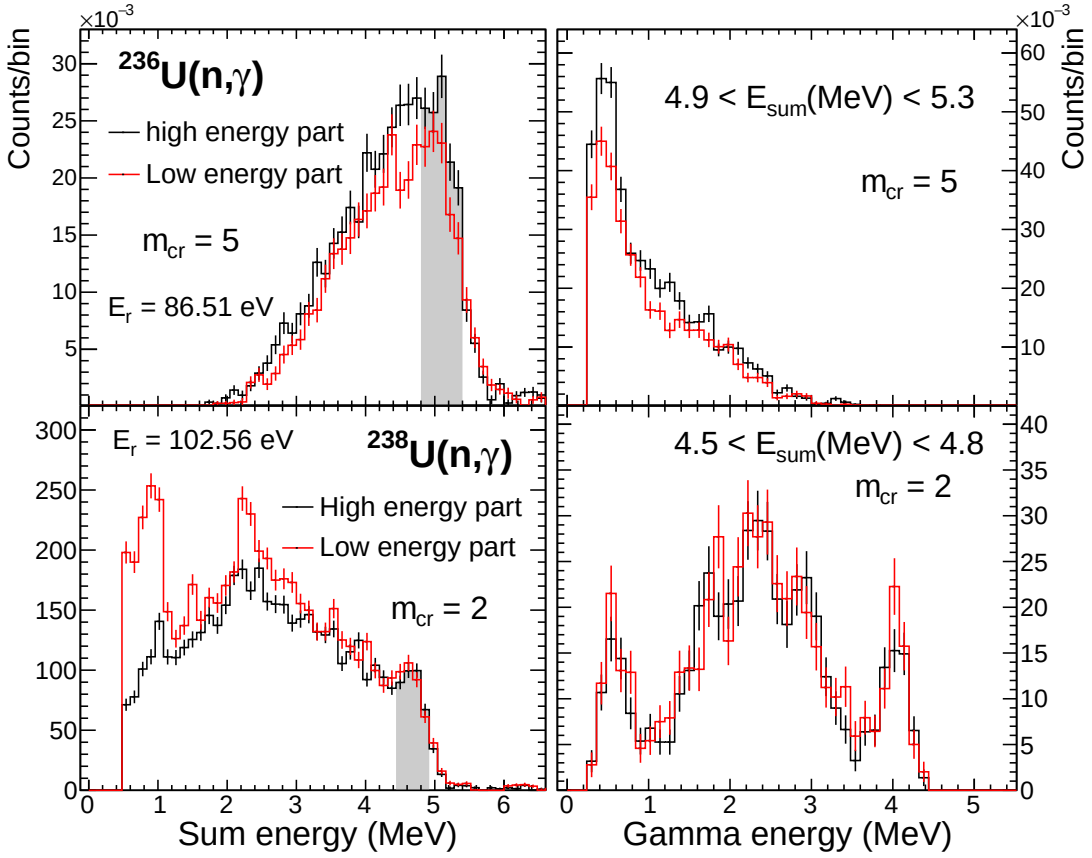

Figure 3.5: Comparison between E_{sum} and MSC spectra for a given crystal multiplicity of both the low-energy and the high-energy tails of the resonances at $E_r = 86.51$ eV and $E_r = 102.56$ eV for ^{236,238}U(n,γ) respectively.

MSC spectra with $m_{cr} = 2$ because they are directly related with the primary intensity and they decrease for higher crystal multiplicity. In addition, the crystal multiplicity distributions shown in Fig. 3.9 present also important variations between resonances related with PTF. Thus, to facilitate the analysis we will use the average spectra of the resonances and the standard deviation which is representative of the fluctuations due to PTF as seen as a reddish band in the figures.

3.2 Comparison of simulations and n_TOF measurements

In this section we compare the experimental data of the three uranium isotopes presented before with the simulations given by DICEBOX and FIFRELIN, described in Sec. 1.3, to produce the gamma cascades and GEANT4, described in Sec. 2.3, to simulate the transport and detection of these gammas with the complete TAC experimental setup. This study will be mostly qualitative paying attention to the behaviour of the spectra. In addition, as an attempt to quantify the agreement between simulations and

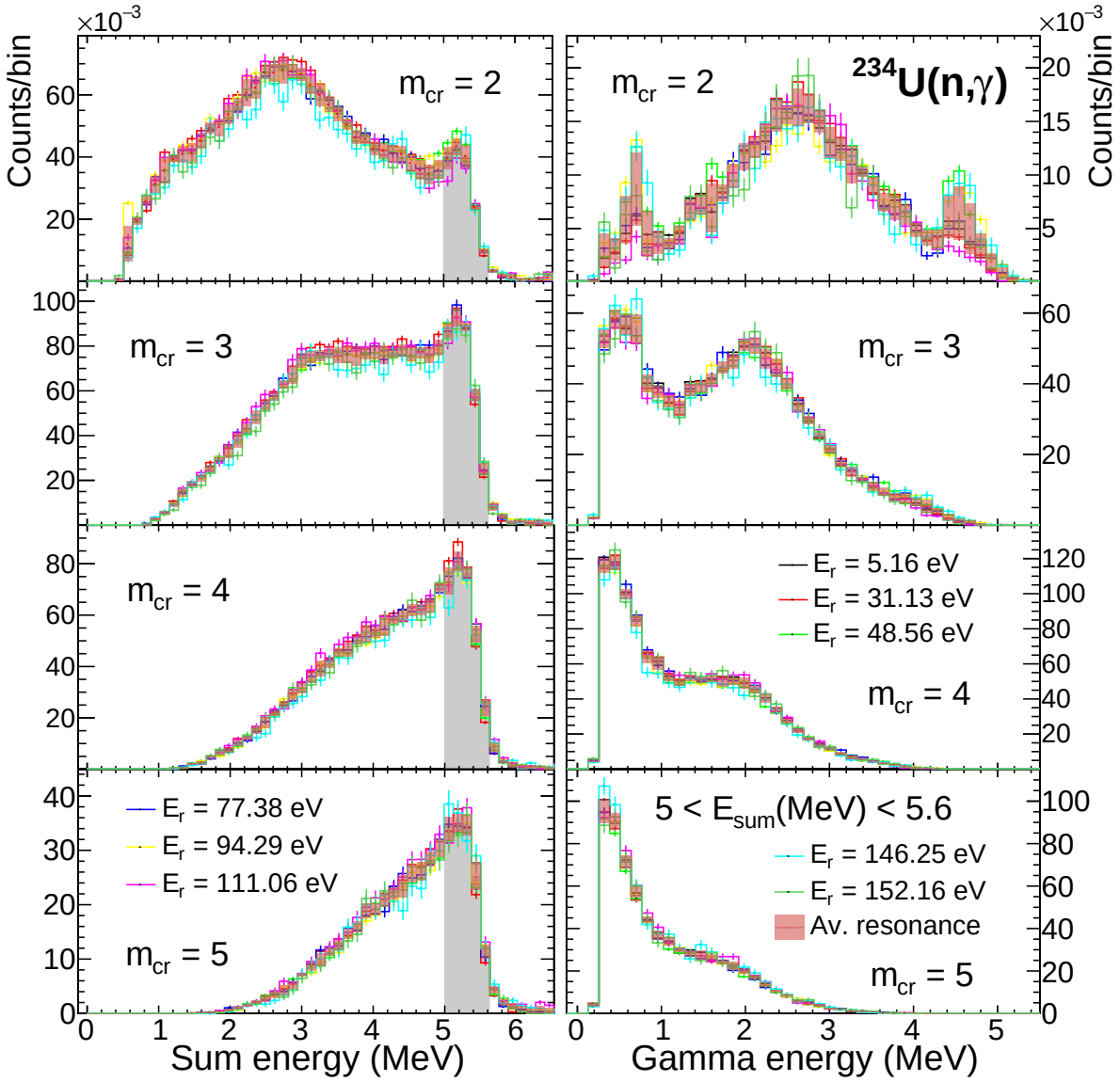

Figure 3.6: E_{sum} (left) and MSC (right) spectra of different resonances for each m_{cr} after background subtraction for ^{234}U(n, γ). The reddish band represents the average resonance spectra whose standard deviation is representative for the fluctuation of each single resonance.

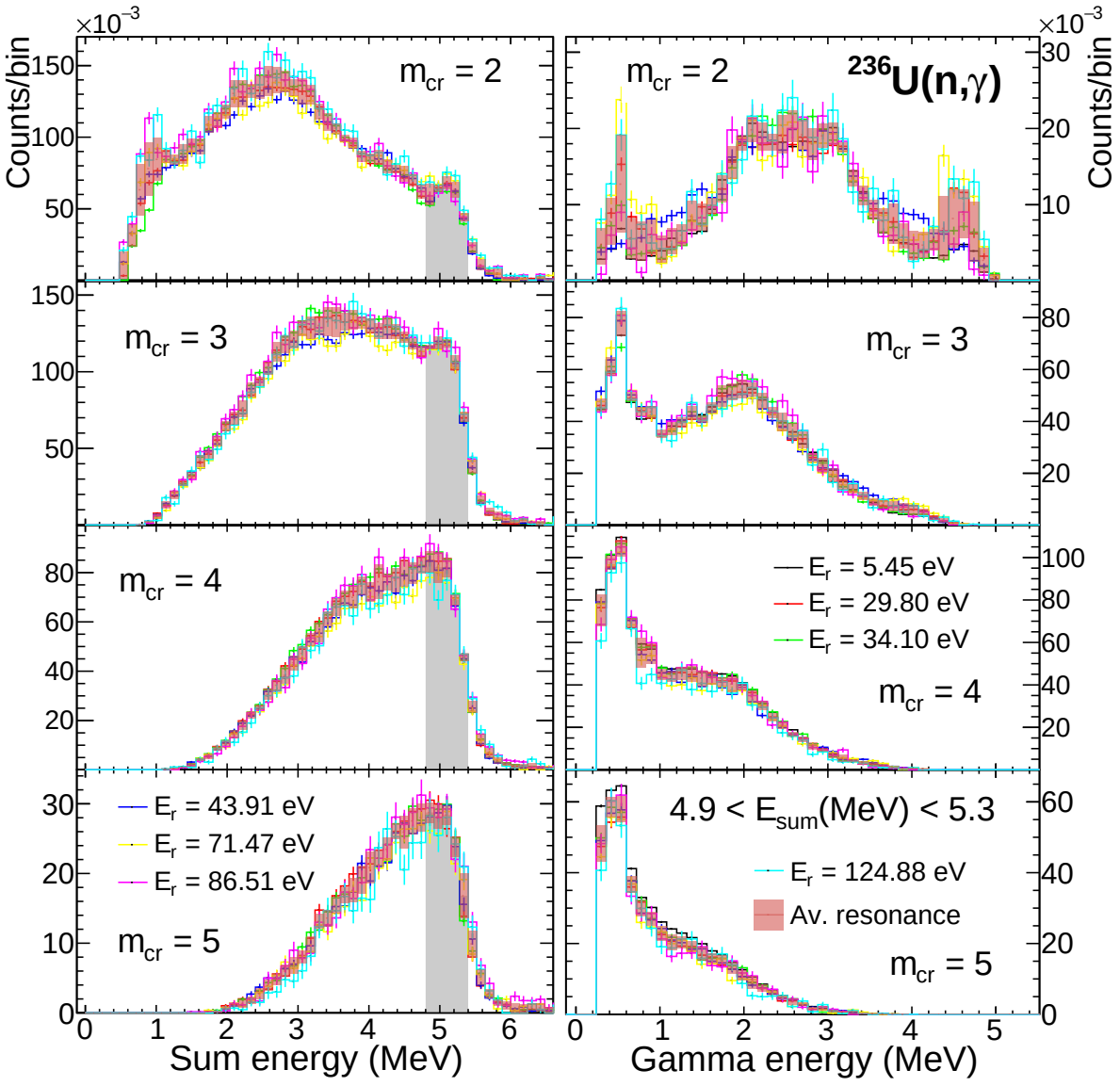

Figure 3.7: The same as Fig. 3.6 for ^{236}U(n, γ).

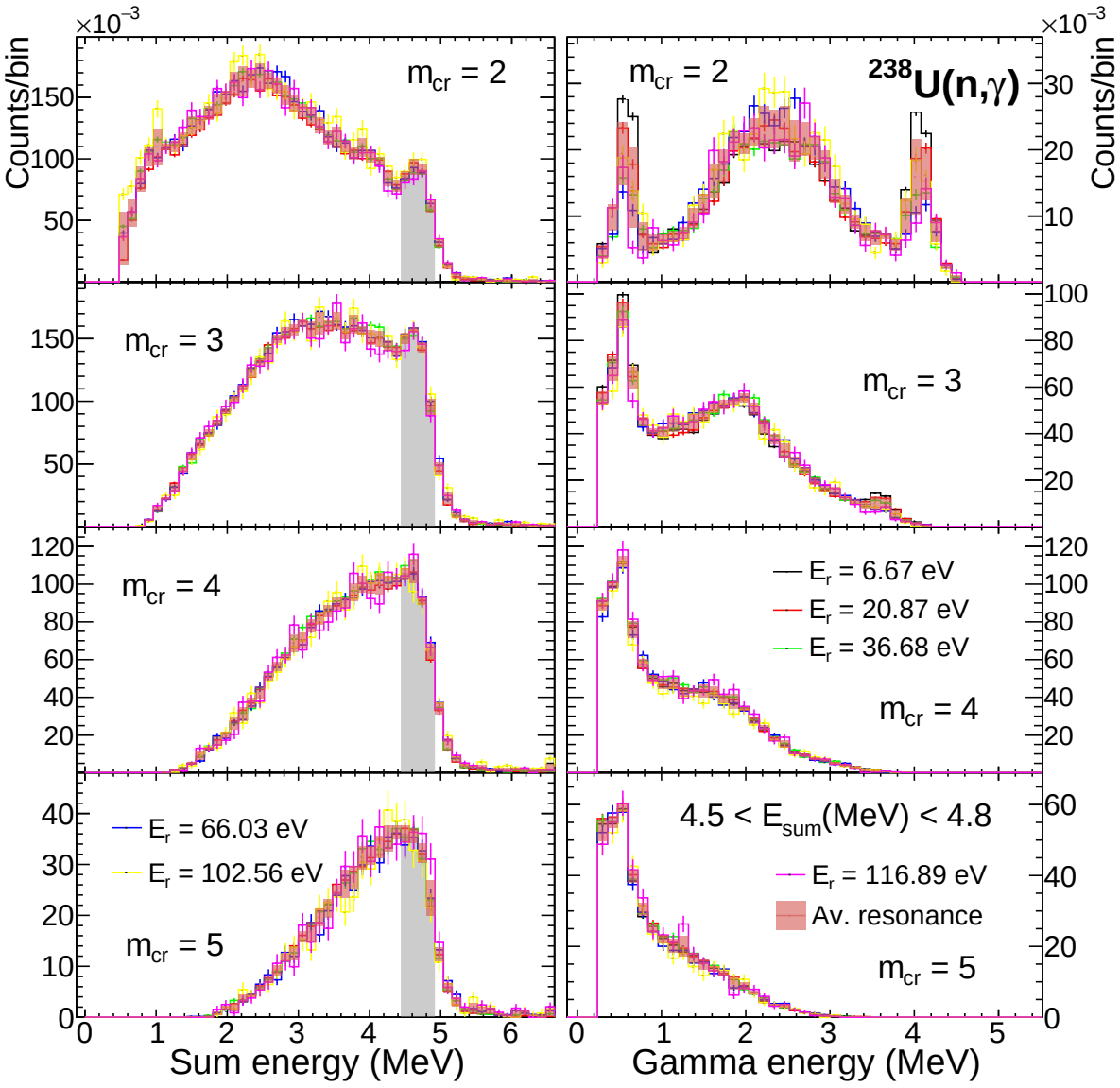

Figure 3.8: The same as Fig. 3.6 for ^{238}U(n, γ).

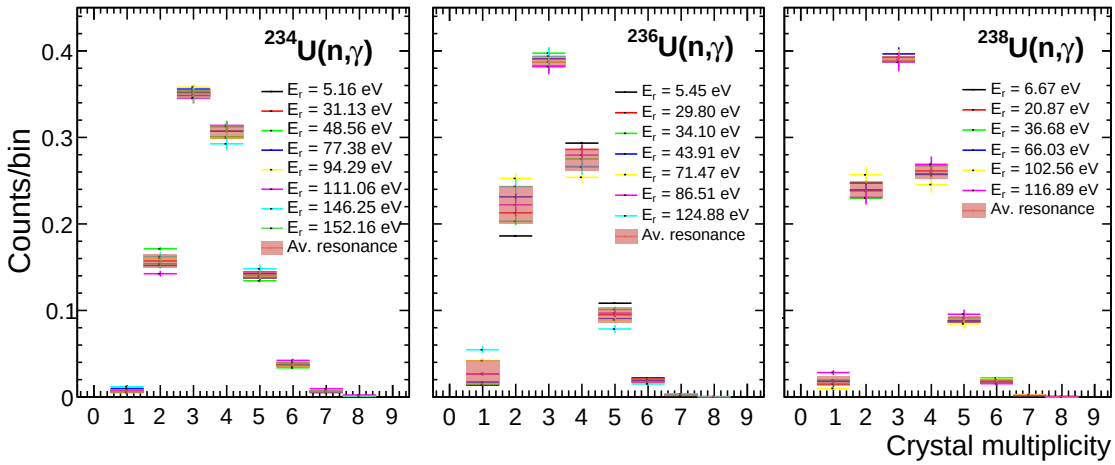

Figure 3.9: Crystal multiplicity distribution for single resonances after background subtraction (solid line) and for average resonance (reddish band).

measurements we rely on a quantity Δ^2_ν defined by:

$$\Delta^2_\nu = \frac{1}{\nu}\sum_{i=1}^{\nu}\frac{(S_{\mathrm{sim},i} - S_{\mathrm{exp},i})^2}{\Delta S^2_{\mathrm{sim},i} + \Delta S^2_{\mathrm{exp},i}} \tag{3.1}$$

where S_{exp} and S_{sim} are the experimental and simulated spectra, ΔS_{sim} and ΔS_{exp} correspond to the standard deviations of the spectra resulting essentially from the Porter Thomas fluctuations, and ν is the degree of freedom. This coefficient of agreement will be used to choose the simulation that best reproduces the experimental data when the different LD models are combined with the PSF models and to synthetize the results of several simulations.

First, in Sec. 3.2.1 we compare the TAC data with the phenomenological and semi-microscopic models and parameters available in the literature. Then, in Sec. 3.2.2 we propose a more detailed study using the DICEBOX code with PSF and LD combinations which reproduce better the data while in Sec. 3.2.3 we compare with the results of FIFRELIN. Finally, in Sec. 3.2.4 and 3.2.5 we study the sensitivity of the parameters in the simulations and the relation between $E1$ and $M1$ PSFs.

3.2.1 Comparison with models and parameters from literature

The ^{234,236,238}U(n, γ) reactions have already been studied from different experiments in previous works. A combination of LD and PSF models, and parameters can be taken from RIPL-3 database [21] in which only one SLO term for the $M1$ PSF is recommended, or from recent original works, in particular:

- The analysis of d- and ^{3}He-induced reactions on actinide targets performed at the Oslo Cyclotron Laboratory (OCL) [6].

- The measurement of multi-step gamma-ray energy spectra from resonant neutron capture on uranium samples with DANCE calorimeter [7].

In both studies a sum of three SLO terms is adopted to describe the $M1$ PSF, one for the SF and two for the SC mode. The $E2$ transitions are not included in those works.

The combination of LD and $E1$ PSF models considered are different for each analysis. From the RIPL-3 database we use the GLO model with two Lorentzians for $E1$ PSF while the BSFG VE05 model is used for the LD. The parameters for the PSF are taken from ^{234}U(n,γ) and extended to the other isotopes. The OCL analysis uses the EGLO model with $k_0 = 1$ which is identical to GLO model with a constant temperature $T = 0.2$ MeV including one more Lorentzian around 7 MeV called pygmy $E1$ resonance. The parameters are a fit to the experimental data from Caldwell et al. [76] for photoneutron (γ,xn) and photofission (γ,f) cross sections. The LD proposed by OCL could be described by a CT model with $T = 0.4$ MeV and a spin cut-off from Ref. [15] for the BSFG model which takes a value of $\sigma_c = 8.02$ at the neutron separation energy. Finally, the DANCE analysis concludes that a good reproduction of the experimental data is provided by the MGLO model with $k_0 = 3$ and a fixed temperature $T = 0.5$ MeV using two Lorentzians and the CT VE05 model for the LD. The parameters for the PSF are taken from fits of the photoabsorption cross section of ^{239}Pu in ref. [34] and is scaled by a factor 0.5. The PSF parameters used in the different calculations are collected in Table 3.2.

In Fig. 3.10 we compare the experimental data with DICEBOX simulations using the PSFs parameters taken from (i) the RIPL-3 database [21], (ii) the analysis of d- and ^{3}He-induced reactions at OCL [6] and (iii) the DANCE analysis [7]. The normalization of all simulated spectra is done in the sum peak for the same conditions as experimental data. We only show the E_{sum} and MSC spectra for ^{234}U(n, γ) as representative to get some conclusions. The spectra for the other uraniums are shown in appendix B, Figs. B1 and B2. The simulations are represented with a coloured band which indicates the standard deviation due to different nuclear realizations. In addition, it is important to note that the statistical uncertainties are much smaller than the standard deviation. Notable differences can be observed between the results of the combinations and parameters of LD and PSF in the literature:

- The RIPL-3 analysis presents large differences for both observables giving the worst results.

- The OCL combination improves the trends of the simulation but differences still exist. The improvement is produced by the introduction of the SC mode of the $M1$ PSF which is responsible for the bump appearing in the middle of the MSC spectra. However, the intensity of the $E1$ transitions with a contribution of the pygmy resonance is high.

- The simulation performed with the combination from DANCE analysis gives a good agreement with the experimental spectra for the three uranium isotopes. This is achieved by decreasing the intensity for $E1$ strength which was scaled by a factor 0.5 and by using the SC mode to describe the $M1$ transitions whose parameters were adjusted to reproduce the data.

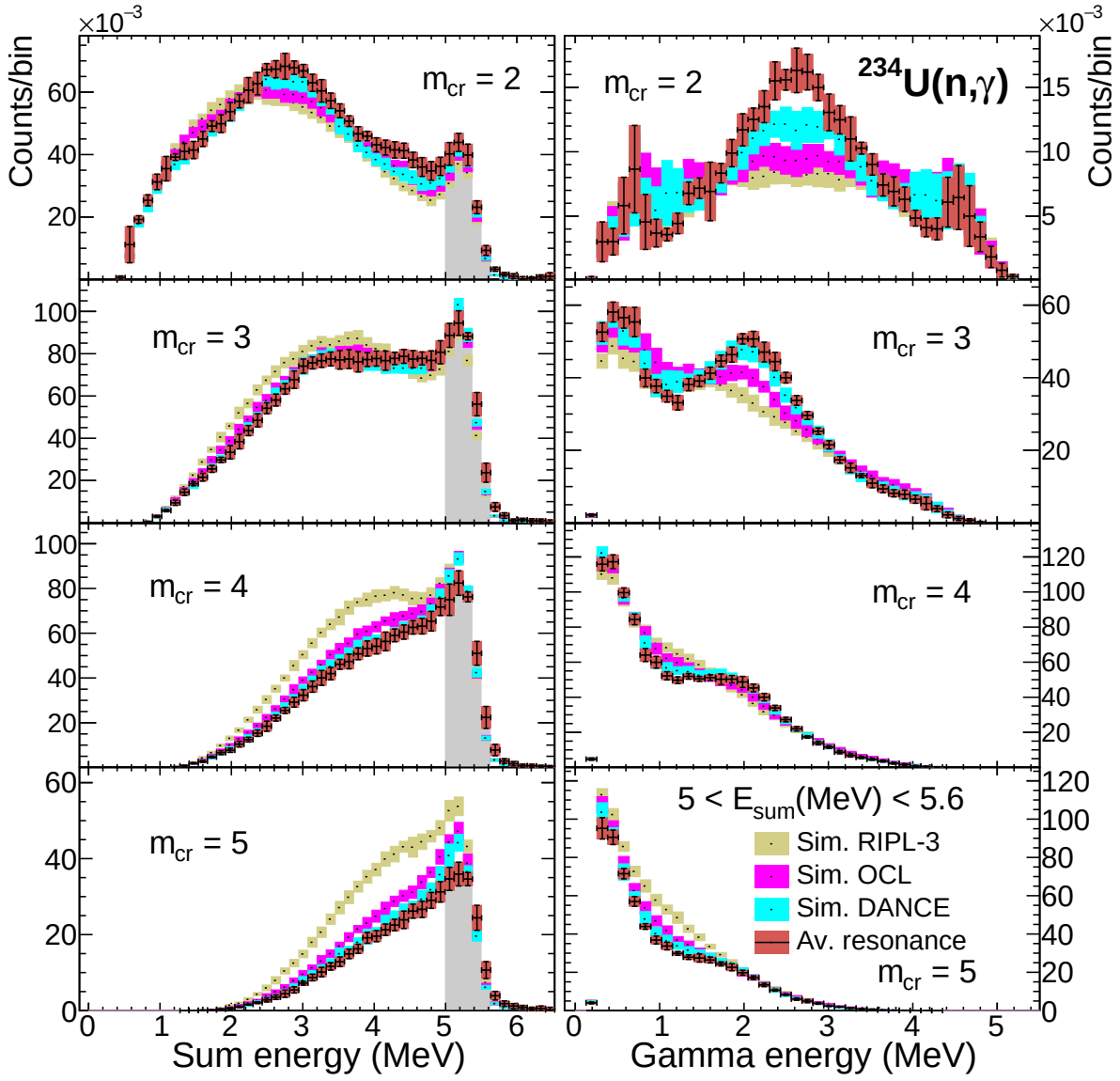

Figure 3.10: Comparison of the E_{sum} (left) and MSC (right) spectra for ^{234}U(n, γ) reactions of the n_TOF data with simulations using the LD and PSF models as recommended in RIPL-3 database [21] (mustard), and as published from OCL [6] (pink) and DANCE [7] (blue). The crystal multiplicity and sum energy conditions are specified in the figures.

Table 3.2: Parameters from RIPL-3 [21], OCL [6] and DANCE [7] for the PSFs.

	$E1$ PSF			$M1$ PSF		
Model	E (MeV)	Γ (MeV)	σ (mb)	E (MeV)	Γ (MeV)	σ (mb)
RIPL-3 [a]	11.11	1.12	243.3	–	–	–
	13.41	4.98	426	–	–	–
	–	–	–	6.61	4.00	2.35
OCL [b]	11.40	4.20	572	2.15	0.80	0.45
	14.40	4.20	1040	2.90	0.60	0.40
	7.30	2.0	15.0	6.61	4.00	7.00
OCL [c]	11.40	4.20	572	2.00	0.80	0.40
	14.40	4.20	1040	2.80	1.20	0.30
	7.30	2.0	15.0	6.61	4.00	7.00
DANCE [a]	11.28	2.48	325	2.15	0.80	0.60
	13.73	4.25	384	2.90	0.60	0.53
	–	–	–	6.61	4.00	1.50

a) ^{234,236,238}U(n,γ)

b) ^{234,236}U(n,γ)

c) ^{238}U(n,γ)

However, the $E1$ PSF used for OCL and DANCE contradicts the experimental values of the PSF around GEDR energy from Caldwell et al. [76] as seen in Fig. 3.11.

On the other hand, we have studied the tabulated values of LD based on HFB plus combinatorial model [24] presented in Sec. 1.1.5 and PSF from the D1M+QRPA calculations with non-zero limit at low E_γ [69] shown in Sec. 1.2.5. The semi-microscopic models have already been studied in ref. [69]. The LD for ^{238}U(n,γ) is not renormalized because the reproduction of the value D_0 worsens while the values of the parameters for the non-zero limit of the PSF are $f_0 = 1 \cdot 10^{-10}$ MeV^{-4}, $E_0 = 4$ MeV, $C = 1 \cdot 10^{-8}$ MeV^{-3} and $\eta = 0.8$ MeV^{-1} for the three uranium isotopes. The comparison with the E_{sum} and MSC spectra of the n_TOF data is shown in Fig. 3.12, 3.13 and 3.14 for ^{234,236,238}U(n, γ) respectively. We observe that for ^{236}U(n, γ) the simulation produces a good agreement with the experimental data while for ^{234}U(n, γ) and ^{238}U(n, γ) this is only achieved for $m_{cr} \geq 4$. For lower crystal multiplicities, $m_{cr} \leq 3$, differences are clearly visible in the MSC spectra of these two uranium isotopes and improvements can still be done.

Finally, we study the TRW calculated by the simulations corresponding to the decay of $1/2^+$ resonances at S_n for combination of LD and PSF present in the literature. The results are collected in table 3.3. The evaluated values of Γ_γ present important variations depending on the reference used. The values from JEFF-3.3 and ENDF/B-VIII.0

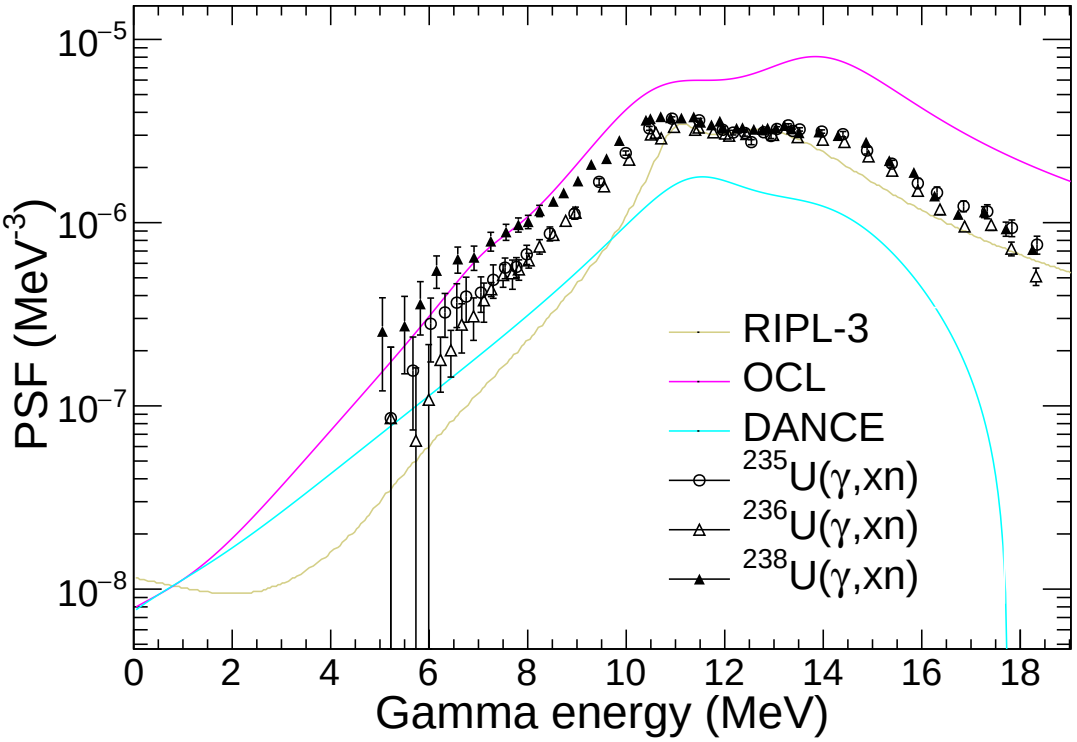

Figure 3.11: Comparison of the experimental PSF calculated from the photoabsorption cross section around the GEDR energy for ^{234,236,238}U(n, γ) from Caldwell et al. [76] with the E1 PSF models used from the RIPL-3 database [21] (mustard) whose parameters are taken from ^{234}U(n, γ) and are used to the other isotopes, OCL [6] (pink) whose parameters derived from (γ,x) cross sections on ^{236,238}U by Caldwell et al. [76] and DANCE [7] (blue) where parameters were taken from fits to ^{239}Pu photoabsorption cross-section data and scaled by a factor 0.5.

database were calculated by doing the mean value between the Γ_γ of the resonances used in this work. The evaluated uncertainty is missing in those databases. The uncertainty in the simulated values indicates the expected fluctuations of the TRW due to different nuclear realizations produced by DICEBOX. It is observed that the phenomenological study from RIPL-3 understimates the values of the TRW for the three uranium isotopes, while from OCL and DANCE the TRW are in a good agreement with some reference for ^{236}U(n,γ) but understimate them for the other two isotopes. Finally, the semi-microscopic simulations give coherent values of the TRW with the evaluated ones except perhaps for ^{234}U(n,γ).

3.2.2 Improvement of models and parameters

Previous works in the literature using phenomenological models showed the importance of introducing the SC mode in the $M1$ PSF and modifying the intensity of $E1$ and $M1$ strengths in the simulations in order to reproduce the experimental data. In this

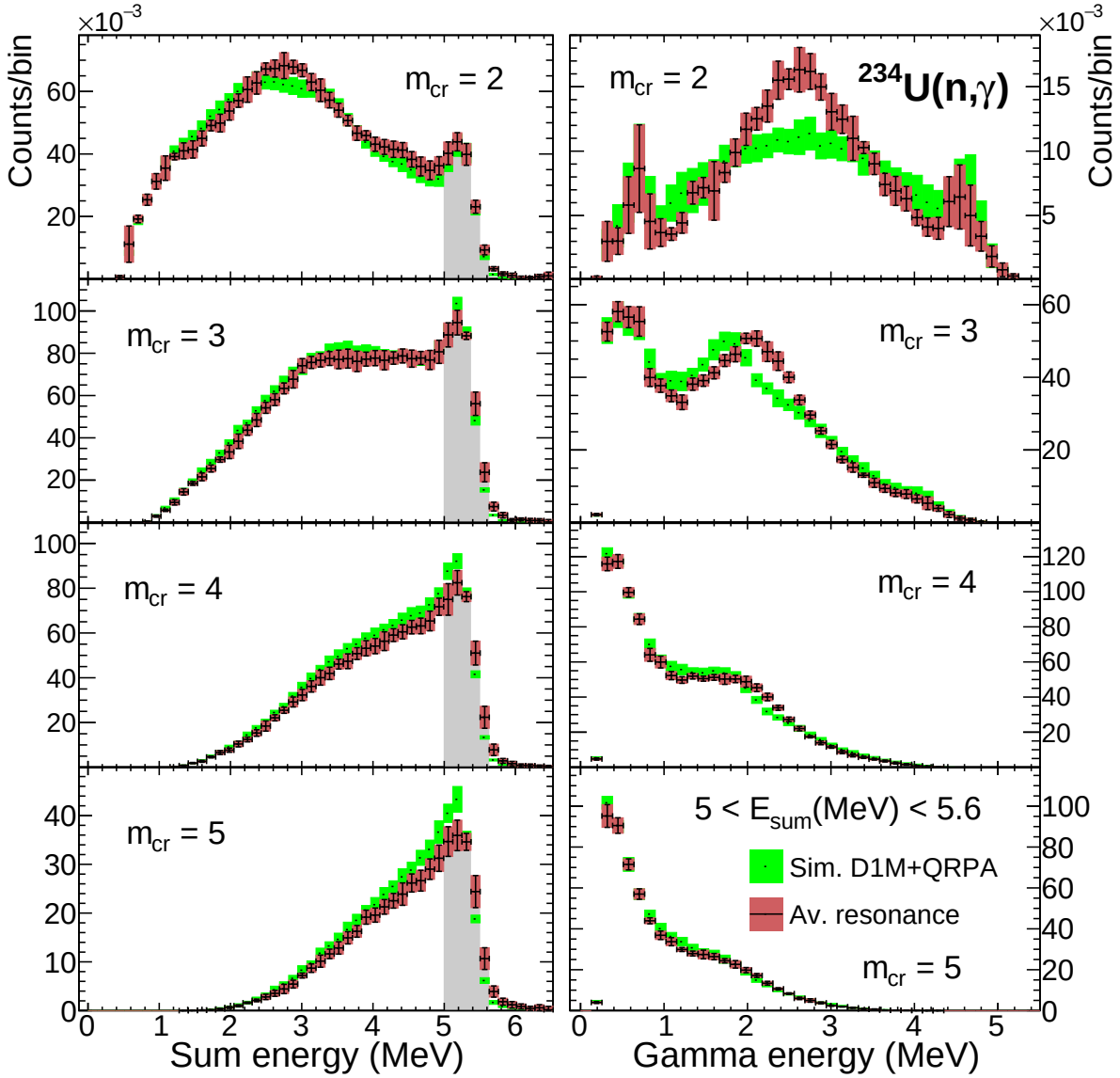

Figure 3.12: Comparison of the E_{sum} and MSC spectra for ^{234}U(n, γ) reactions of the n_TOF data with simulations from semi-microscopic models of LD based on HFB plus combinatorial model [23] and PSF based on the D1M+QRPA calculations with non-zero limit at low E_γ [69].

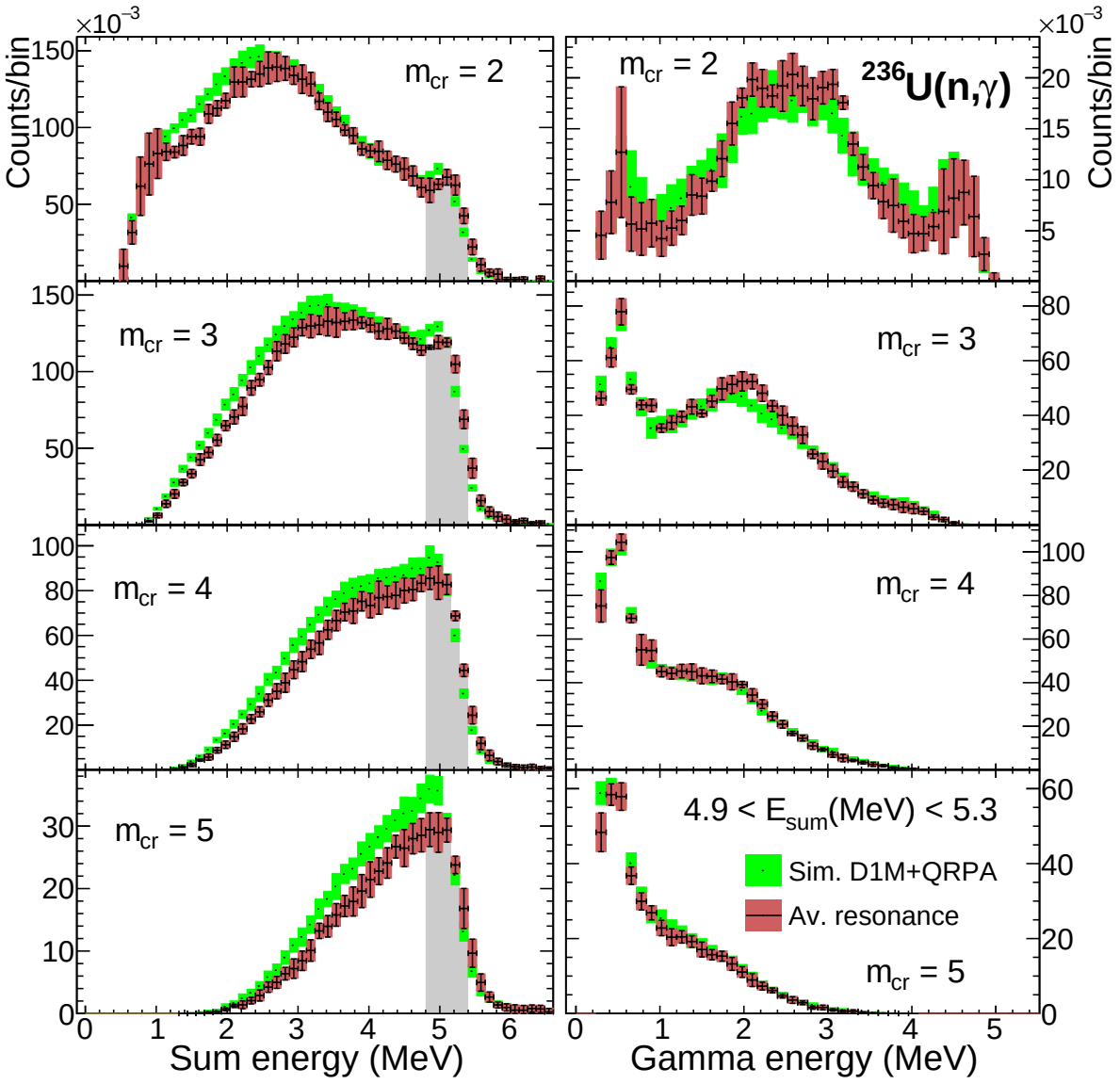

Figure 3.13: Same as Fig. 3.12 but for ^{236}U(n, γ) reactions of the n_TOF data.

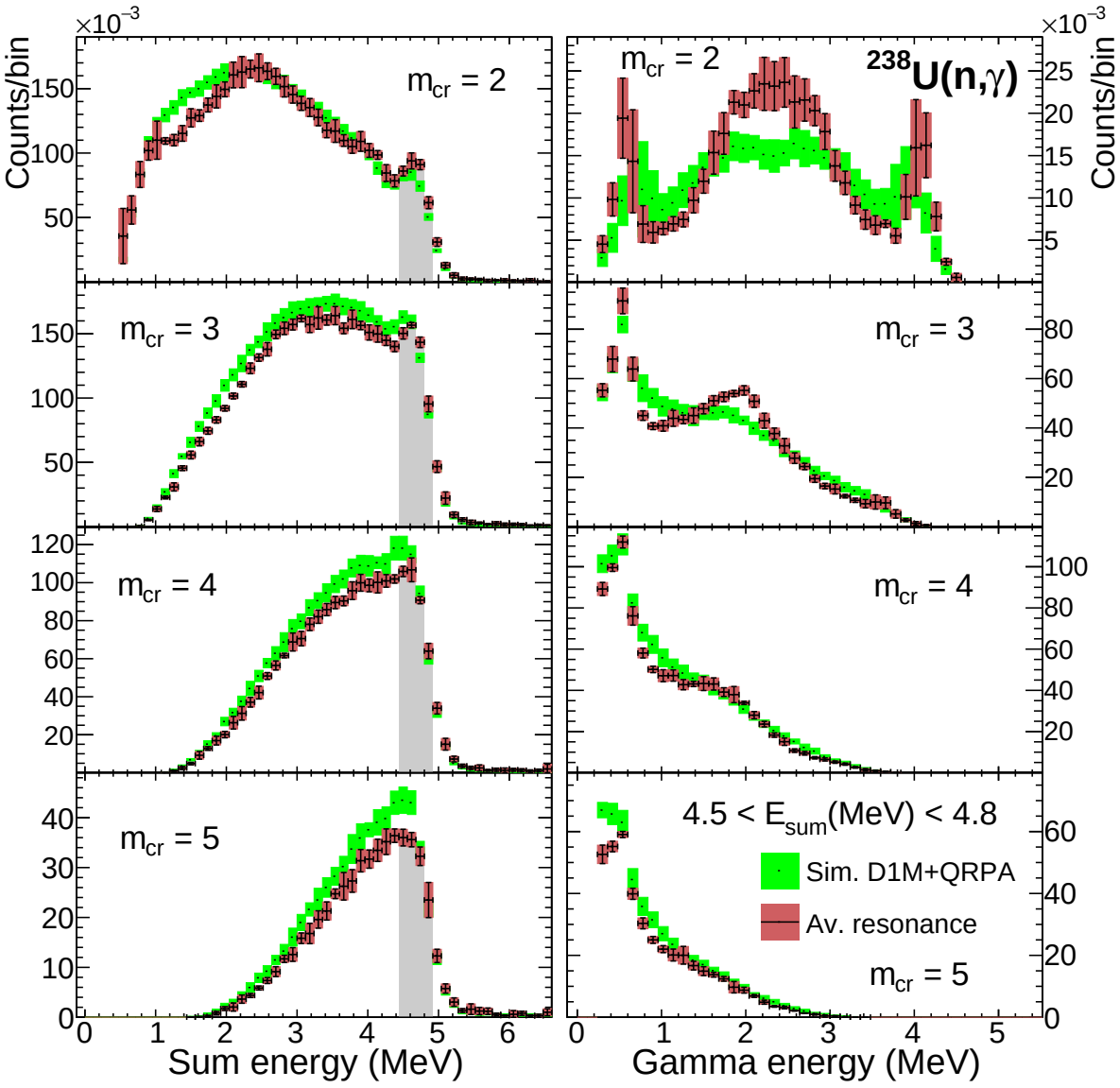

Figure 3.14: Same as Fig. 3.12 but for ^{238}U(n, γ) reactions of the n_TOF data.

Table 3.3: Total radiation widths Γ_γ of s-wave resonances ($1/2^+$) obtained with the different combination of LD and PSF in the literature. The values from JEFF-3.3 and ENDF/B-VIII.0 databases are calculated by doing the mean value between the Γ_γ of the resonances used in this work and collected in table A1 of appendix A.

	Γ_γ (meV)		
Model	n + ^{234}U	n + ^{236}U	n + ^{238}U
RIPL-3 [21]	16.1(2)	12.9(2)	9.5(2)
OCL [6]	19.9(4)	20.4(6)	18.6(8)
DANCE [7]	22.0(5)	17.2(4)	15.9(6)
D1M+QRPA [69]	29.4(6)	21.1(5)	22.2(4)
Evaluation [108]	25.3(1)	23.4(8)	23.36(31)
Evaluation [109]	36.7(7)	23.4(8)	22.9(4)
JEFF-3.3 [110, 111]	26.5	21.2	22.5
ENDF/B-VIII.0 [112]	26.5	18.5	22.5

work we use the n_TOF data to select after an exhaustive search consistent models and parameters for the $E1$ PSF and adjustment of the $M1$ strength in combination with LD models. First, we study all possible PSF + LD combinations using the models presented in Sec. 1.2 to find which ones present the best agreement with the experimental data taking into account the coefficient of agreement Δ^2_ν and then, we use the TRW values to discriminate between simulations. Because hundreds of simulations have been tested using the DICEBOX code, here we only show the conclusive and more interesting combinations.

Study of level density (LD) and photon strength function (PSF)

From the $E1$ PSF models introduced in Sec. 1.2 the SLO is well known to not reproduce the experimental observables in combination with any LD model independently of the chosen parametrisation of the $M1$ PSF while the KMF model does not agree with the experimental PSF around GEDR. Thus, we used the generalised ELO, GLO, EGLO and MGLO $E1$ PSF models which agree with PSF data around the GEDR and paired them with a suitable LD model allowed a satisfactory description of the experimental data after adjusting the parameters of the $M1$ PSF and the k_0 parameter.

The parameters for the $E1$ PSF for the different models are obtained by trying to reproduce the experimental data as best as possible at GEDR (9 MeV - 16 MeV) from Caldwell et al. [76] as seen in Fig. 3.15, while for the $M1$ PSF the parameters are adjusted to reproduce the n_TOF experimental spectra. We define the generalised $E1$ models with two Lorentzians which is usual for actinides because the introduction of the pygmy resonance in OCL combination in the previous section does not improve the results, while for the $M1$ PSF a sum of three SLOs is adopted to describe it, one for the

Table 3.4: Parameters of the PSFs. The $E1$ model is indicated in the first column while for $M1$ and $E2$ strengths the SLO model is always used. The set of parameters $E1$ and $M1$ PSFs can be used for the three uranium isotopes but for $E2$ PSF each isotope has specific values calculated from ref. [46] which are shown under the table.

	$E1$ PSF			$M1$ PSF		
E1 Model	E (MeV)	Γ (MeV)	σ (mb)	E (MeV)	Γ (MeV)	σ (mb)
ELO	10.90	2.30	398.0	2.15	0.80	0.25
($T(E)$)	14.16	5.15	409.0	2.90	0.60	0.30
	–	–	–	6.61	4.00	1.25
MGLO	10.90	2.30	358.0	2.15	0.80	0.98
($k_0 = 1.8$,	13.96	4.75	459.0	2.90	0.60	0.82
$T = 0.3$ MeV)	–	–	–	6.61	4.00	3.05
MGLO	10.90	2.30	338.0	2.15	0.82	1.07
($k_0 = 2.5$,	13.96	4.75	490.0	2.90	0.65	1.04
$T = 0.3$ MeV)	–	–	–	6.61	4.00	3.45
MGLO	10.90	2.30	328.0	2.15	0.95	1.30
($k_0 = 3.0$,	13.96	4.75	519.0	2.90	0.89	1.25
$T = 0.3$ MeV)	–	–	–	6.61	4.00	3.95
MGLO	11.00	2.50	399.0	2.15	0.70	0.78
($k_0 = 1.8$,	14.11	4.22	452.0	2.90	0.80	0.98
$T(E)$)	–	–	–	6.61	4.00	2.50
MGLO	10.85	1.94	315.0	2.15	0.70	0.90
($k_0 = 2.5$,	13.85	4.86	517.0	2.90	0.80	1.21
$T(E)$)	–	–	–	6.61	4.00	2.85
MGLO	10.93	2.09	324.0	2.15	0.70	0.88
($k_0 = 3.0$,	14.06	4.74	542.0	2.90	0.80	1.28
$T(E)$)	–	–	–	6.61	4.00	3.10

a) ^{234}U(n,γ) E2 parameters: E = 10.21 MeV, Γ = 1.18 MeV, σ = 1.70 mb.

b) ^{236}U(n,γ) E2 parameters: E = 10.18 MeV, Γ = 1.13 MeV, σ = 1.72 mb.

c) ^{238}U(n,γ) E2 parameters: E = 10.15 MeV, Γ = 1.09 MeV, σ = 1.77 mb.

SF mode and two for the SC mode as in the OCL and DANCE analysis. The parameters for energy, width and cross section of the PSFs are collected in table 3.4 for the different models. In this work the $E2$ transitions are included in the simulations by taking the SLO model with one Lorentzian whose parameters are taken from ref. [46]. However, its influence is negligible. Finally, we only show the spectra obtained for LDs VE09 because they present comparable results to those obtained with LDs VE05. In addition, the CGCM model will not be used because it is equivalent to the CT formula as is shown in Sec. 1.1.6 because the excitation energies E_x of the three uranium isotopes are close

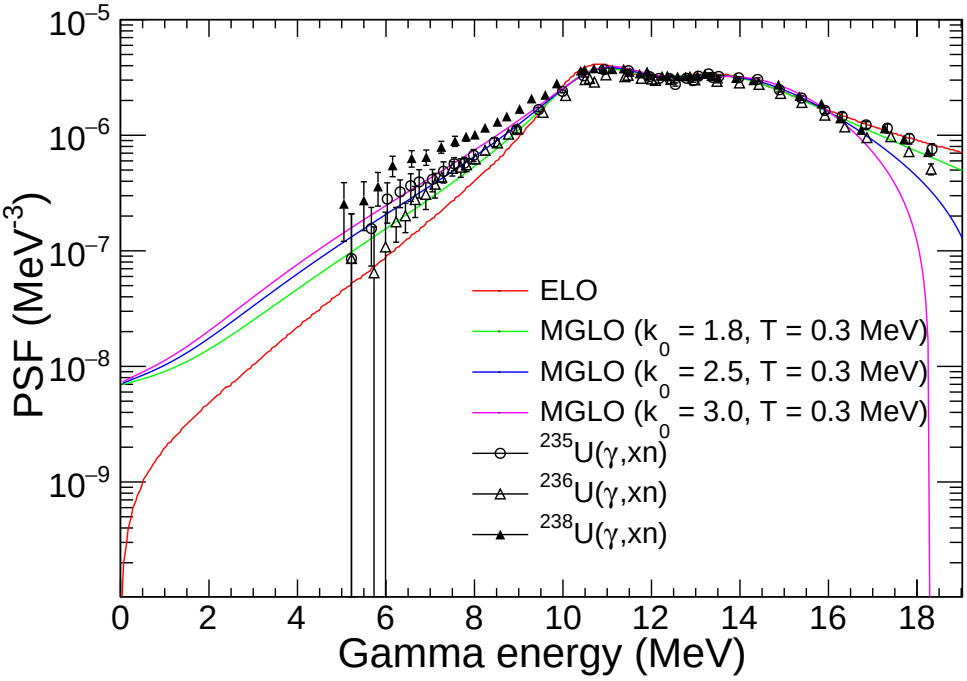

Figure 3.15: Comparison of the PSF formulas used for the simulations with ELO and MGLO with different k_0 values and $T = 0.3$ MeV. Experimental data of the PSF from Caldwell et al. [76].

to S_n ($E_x > S_n - 2$ MeV).

The ELO model with energy dependent temperature is combined with the BSFG and CT VE09 models and shown in Fig. 3.16 for ^{234}U(n,γ). The trends of the E_{sum} and MSC spectra are reproduced for both simulations but slight differences can be observed. The ^{236,238}U(n,γ) spectra present the same conclusion. In addition, to choose which combination best reproduces the experimental data we use the Δ_ν^2 of the E_{sum} and MSC simulated spectra which are shown in Fig. 3.18. The MSC spectra show the single gamma energies for complete cascades while the E_{sum} spectra depend on the energy deposited in the crystals and how the gamma rays escape from the TAC. We can observe that the E_{sum} spectra show a higher Δ_ν^2 than MSC because its results are more sensitive to the simulated geometry, materials, position of the source, and the resolution of the detector among others. Finally, despite the fluctuations between multiplicities there is a clear trend that the combination of the ELO model with BSFG produces a lower Δ_ν^2 than with CT for both observables. On the other hand, the mean value and the standard deviation of the crystal multiplicity distribution are collected in table 3.5 for each uranium isotope. We can observe again that the experimental crystal multiplicity distribution is always best reproduced for the BSFG combination. Finally, for the ELO model of the PSF we can conclude that BSFG obtains better results than CT as LD when analysing the different observables.

Conversely, performing an analysis similar to the previous one, the GLO, EGLO and MGLO models are in reasonable agreement with experimental data when the CT model

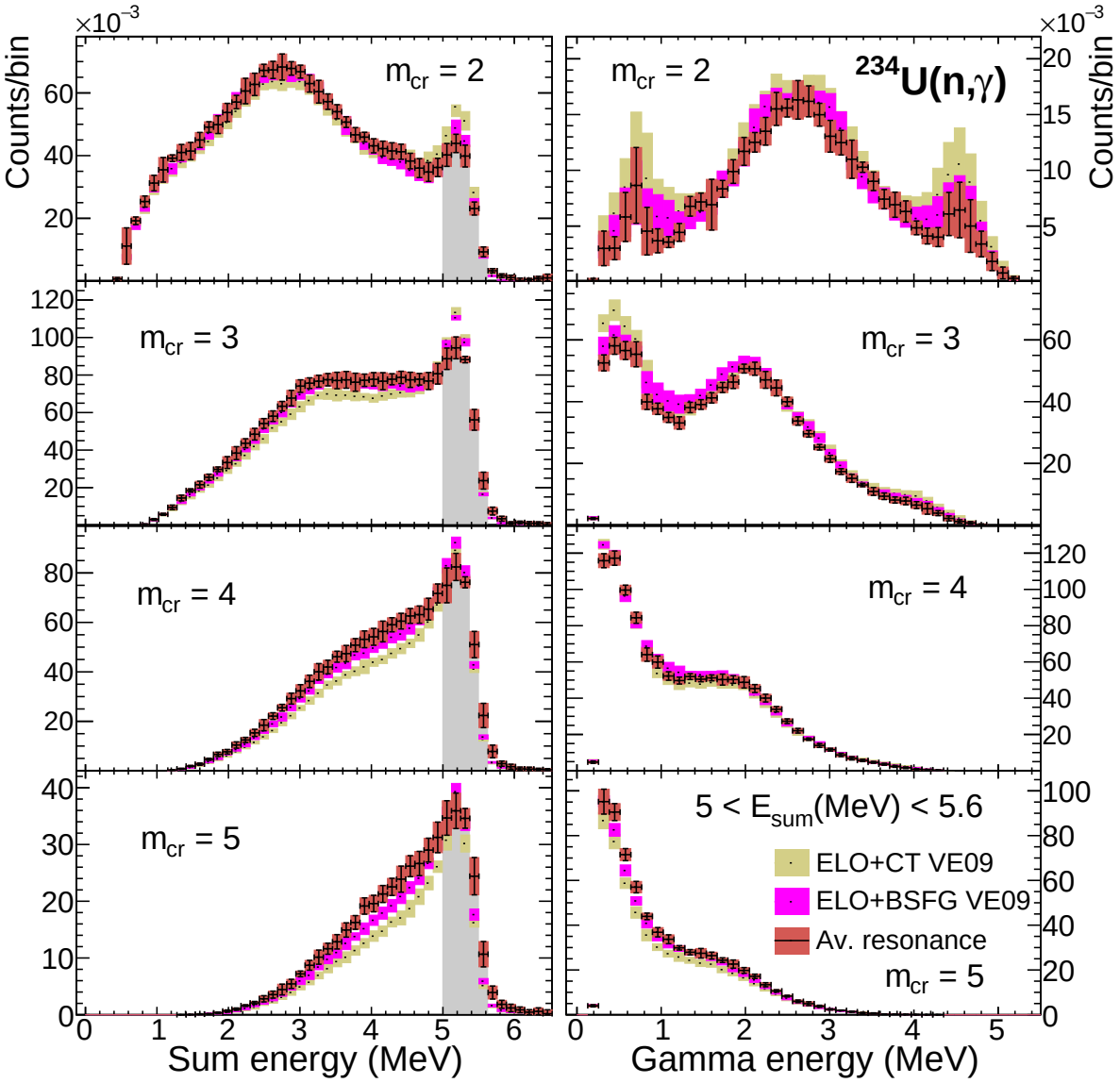

Figure 3.16: Average E_{sum} and MSC spectra of $1/2^+$ resonances in ^{234}U(n,γ) compared with simulations using ELO model for PSF with CT VE09 (mustard) and BSFG VE09 (pink) for LD.

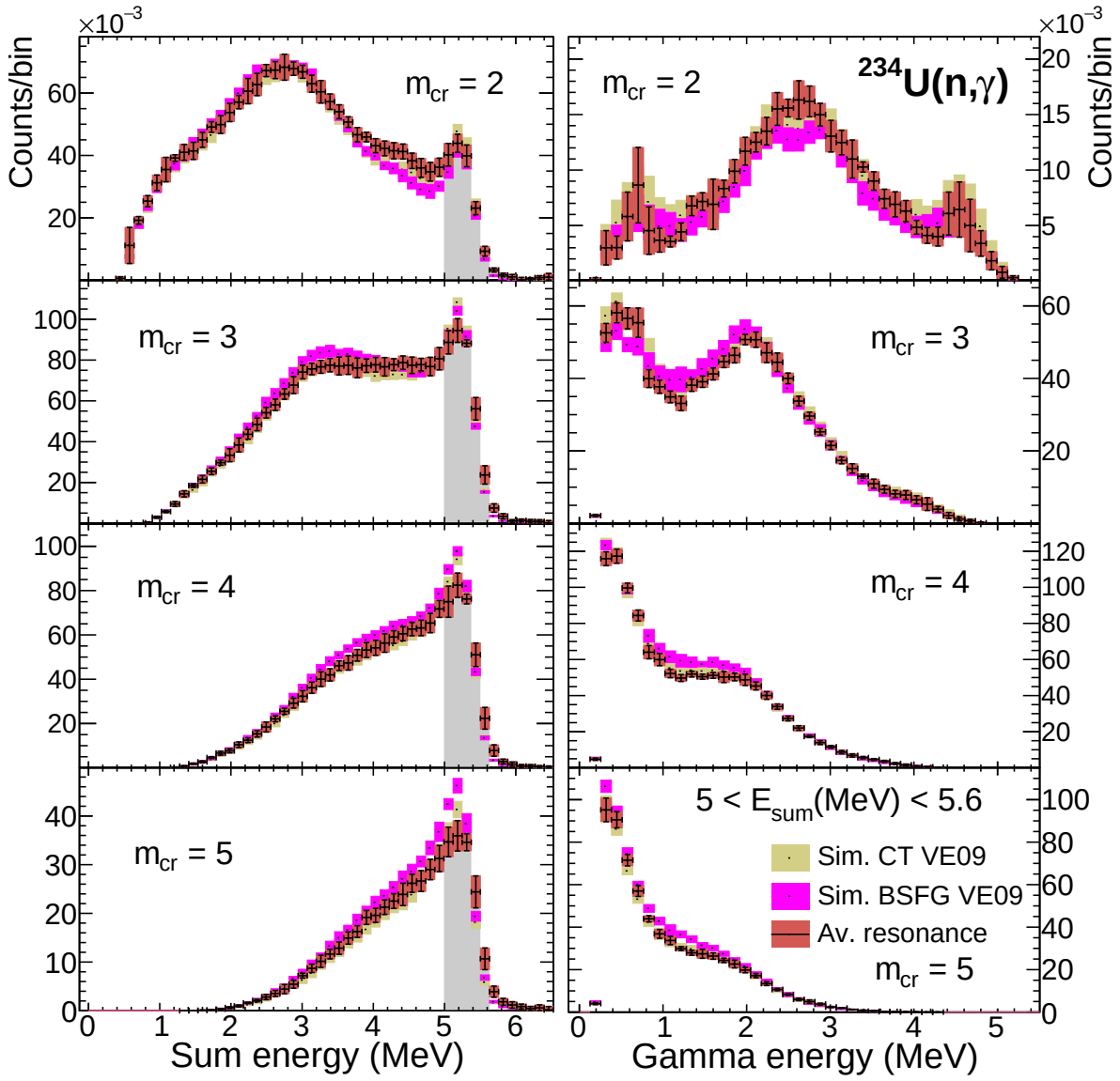

Figure 3.17: The same as Fig. 3.16 but using MGLO with $k_0 = 1.8$ and T = 0.3 MeV.

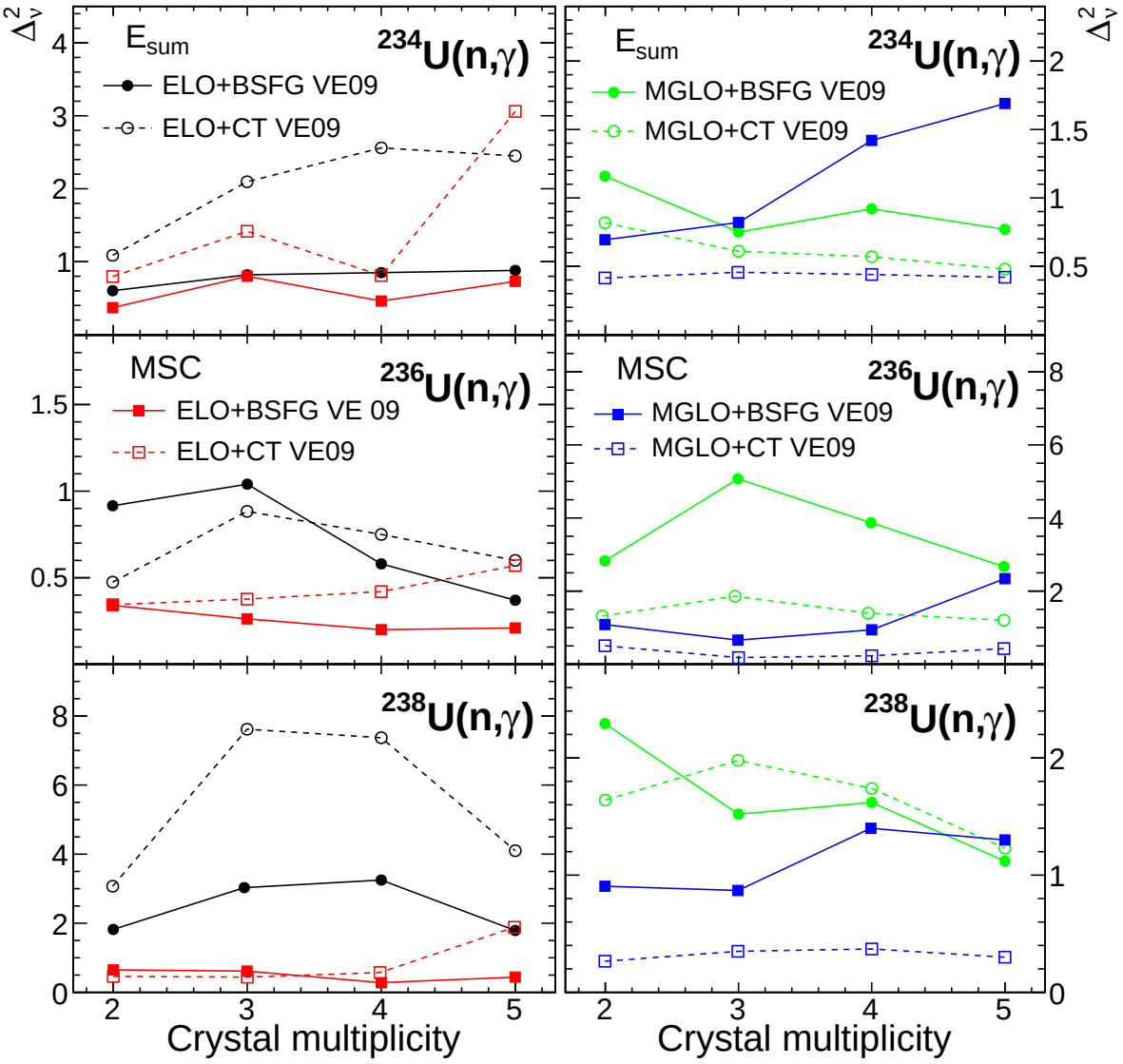

Figure 3.18: Δ_ν^2 of the simulations with ELO (left) and MGLO with $k_0 = 1.8$ and $T = 0.3$ MeV (right) as PSFs in combination with BSFG VE09 and CT VE09 for ^{234,236,238}U(n,γ) reactions. The lines are only plotted for a better visualization.

is used while getting a bit worse results for BSFG as LD. In this work, the case for MGLO only is shown because the GLO and EGLO models produce similar results when modifying the parameters slightly. Fig. 3.17 shows the simulated spectra for MGLO with $k_0 = 1.8$ and fixed temperature T = 0.3 MeV for both LD formulas. In this case the mean value and the standard devation of the crystal multiplicity distribution in table 3.5 produces a better result for CT while the study of the Δ^2_ν of the simulations for E_{sum} and MSC spectra in Fig. 3.18 presents mainly lower values for CT than for BSFG. Therefore, we can conclude that the MGLO model of the PSF produces better results in combination with CT as LD.

Table 3.5: Mean value and standard deviation of the crystal multiplicity distribution for each combination of PSF and LD of ^{234,236,238}U(n,γ) reactions and experimental values calculated from average resonance spectra.

Model		^{234}U(n,γ)		^{236}U(n,γ)		^{238}U(n,γ)	
PSF	LD [VE09]	Mean	Std dev	Mean	Std dev	Mean	Std dev
ELO	BSFG	3.49(1)	1.06(1)	3.29(3)	1.02(2)	3.22(1)	1.00(1)
ELO	CT	3.39(1)	1.06(1)	3.23(3)	1.01(2)	3.13(1)	0.98(1)
MGLO	BSFG	3.62(1)	1.09(1)	3.41(3)	1.05(2)	3.34(1)	1.02(1)
MGLO	CT	3.51(1)	1.08(1)	3.34(3)	1.03(2)	3.24(1)	1.02(1)
Experimental data		3.56(1)	1.09(1)	3.34(3)	1.05(2)	3.22(1)	1.02(1)

Study of the total radiative width (TRW)

As an additional constraint in the search of the best combination, we use the results of the TRW of s-wave resonances ($1/2^+$) at energy S_n obtained from simulations presented above for ELO and MGLO models. The values of the TRW calculated with the spread due to different nuclear realizations and a list of evaluated values from difference references are collected in table 3.6. We can draw important conclusions by analyzing separately the LD and PSF models.

Looking at the dependence with respect to LD, the TRW calculated with BSFG is always higher than when using the CT model. This behaviour is expected because BSFG increases the number of levels faster than CT below S_n. In addition, depending on which of the two versions of LD studied in this work (VE05 and VE09) we can see also small differences. These variations are produced by the different spin cut-off σ_c parameter used in both formulas which gives a slightly different behaviour below S_n, and for CT a different s-wave D_0 value as seen in Sec. 1.1.6. Thus, the TRW is very sensitive to the model of LD used.

Regarding the PSF, the TRW presents also important differences between ELO and MGLO models of $E1$ with adjusted $M1$ PSFs. The TRW calculated using ELO model gives always a lower value than the one calculated by MGLO. This behaviour is produced because the $E1$ strength is higher for the MGLO model below S_n than for ELO model as

Table 3.6: Total radiation widths Γ_γ of s-wave resonances ($1/2^+$) obtained with different models of PSF and LD. The MGLO model has a constant temperature of T = 0.3 MeV. The values from JEFF-3.3 and ENDF/B-VIII.0 databases are calculated in the same way as table 3.3.

Model		Γ_γ (meV)		
PSF	LD	n + ^{234}U	n + ^{236}U	n + ^{238}U
ELO	BSFG VE05	15.9(3)	12.9(2)	9.3(2)
ELO	BSFG VE09	16.7(2)	14.2(2)	9.7(3)
ELO	CT VE05	8.3(3)	6.2(2)	5.6(2)
ELO	CT VE09	7.9(2)	5.9(2)	4.4(9)
MGLO ($k_0 = 1.8$)	BSFG VE05	51.5(7)	43.2(7)	32.7(7)
MGLO ($k_0 = 1.8$)	BSFG VE09	53.0(6)	47.0(5)	33.6(9)
MGLO ($k_0 = 1.8$)	CT VE05	27.1(7)	21.1(4)	19.5(7)
MGLO ($k_0 = 1.8$)	CT VE09	25.2(5)	19.7(6)	15.4(3)
MGLO ($k_0 = 2.5$)	CT VE05	32.4(9)	25.1(6)	23.2(9)
MGLO ($k_0 = 2.5$)	CT VE09	30.3(7)	23.4(7)	18.3(3)
MGLO ($k_0 = 3$)	CT VE05	41(1)	32.3(7)	29.9(9)
MGLO ($k_0 = 3$)	CT VE09	38.8(9)	30.0(7)	23.5(4)
Evaluation [108]		25.3(1)	23.4(8)	23.36(31)
Evaluation [109]		36.7(7)	23.4(8)	22.9(4)
JEFF-3.3 [110, 111]		26.5	21.2	22.5
ENDF/B-VIII.0 [112]		26.5	18.5	22.5

seen in Fig. 3.15. Finally, we can see that the TRW obtained for the ELO combinations produce always a lower value of the TRW than the evaluated ones while for the MGLO model with $k_0 = 1.8$ and $T = 0.3$ MeV presents a better agreement with TRW in combination with CT model. In addition, for MGLO we can change the value of TRW by a modification of the parameter k_0.

To reproduce any evaluated value of TRW for the three reactions of this work we modify the parameter k_0 of the MGLO model. We only show two more simulations using CT VE05 and CT VE09 but a similar study can be done for, CGCM or other LD models which reproduces the experimental data. The TRW for ^{238}U(n,γ) from different references gives a stable value around 23 meV. As said before the TRW increases for higher intensity of the PSF, so we have to increase the k_0 parameter for ^{238}U(n,γ) because they presented a lower TRW with respect to the evaluated ones by using $k_0 = 1.8$. Finally, the TRW can be well calculated for ^{238}U(n,γ) using a value of $k_0 = 3$ and adjusting the parameters of $E1$ PSF to fit the experimental data at GEDR and the parameters of $M1$ PSF to reproduce the experimental data as shown in Fig. 3.20 for CT VE09 as LD. In

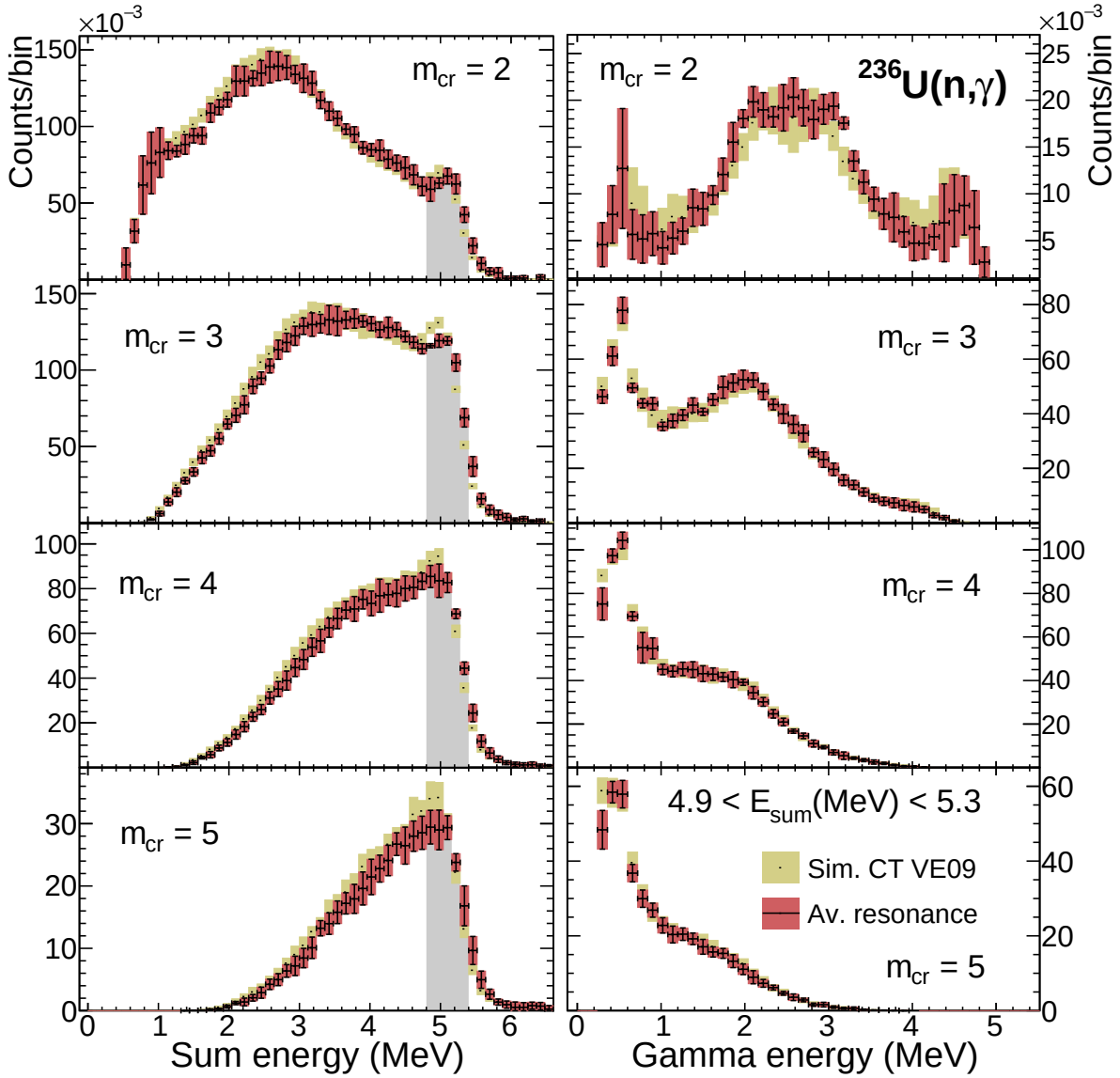

Figure 3.19: E_{sum} and MSC of $1/2^+$ resonances in ^{236}U(n,γ). The reddish band histograms correspond to the average experimental data from different resonances. The mustard band is the simulations with MGLO model with $k_0 = 2.5$ and T = 0.3 MeV for PSF and CT VE09 for LD.

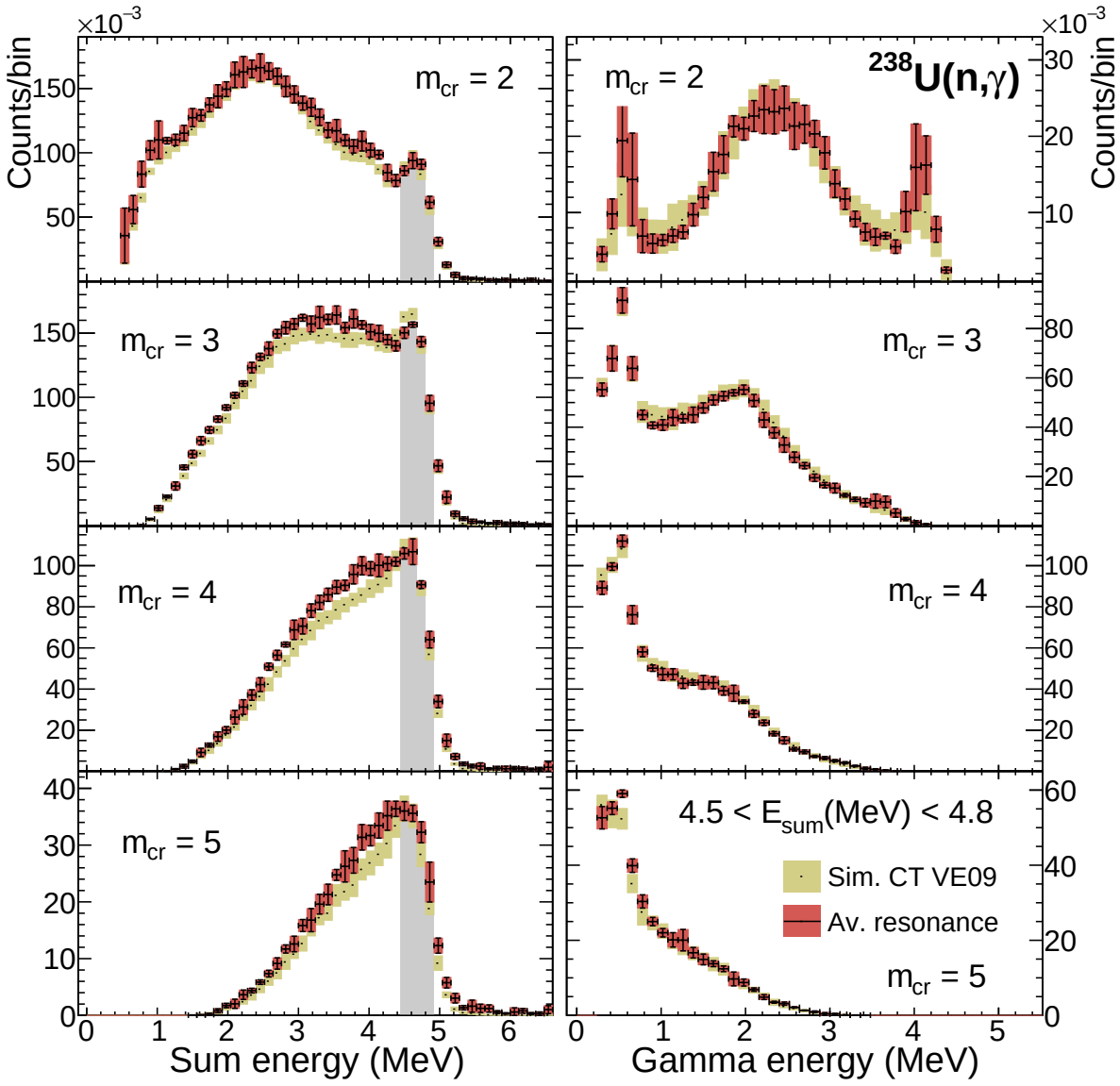

Figure 3.20: The same as Fig. 3.19 for ^{238}U(n,γ) using $k_0 = 3$.

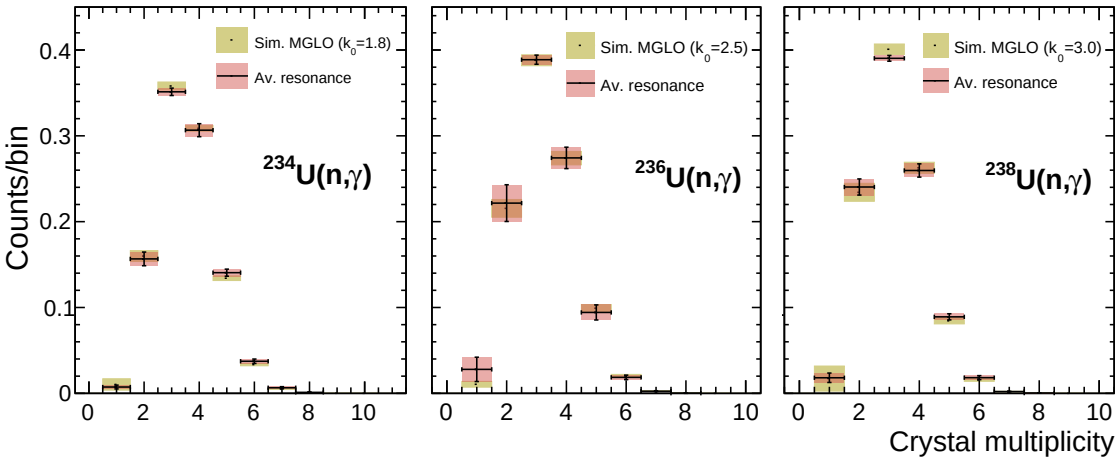

Figure 3.21: Comparison of the simulated crystal multiplicity distribution with the experimental data using MGLO with $k_0 = 1.8, 2.5$ and 3.0 for ^{234,236,238}U(n,γ) respectively.

addition, we show in Fig. 3.19 other simulation by using a value of $k_0 = 2.5$ for ^{236}U(n,γ) which presents a good agreement with the TRW from Mughabghab [108, 109] and with the experimental spectra for CT VE09 as LD. The parameters for these simulations are collected in table 3.4 and as mentioned in the previous section for MGLO with $k_0 = 1.8$ the simulations can reproduce the experimental data for the three uranium isotopes obtaining comparable results of the Δ^2_ν. In addition, the crystal multiplicity distribution for each uranium are shown in Fig. 3.21 presenting a good agreement with the trend of the experimental data.

We could conclude that for CT VE09 as LD the TRW and the n_TOF experimental spectra are reproduced for ^{238}U(n,γ) by using $k_0 = 3$ because the TRW presented slight variations between the references. However, for the other two isotopes the k_0 depends on the reference used. For ^{234}U(n,γ) we should use a k_0 between 2.5 and 3 to reproduce the TRW from ref. [109] while for the other references the TRW are reproduced by using a $k_0 = 1.8$. For ^{236}U(n,γ) a good value of TRW from JEFF-3.3 and ENDF/B-VIII.0 databases is calculated by using a $k_0 = 1.8$ but for refs. [108, 109] a $k_0 = 2.5$ is needed. However, if we use the CT VE05 as LD we find that the simulations need a lower k_0 value for each isotope in order to present a good agreement with the TRW, for instance ^{238}U(n,γ) gives a good results for $k_0 = 2.5$ by using CT VE05. This indicates that the intensity of the PSFs is strongly related to the LD formula used in the simulation. In general, it seems that MGLO model with $k_0 = 1.8$ and CT model is the only combination that produces TRW more or less consistent with the evaluated values for the three isotopes.

3.2.3 Comparison with FIFRELIN

As was introduced in Sec. 1.3.2 the FIFRELIN code uses default values for the $E_{cut-off}$, binning width and E_{bin}. We checked the validity of these default parameters in the

simulations in order to study their sensitivity in the results. To test the influence of $E_{cut-off}$ we compare two simulations of FIFRELIN, one using the default $E_{cut-off}$ value and the other with $E_{cut-off} = E_{crit}$, for ^{238}U(n,γ) as a representative case because the largest difference between these energies is observed for this reaction. We can observe in Fig. 3.22 that the relative differences between both simulations are around 1 in average for the E_{sum} and MSC spectra. These results indicate that the choice of $E_{cut-off}$ does not impact the simulation if its value is below the energy where the LD starts to decrease by lack of experimental information.

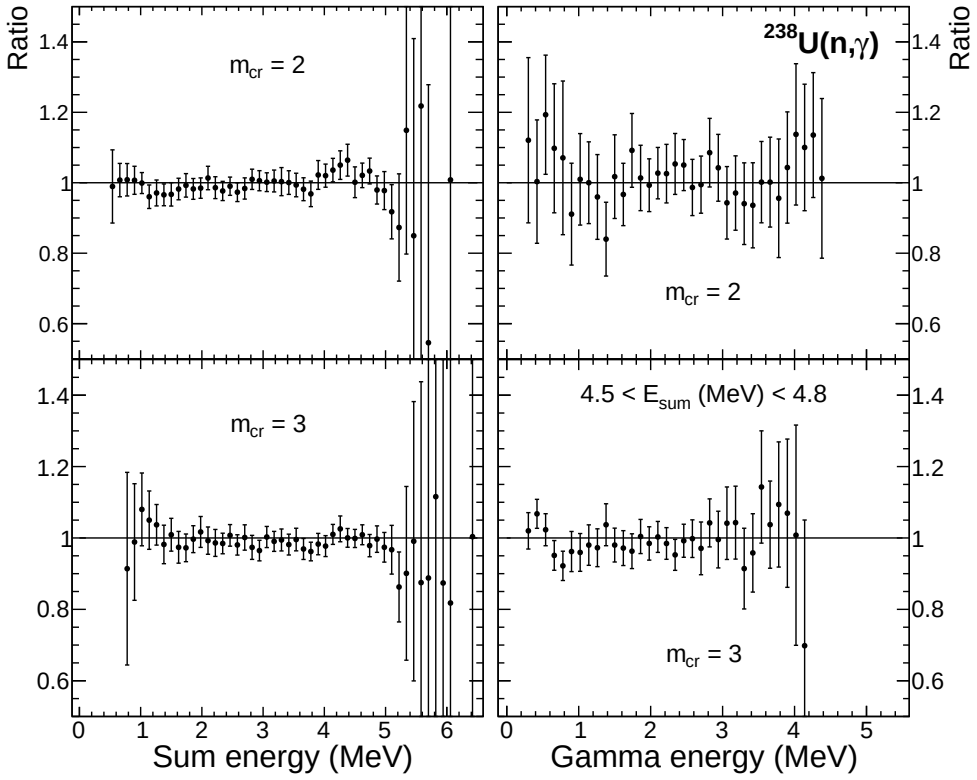

Figure 3.22: Ratio between simulations done with FIFRELIN for $E_{cut-off} = 0.373$ MeV from RIPL-3 default value and $E_{cut-off} = E_{crit} = 0.830$ MeV.

Now, we study the influence of the bin width in the simulations. For that we analyze also the single gamma spectra of the simulated cascades which are shown in Fig. 3.23 (top-left) for the ^{238}U(n,γ) reaction. We can observe that FIFRELIN decreases the number of gammas and presents an unrealistic high peaks structure below ~ 1.6 MeV when the default value of 10 keV for the binning width is used. This behaviour is produced because the 10 keV energy bins in the treatment of the continuum region lead to an abrupt change compared to the discrete representation of levels. This problem can be solved by decreasing the value of the binning of the continuum region to 1 keV. However, results of the full simulations with a binning of 10 keV and 1 keV are identical as seen in Fig. 3.23 (bottom) where the relative differences between both simulations are also around 1 in average for all spectra. This is because the energy grid used to plot the E_{sum} and MSC spectra is broad and these peaks of ~ 10 keV width will disappear when

we use the same grid for single gamma spectra as seen in Fig. 3.23 (top-right). The same results are obtained if instead of changing the binning width we increase the E_{bin} up to coincide with S_n. However, the simulation time is greatly increased when bins of 1 keV width or higher E_{bin} are used. After testing the influence of all default parameters in the FIFRELIN code, we can conclude that the simulated spectra for FIFRELIN remain unchanged for different values of E_{bin}, the bin width in the continuum region and $E_{cut-off}$ as long as it is below the energy where the experimental LD starts missing levels. For the next results we use the default values proposed by FIFRELIN for these parameters in order to decrease the simulation time.

On the other hand, FIFRELIN considers PSF = EGLO and LD = CGCM default models in fission calculations (deexcitation of fission fragments). To test the validity of these options against our experimental neutron capture data on actinides, we compare in Fig. 3.24, 3.25 and 3.26 the simulated spectra using these default parameters and models with the simulated spectra using the parameters proposed in table 3.4 for the MGLO model with $T = 0.3$ MeV and $k_0 = 1.8$, 2.5 and 3.0 for ^{234,236,238}U(n,γ) respectively, and keeping CGCM as LD. We can observe that the simulation with modified PSF reproduce better the trend of the experimental data than default PSF as expected because RIPL-3 does not introduce the SC mode in the definition of the $M1$ PSF which is responsible for the bump appearing in the middle of the MSC spectra.

Finally, we compare the results obtained from DICEBOX with the simulations of FIFRELIN using the same model and parameters for PSF and LD. Fig. 3.27 shows the results for the E_{sum} and MSC spectra obtained with both codes for ^{238}U(n,γ). We can observe little differences in the trend of the spectra but mostly we get the same results. Both codes reproduce the trend of the experimental data. To understand the source of these differences we study the parameters involved in the simulation of the cascade. Firstly, In Fig. 3.28 the influence of the internal conversion is shown. If the cascade is complete the sum of the gamma-ray energies has to be the Q value of the reaction that for the neutron energy used in this work corresponds to S_n ($\sim$ 4.8 MeV for ^{238}U(n,γ)). However, if there is an internal conversion the sum of the gamma-ray energies in the cascade will be lower than S_n because part of the energy is carried away by an electron. We can see that the influence of internal conversion estimated with DICEBOX and FIFRELIN is similar. Secondly, as explained in Sec. 1.3.2 the spin distribution is normalized by the integral of the distribution in the FIFRELIN simulation. However, the differences in the calculation of the D_0 are negligibe with $D_0 = 18.26$ eV for FIFRELIN with a normalized $f(E, J)$ and $D_0 = 18.28$ eV using directly $f(E, J)$ from eq. 1.2, so it is not the main source of the variations in the results. Finally, we study the nuclear level scheme used in FIFRELIN which is taken directly from RIPL-3 database and we note some differences compared to the one used in DICEBOX taken from ENSDF database. For instance, the nuclear levels with energies 0.098 MeV, 0.222 MeV, 0.226 MeV, 0.302 MeV, 0.307 MeV, 0.373 MeV, 0.499 MeV, 0.695 MeV, 0.702 MeV and 0.796 MeV below E_{crit} do not have transitions for the FIFRELIN level scheme and the branching intensities from these levels are simulated with PSF and LD models, while guess transitions are imposed in DICEBOX. It is important to mention that most of these levels have a spin higher than 7/2, so their feedings in the simulated cascade are negligible. In addition, FIFRELIN includes experimental levels at 0.020 MeV, 0.194 MeV,

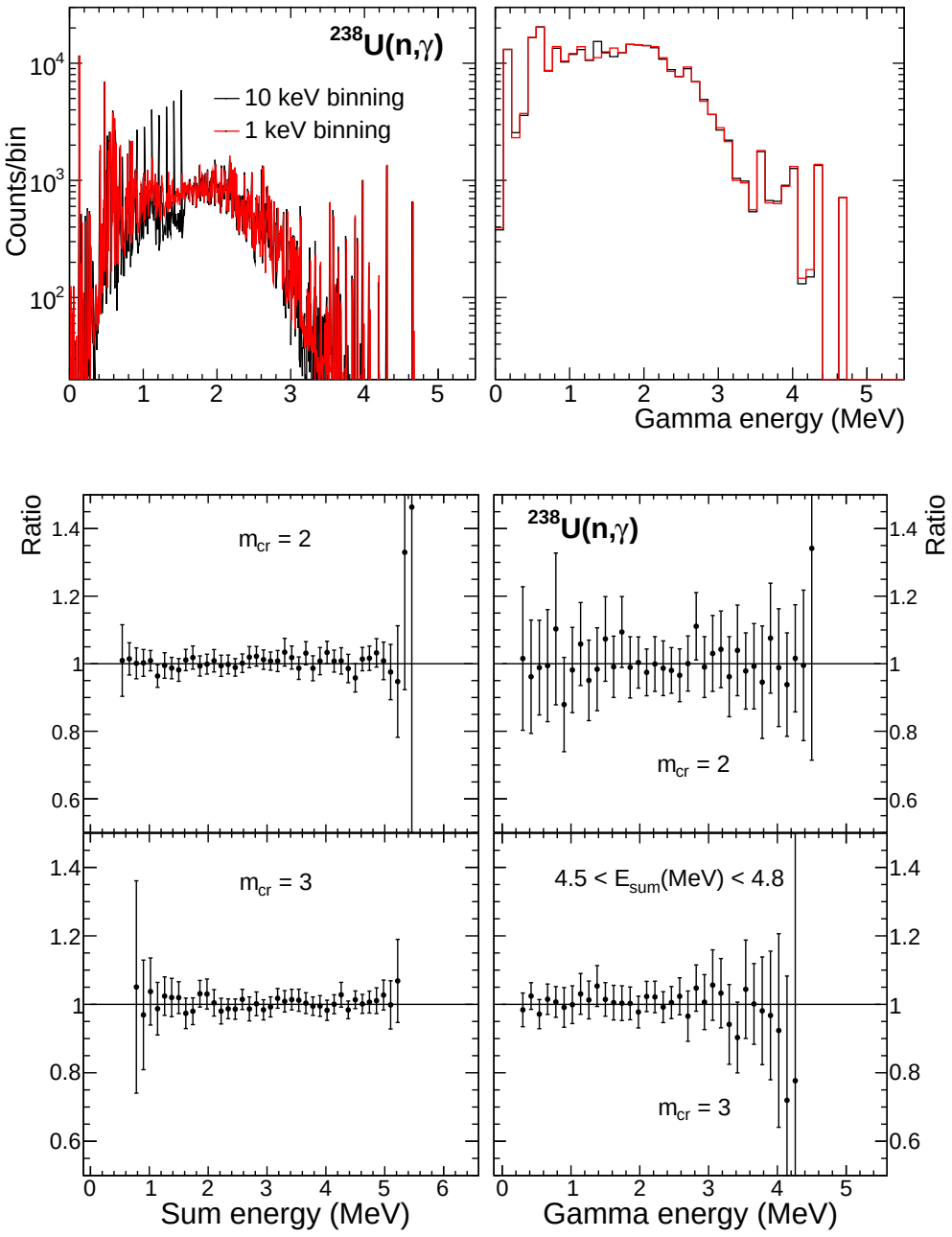

Figure 3.23: Single gamma spectrum for neutron capture events generated with FIFRELIN for a binning of 10 keV and 1 keV. The left spectra are plotted with $\sim$ 10 keV grid while right used $\sim$ 100 keV grid (top). Ratio between the simulations done with FIFRELIN for a binning of 10 keV and 1 keV for E_{sum} and MSC spectra (bottom).

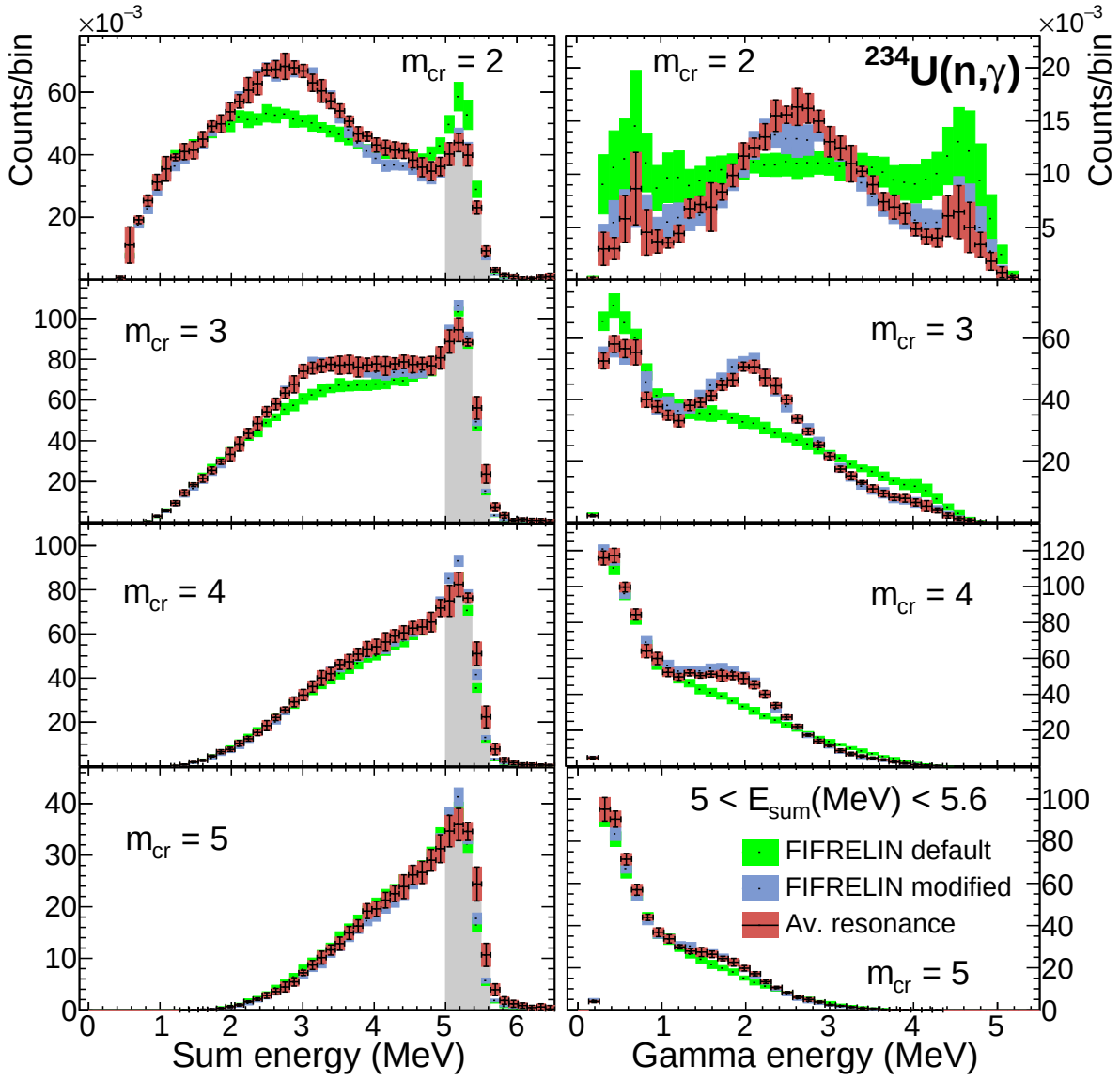

Figure 3.24: Comparison between a simulation using default parameters and models (PSF = EGLO and LD = CGCM) and a simulation using the modified parameters for the PSF collected in table 3.4 and MGLO with $k_0 = 1.8$ and $T = 0.3$ MeV in combination with CGCM for ^{234}U(n,γ). The crystal multiplicity and sum energy conditions are specified in the figures.

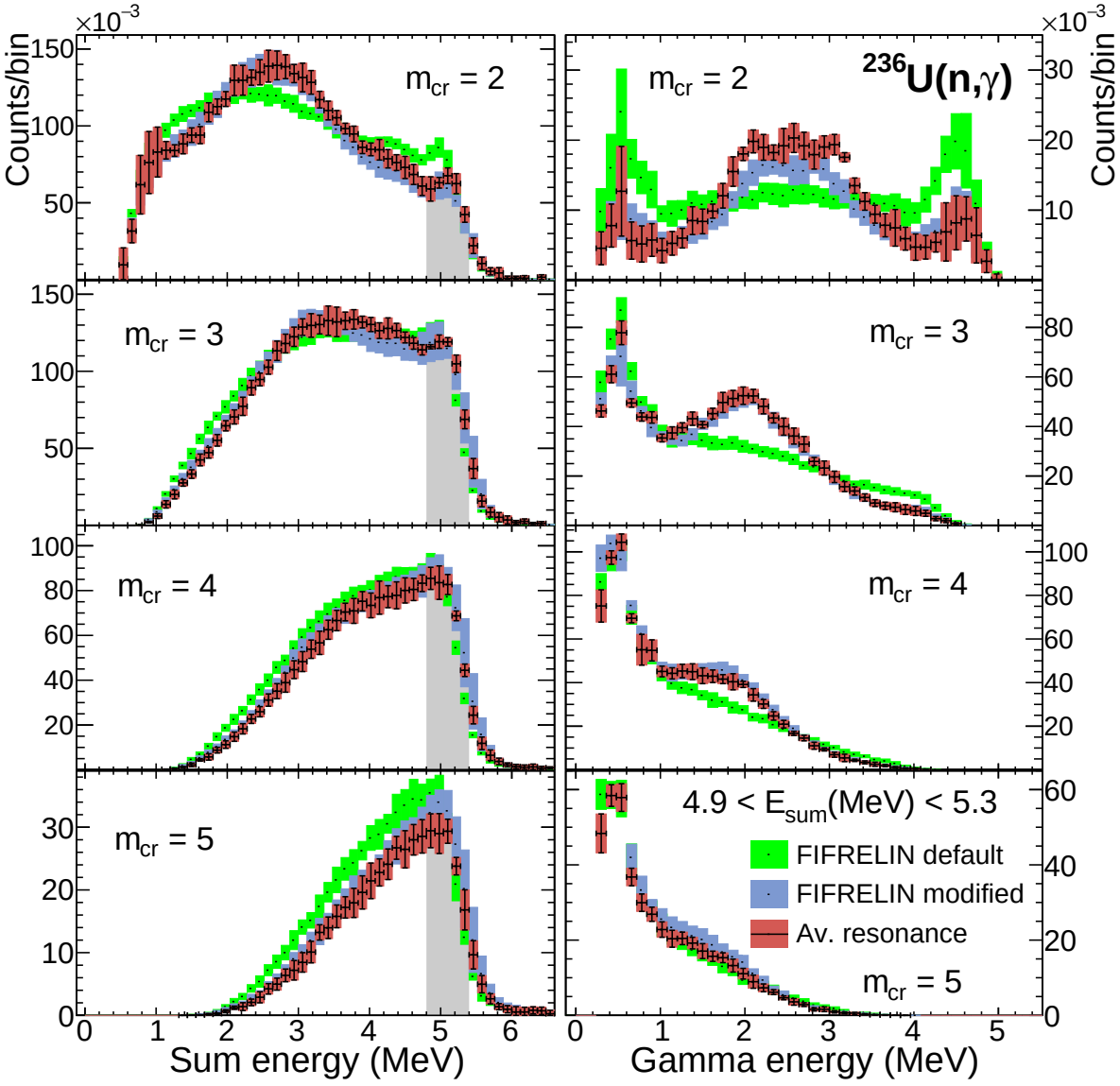

Figure 3.25: Same as Fig. 3.24 but using $k_0 = 2.5$ for ^{236}U(n,γ).

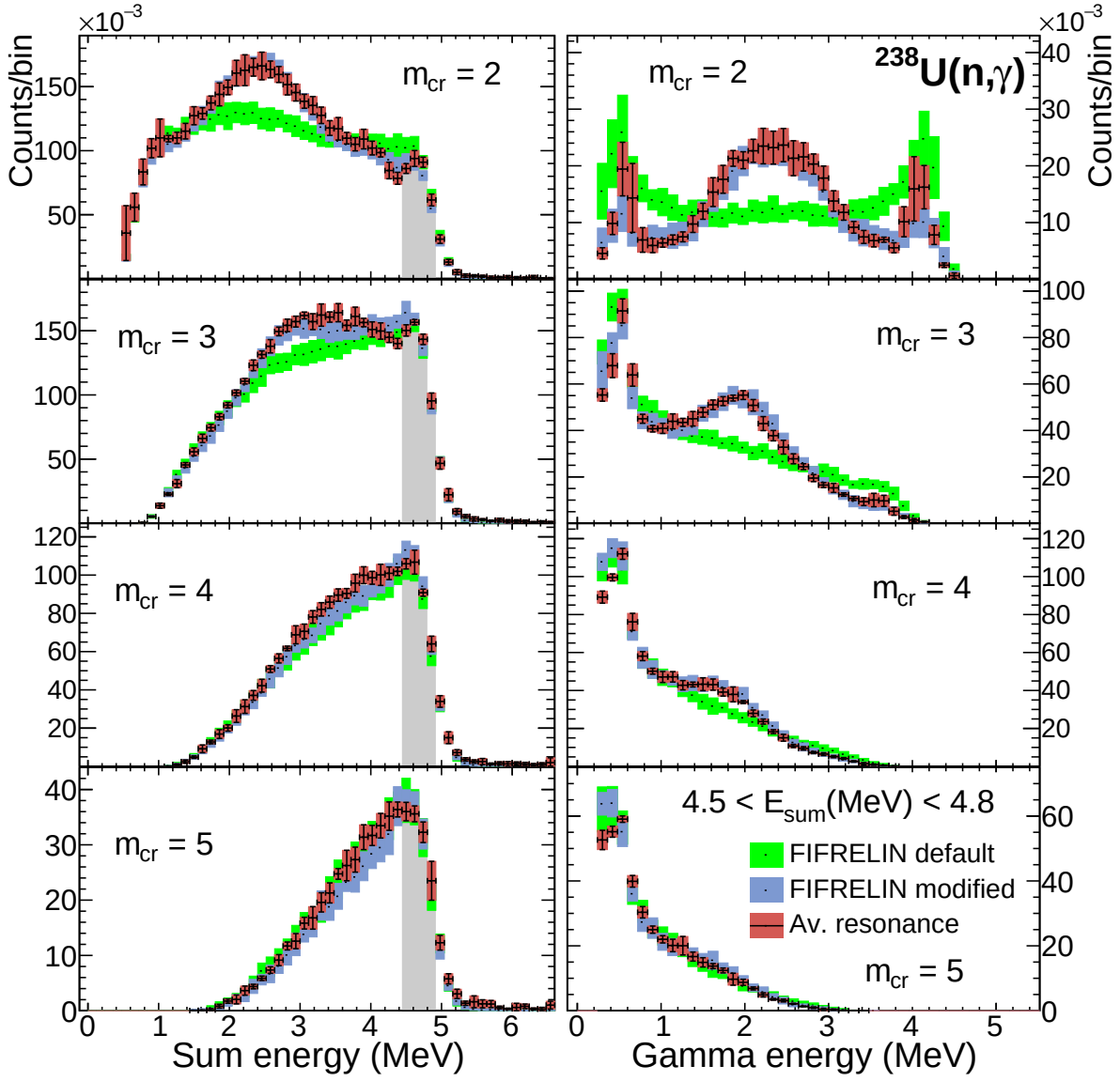

Figure 3.26: Same as Fig. 3.24 but using $k_0 = 3.0$ for ^{238}U(n,γ).

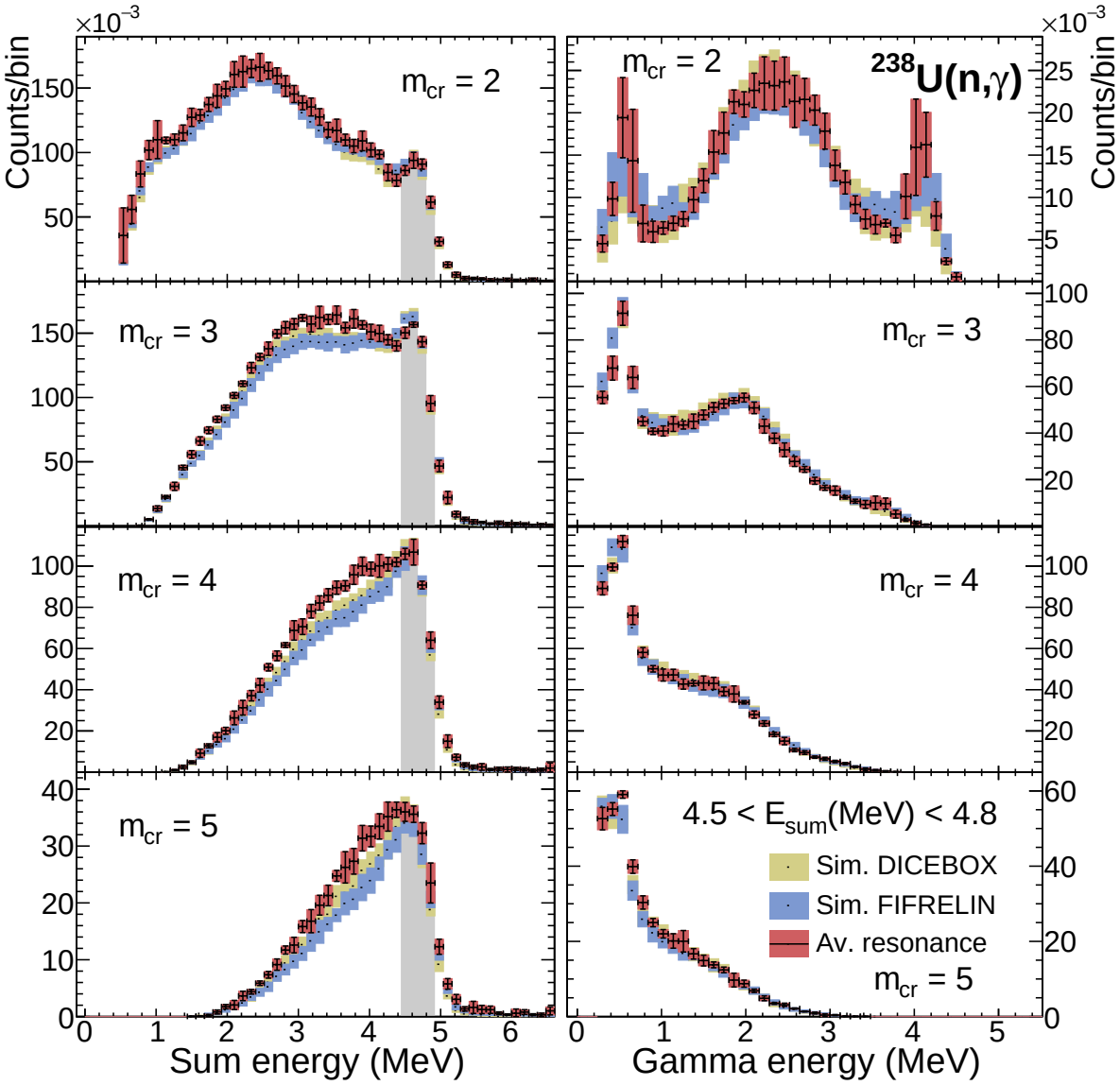

Figure 3.27: Comparison between simulations for ^{238}U(n,γ) with FIFRELIN and DICEBOX codes using MGLO with $k_0 = 3.0$ and CT VE09. The scheme of the experimental nuclear levels are taken from RIPL-3 for FIFRELIN and from ENSDF for DICEBOX.

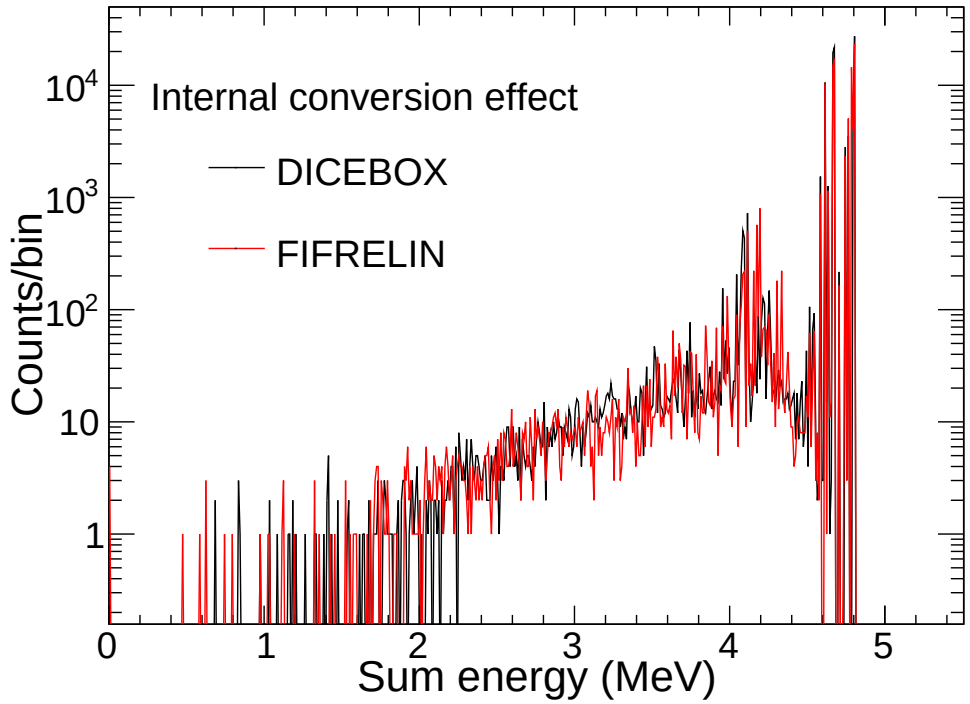

Figure 3.28: Comparison of the internal conversion effects for DICEBOX and FIFRELIN.

0.498 MeV and several other levels (around 70) above E_{crit}. Fig. 3.29 shows the feeding of the experimental nuclear levels when the initial level of the transition corresponds to other experimental level below E_{crit} considered in the simulation of the gamma cascades by FIFRELIN and DICEBOX whose values are collected in table 1.2 for each uranium isotope. We can observe some differences between both codes produced by nuclear levels considered from different nuclear databases as said before for ^{238}U(n,γ). For the case of ^{236}U(n,γ) we can apply the same logic, for instance the feeding of the three levels from FIFRELIN between 0.4 MeV and 0.6 MeV which do not appear for DICEBOX are produced from the level at 0.7180 MeV which is not considered in DICEBOX code. Finally, the simulations for ^{234}U(n,γ) present the most similar behaviour between the two codes because the description of the experimental nuclear levels is very similar. In addition, we compare the value of the TRW calculated by DICEBOX and FIFRELIN for the same PSF + LD simulation. The values of the TRW are collected in table 3.7. We can appreciate also little differences between both codes caused by the differences in the nuclear level scheme used.

We can conclude that both FIFRELIN and DICEBOX are satisfactory for simulating the γ-cascade, but the default use in FIFRELIN of the RIPL-3 database for the definition of the nuclear level scheme and PSF parameters are not favorable for a good agreement with the experimental data.

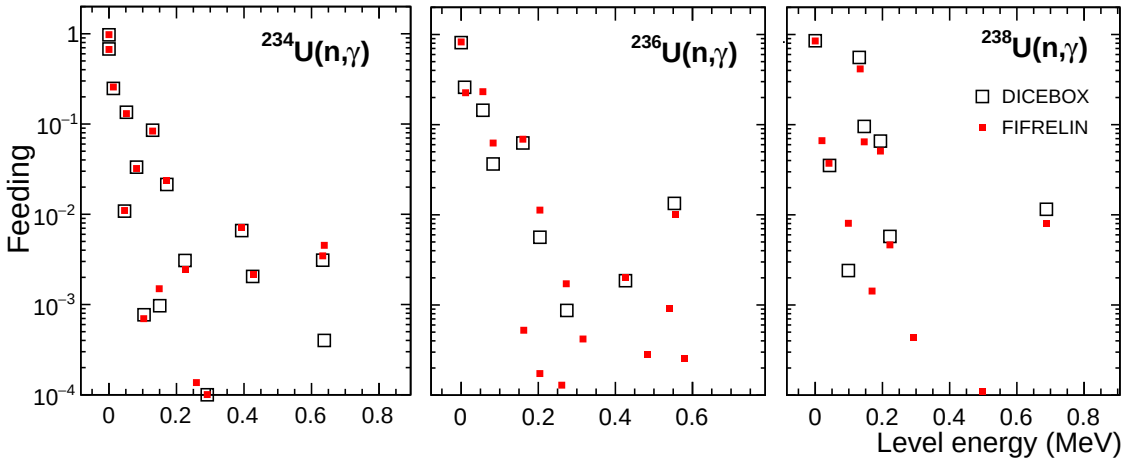

Figure 3.29: Feeding of the experimental levels from other experimental levels in the simulation of the gamma cascade for DICEBOX and FIFRELIN.

Table 3.7: Total radiation widths Γ_γ of s-wave resonances ($1/2^+$) obtained with same models of PSF and LD for DICEBOX and FIFRELIN.

	Γ_γ (meV)		
MC code	n + ^{234}U	n + ^{236}U	n + ^{238}U
DICEBOX	25.2(5)	23.4(7)	23.5(4)
FIFRELIN	24.6(1)	23.1(2)	23.7(1)

3.2.4 Sensitivity of the parameters

In this section we study the sensitivity of the PSF parameters to the TRW and the influence in the spectra. We only show the analysis for ^{238}U(n,γ) as a representative example. The combination used is MGLO with $k_0 = 3$ and T = 0.3 MeV as PSF, and CT VE09 as LD. However, similar results were obtained for the other isotopes regardless of the k_0 value.

Fig. 3.30 shows the behaviour of the TRW given by DICEBOX with respect to a $\Gamma_{\gamma,ref}$, that in this case is 23.5 meV, for changing in a maximum of $\pm$50% range the three parameters of the Lorentzians which define the PSF of the ^{238}U(n,γ) reaction. We can observe that the TRW increases its value very quickly for lower values of the E parameters while for higher values the TRW decreases more slowly. On the other hand, the TRW presents a similar behaviour for Γ and σ parameters increasing for higher values and decreasing for lower values of the parameters in a similar way. The trends of the TRW show a higher sensitivity to the E parameters while the Γ and σ parameters present a similar sensitivity although slightly less for σ. In addition, we study the slope of the curve in a range of 1% in which a linear fit can be made and results are collected in table 3.8. For both E and Γ parameters the most sensitive is the second Lorentzian of

the $E1$ PSF while for σ it is the first Lorentzian at 2.15 MeV which defines the SC mode of $M1$ PSF. In addition, the three parameters of the Lorentzian for SF mode and the second Lorentzian for SC mode present similar slope, so for $M1$ PSF the most sensitive parameters correspond to the first Lorentzian of the SC mode.

Table 3.8: Sensitivity coefficients of the TRW to the parameters of the PSF.

	$E1$ PSF			$M1$ PSF		
Isotope	$\frac{\partial\Gamma_\gamma}{\partial E}\cdot\frac{E_{ref}}{\Gamma_{\gamma,ref}}$	$\frac{\partial\Gamma_\gamma}{\partial\Gamma}\cdot\frac{\Gamma_{ref}}{\Gamma_{\gamma,ref}}$	$\frac{\partial\Gamma_\gamma}{\partial\sigma}\cdot\frac{\sigma_{ref}}{\Gamma_{\gamma,ref}}$	$\frac{\partial\Gamma_\gamma}{\partial E}\cdot\frac{E_{ref}}{\Gamma_{\gamma,ref}}$	$\frac{\partial\Gamma_\gamma}{\partial\Gamma}\cdot\frac{\Gamma_{ref}}{\Gamma_{\gamma,ref}}$	$\frac{\partial\Gamma_\gamma}{\partial\sigma}\cdot\frac{\sigma_{ref}}{\Gamma_{\gamma,ref}}$
^{234}U(n,γ)	-0.9(2)	0.33(9)	0.17(2)	-0.6(1)	0.21(4)	0.14(3)
	-1.3(2)	0.44(8)	0.22(4)	-0.8(2)	0.30(5)	0.37(6)
	–	–	–	-0.4(1)	0.12(2)	0.11(2)
^{236}U(n,γ)	-0.9(3)	0.33(9)	0.17(4)	-0.5(1)	0.19(7)	0.13(4)
	-1.4(4)	0.5(1)	0.25(6)	-0.8(3)	0.29(8)	0.36(9)
	–	–	–	-0.4(1)	0.11(3)	0.11(3)
^{238}U(n,γ)	-0.8(1)	0.28(4)	0.14(2)	-0.37(6)	0.19(3)	0.11(2)
	-1.3(3)	0.45(7)	0.22(4)	-0.9(2)	0.33(6)	0.38(7)
	–	–	–	-0.48(8)	0.14(2)	0.13(3)

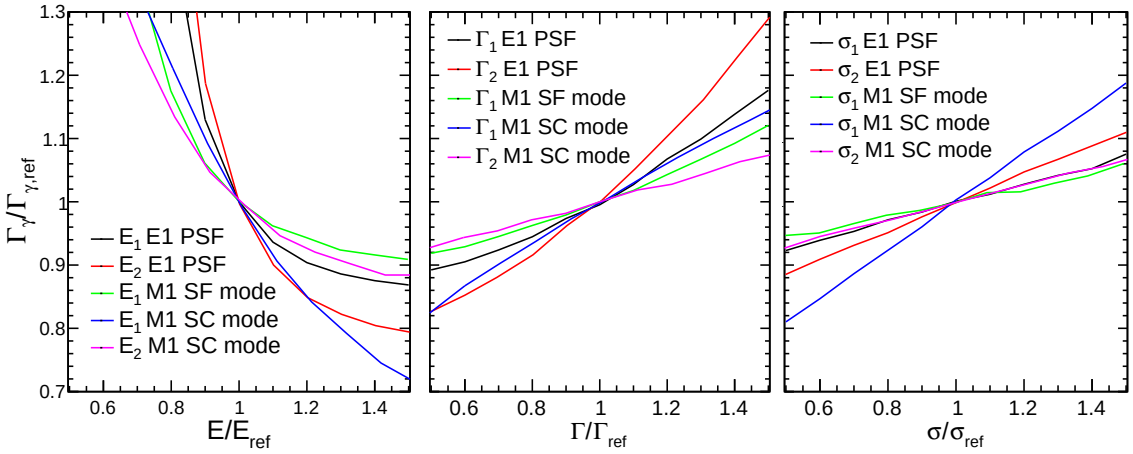

Figure 3.30: Behaviour of the TRW by changing the three parameters of the Lorentzians of the PSF in a range of ±50%. The reference values of the parameters are collected in table 3.4 for the MGLO model with $k_0 = 3$ and $T = 0.3$ MeV.

In this work we propose a study of the range of the parameters in which the results remain similar to the ones presented in previous sections by putting restriction in the coefficient of differences Δ^2_ν of the simulations. We consider the simulations presented before as references to compare with the simulation with changed parameters. If $\Delta^2_\nu > 0.40$ we suppose that the simulation present enough differences with respect to the original one to discard it. The limit value of Δ^2_ν was taken by comparison of a lot

of simulations with modified parameters. However, we always need the support of the spectra. To reduce the number of free parameters involved in the simulation we consider that the $E1$ PSF is fixed to experimental data at GEDR. We note that most of the parameters need large changes to affect the spectra, but when many parameters are modified in the same direction the impact on the spectra is greater. We neglect the correlations in this study and the ranges in the parameters may be overestimated. After a large number of simulations using different set of parameters we can estimate the range for each parameter of $M1$ PSF collected in table 3.9, in which the spectra do not change with respect to the reference ones and are in a good agreement with the experimental data. We observe that the peak positions of the SC mode present the lower ranges because these two parameters are highly sensitive at low crystal multiplicity. Fig. 3.31 shows the MSC spectra for ^{236}U(n,γ) where the values of the peak positions of the SC mode are modified from $E_1 = 2.15$ MeV to $E_1 = 2.00$ MeV and from $E_2 = 2.90$ MeV to $E_2 = 3.20$ MeV. We can observe important differences for $m_{cr} = 2$ which are negligible for higher crystal multiplicity. This means that the value of these two parameters can be extracted with a good accuracy.

Table 3.9: Ranges of the parameters for $M1$ PSF in which the TRW and the spectra are well simulated with respect to experimental data.

	Range for $M1$ PSF		
Isotope	E (MeV)	Γ (MeV)	σ (mb)
^{234}U(n,γ)	2.10 – 2.20	0.69 – 0.90	0.87 – 1.08
	2.85 – 2.95	0.50 – 0.83	0.62 – 1.02
	6.19 – 7.09	3.34 – 4.61	2.18 – 3.93
^{236}U(n,γ)	2.10 – 2.22	0.70 – 0.94	0.94 – 1.19
	2.80 – 3.00	0.50 – 0.90	0.80 – 1.43
	6.15 – 7.17	3.21 – 4.74	2.31 – 4.53
^{238}U(n,γ)	2.11 – 2.23	0.81 – 1.06	1.14 – 1.43
	2.80 – 3.10	0.59 – 1.12	0.80 – 1.61
	6.15 – 7.52	3.00 – 4.75	2.22 – 5.33

Finally, we are interested to study the sensitivy of the LD parameters because as seen in Sec. 3.2.2 the TRW varies notably with slight changes in the LD and in Sec. 1.1.6 the CT model does not exactly reproduce the evaluated D_0. In the same way as for the parameters of the PSF we study the behaviour of the D_0 with respect to the reference value $D_{0,ref}$ collected in table 1.1 for changing in a maximum of 15% range the parameters describing the CT model. We can observe in Fig. 3.32 where the behaviour of the $D_0/D_{0,ref}$ is shown for the relative difference of the parameters of the CT VE09 model that the most sensitive parameter to change the D_0 value is the T parameter while the lowest is the spin cut-off σ_c. In addition, the TRW presented considerable modifications overall for changes of the T parameter becuase the TRW is directly related with D_0.

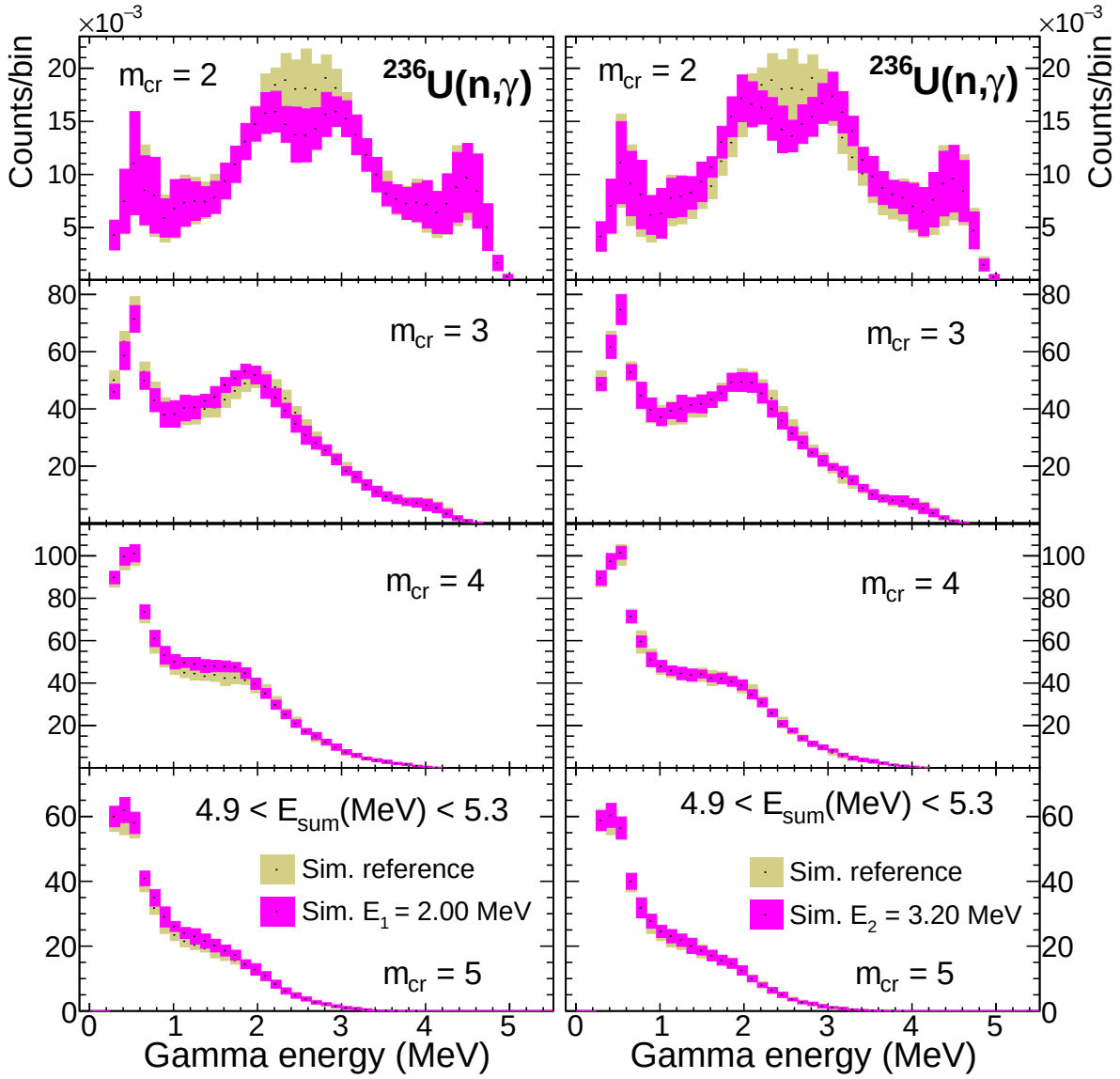

Figure 3.31: Impact on MSC spectra of changes of the peak position for the two Lorentzians of the SC mode. The reference simulation corresponds to that performed with $E_1 = 2.15$ MeV and $E_2 = 2.90$ MeV. Other parameters on table 3.4.

The spectra are also influenced for the parameters in the small range studied. We do not recommend to change the LD parameters more than ± 0.005 MeV for T, ± 0.05 MeV for E_0 and ± 0.5 for σ_c in order to keep similar results as presented before and a good value of D_0.

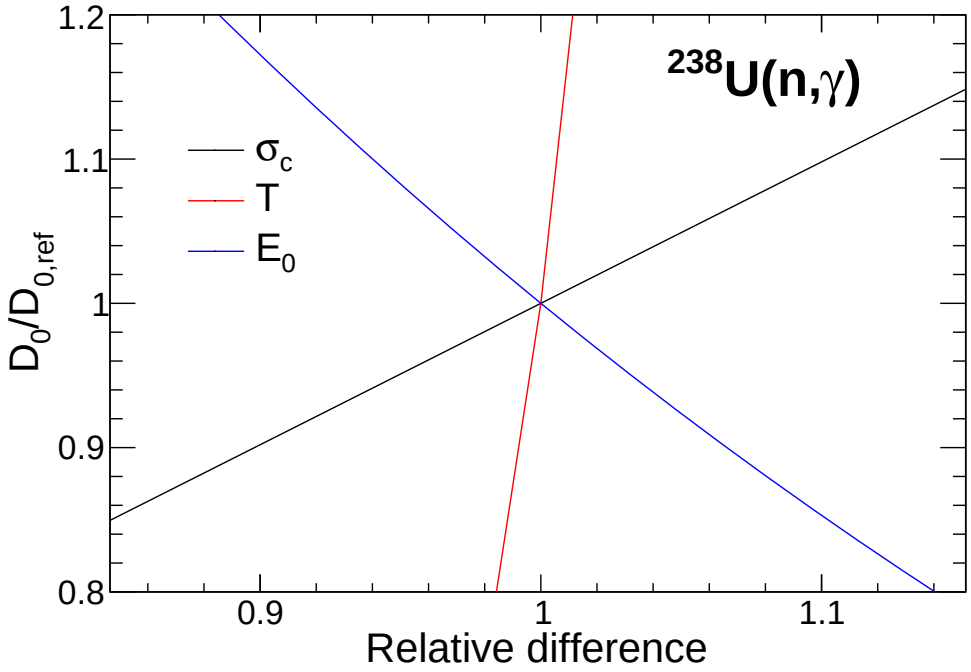

Figure 3.32: Behaviour of the D_0 by changing the parameters of the CT VE09 model in a range of 15%.

3.2.5 Relation between $E1$ and $M1$ PSFs.

In the previous subsections we have studied the necessity of modifying the k_0 parameter of the MGLO model in order to reproduce the TRW for each isotope of uranium for a given CT model. The $E1$ and $M1$ PSFs are shown in Fig. 3.33 (left) for the three combinations studied in this work by using $k_0 = 1.8$, 2.5 and 3. The error band of the $M1$ shows the sensitivity studied above and it means that inside the error band we can find a set of parameters for the $M1$ PSF which can reproduce the experimental spectra. We assign an isotope to each simulation to plot the error band. The increase in the $E1$ PSF produced by a higher k_0 seems to be related to the increase in the $M1$ PSF needed to reproduce the experimental data. Studying the ratio between the $M1$ and $E1$ PSFs shown in Fig. 3.33 (right) we observe that it remains similar when modifying k_0. The error band is given by the sensitivity of the calculated PSF. This means that for the MGLO model to define the $E1$ PSF we have to adjust the parameters of the $M1$ PSF to keep the same ratio $M1/E1$ regardless of the value of k_0 used in the range studied to reproduce all the experimental data.

To verify the validity of the ratio $M1/E1$ PSFs we use the MGLO model with an energy dependent temperature and k_0 showed before for each uranium isotopes, and adjusted parameters of the $M1$ PSF to reproduce the experimental data. The parameters are collected in table 3.4. We only focus on reproducing the E_{sum}, MSC and crystal multiplicity distribution spectra regardless of the TRW value obtained. The Δ_ν^2 of these three simulations for each observable are shown in Fig. 3.35 presenting similar results as in Sec. 3.2.2. However, the ratio $M1/E1$ needed to reproduce the experimental spectra, although it remains similar again for the different values of k_0, presents a different behaviour below ≈ 2.5 MeV with respect to MGLO using a constant temperature. This difference is produced because below ≈ 2.5 MeV the trends of both $E1$ PSFs are different as seen in Fig. 3.34 (left). Therefore, we can conclude that the ratio $M1/E1$ is different for different trends of the $E1$ PSF but remains unalterable for a similar behaviour under changes of the k_0 parameter.

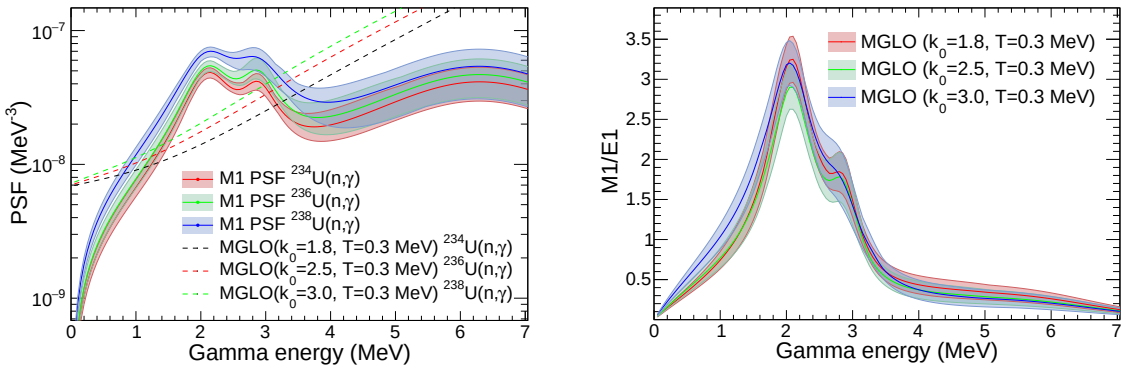

Figure 3.33: E1 (dashed line) and M1 (color band) PSFs models used in simulations for ^{234,236,238}U(n,γ) (left). Ratio between $M1$ and $E1$ PSFs (right).

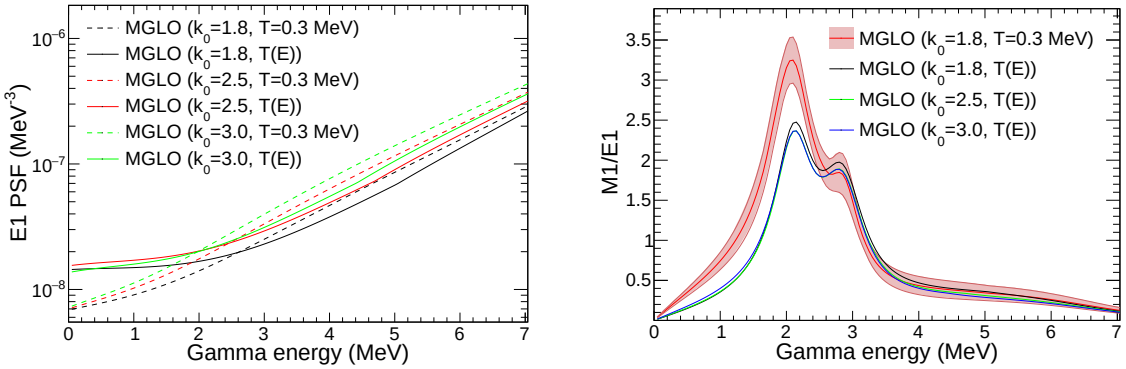

Figure 3.34: Comparison of $E1$ PSF for MGLO with $T = 0.3$ MeV and with energy dependent temperature for different values of the k_0 parameter (right). Comparison of the ratio between $M1$ and $E1$ PSFs for MGLO with a constant temperature and energy dependent temperature to reproduce the experimental spectra of the three uranium isotopes (left).

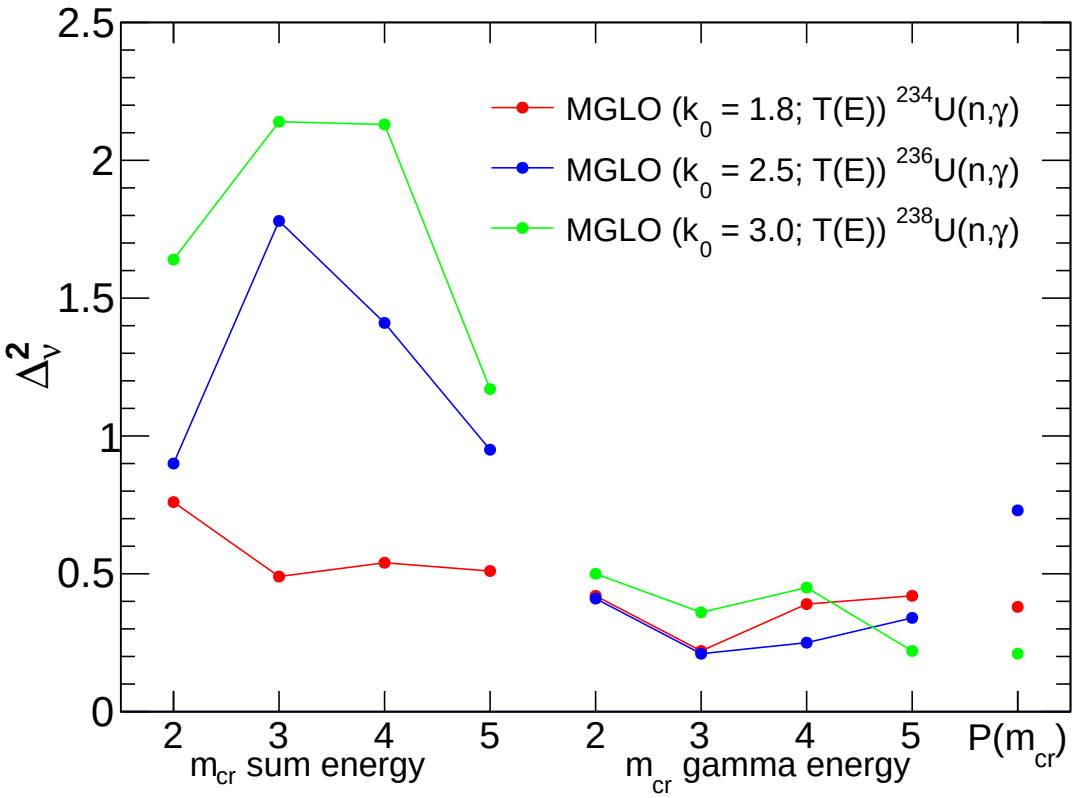

Figure 3.35: Δ^2_ν of the simulations using MGLO with energy dependent temperature for $k_0 = 1.8$ for ^{234}U(n,γ), $k_0 = 2.5$ for ^{236}U(n,γ) and $k_0 = 3.0$ for ^{238}U(n,γ) in combination with CT VE09. The lines are only plotted for a better visualization.

Conclusions

The gamma cascades following the neutron capture reactions on the isotopes ^{234}U, ^{236}U and ^{238}U were analysed with the aim to study and improve the PSF and LD in the framework of the statistical model for gamma decay. The total absorption calorimeter (TAC) at the n_TOF facility (CERN) was used for the detection of the gamma rays. With the information provided by the TAC we can access to the different observables used for the analysis: sum-energy spectra, multi-step cascade spectra, and crystal multiplicity distribution . Of all these observables the one that contains the most relevant information is the multi-step cascade spectra because it is directly related to the gamma decay with little sensitivity to the geometry of the experimental setup and to the resolution of the detectors.

GEANT4 simulations of the transport of gamma rays from the electromagnetic cascade modeled with DICEBOX for various level density (LD) and photon strength function combinations (PSF) were compared with the experimental data. The necessity of introducing a scissors mode (SC) contribution to $M1$ PSF was shown from model combinations and set of parameters in the literature. In particular, the DANCE analysis [7] showed an improvement in the behaviour of the simulation by modifying the parameters of the PSFs used in the OCL analysis [6]. In addition, we tested the validity of the tabulated values of the LD based on HFB plus combinatorial calculations and of the PSF from D1M+QRPA calculations with non-zero limit at low E_γ. We concluded that the simulations obtained with these semi-microscopic models for the LD and PSF, although they follow the trend of experimental data, should be improved further.

Following the results of these previous works we carried out an exhaustive analysis in order to improve the simulations of the gamma cascade for the three uranium isotopes studied in this work. We tested all possible PSF+LD combinations with the models presented in this work for different sets of parameters. The inadequacy of the SLO and KMF models of $E1$ PSF was shown focusing the analysis on the generalized models: ELO, GLO, EGLO, MGLO. We found some combinations which can agree with the experimental crystal multiplicity distribution, sum-energy and multi-step cascade spectra. In addition, through the use of a quantitative Δ_ν^2 parameter we noted that the ELO model produces better results in combination with BSFG for the LD while the other generalized models works better in combination with CT. We only show the case of MGLO because GLO and EGLO produce the same results when slightly changing the parameters. To reduce the number of possible combinations we use the total radiation width (TRW) as additional constraint. We found the necessity to use the MGLO model and the possibility to modify the value of k_0 in order to reproduce any reasonable TRW value for each isotope. For a good agreement with the TRW for simulations in

combination with CT VE09 we have to use a $k_0 = 3$ for ^{238}U(n,γ) which presented a stable TRW from the references. For ^{234}U(n,γ) a k_0 between 2.5 and 3 produces a good value of the TRW from ref. [109] while for the other references the TRW are reproduced by using a $k_0 = 1.8$. Finally, the TRW from JEFF-3.3 and ENDF/B-VIII.0 databases is reproduced by using a $k_0 = 1.8$ for ^{236}U(n,γ) but for refs. [108, 109] a $k_0 = 2.5$ is needed. However, although the k_0 value depends on the LD used in combination, the simulations present a good general agreement for $k_0 = 1.8$ for the three reactions.

On the other hand, we used the FIFRELIN code which was initialy dedicated to the simulation of the fission process with neutron emission. This work was usefull to test the validity of the simulations of the gamma decay made by FIFRELIN in the case of a neutron capture reaction on an actinide. We proved that the simulations using the default models and parameters for PSF and LD taken from the RIPL-3 database do not reproduce the trend of the experimental data. However, a good agreement is reached when the SC mode is included to describe the $M1$ PSF. In addition, we compare the FIFRELIN results with the simulation of DICEBOX which is a code used for many years in the simulation of the gamma decay. The results of both codes are similar. The only little difference is due to a different description of the experimental nuclear level scheme at low energy because FIFRELIN takes the levels from RIPL-3 database while DICEBOX take them from ENSDF. FIFRELIN should check its nuclear level scheme and not use the default parameters of the PSF in order to reproduce the experimental data.

We studied also the sensitivity of the TRW to the parameters of the Lorentzians of the PSF. Analyzing the trend of the TRW values we observed that the simulations are more sensitive to changes of the E parameters than the Γ and σ parameters. In addition, we observed that the first Lorentzian of the SC mode is more sensitive than the Lorentzian of the SF mode and the second Lorentzian of the SC mode. However, for E and Γ parameters the most sensitive was shown for the second Lorentzian of the $E1$ PSF. On the other hand, regarding the Δ^2_ν of different simulations we could determine the parameter ranges in which the results remain similar. The most sensitive parameters are the peak positions of the SC mode which means that these values are given with a good accuracy. Finally, we noted a large sensitivity of the TRW to the LD even for very similar formulas and parameters. In order to reproduce the same results that were shown in this work the LD parameter ranges are $\pm$ 0.005 MeV for T and $\pm$ 0.05 MeV for E_0 of the CT formula.

To establish a relationship between all the results, we studied the ratio between $M1$ and $E1$ PSFs. We found that for the MGLO model of $E1$ PSF with different values of k_0 we have to keep a similar ratio $M1/E1$ to reproduce the experimental data, but if the trend of the $E1$ model is very different the ratio $M1/E1$ will be also different.

In summary, the results presented in this work confirm the need to use the SC mode for $M1$ PSF to reproduce the experimental data. However, the intensity of the PSFs may be different for each isotope to reproduce different values of the TRW and they are also directly related with the LD used in combination. In addition, we study the sensitivity of the parameters and get a range of values in which the simulations give similar results. Finally, we show the importance of the ratio between $M1$ and $E1$ PSFs for similar trends of the models which should be kept in order to reproduce the experimental data and which remains unchanged by modification of the k_0 parameter.

Appendix A

Table A1: Energy E_r, spin and parityJ^π, neutron width Γ_n, gamma witdh Γ_γ, fission width Γ_f and count rate of the time window used for the analysis of the resonances for the systems n + ^{234,236,238}U. The values are taken from the JEFF-3.3 database [110, 111].

n + ^{234}U					
E_r (eV)	J^π	Γ_n (eV)	Γ_γ (eV)	Γ_f (eV)	Counts/μs
5.16	$1/2^+$	0.0039	0.030	1.8e-5	0.17
31.13	$1/2^+$	0.0072	0.026	8.6e-6	0.27
48.56	$1/2^+$	0.0087	0.026	0	0.30
77.38	$1/2^+$	0.0103	0.026	4.4e-6	0.22
94.29	$1/2^+$	0.0417	0.026	3.35e-5	0.30
111.06	$1/2^+$	0.0185	0.026	3.08e-4	0.25
146.25	$1/2^+$	0.0134	0.026	2.88e-5	0.14
152.16	$1/2^+$	0.0179	0.026	2.16e-5	0.16

n + ^{236}U					
$E_r(eV)$	J^π	Γ_n (eV)	Γ_γ (eV)	Γ_f (eV)	Counts/μs
5.45	$1/2^+$	0.0022	0.0245	2.9e-4	0.19
29.8	$1/2^+$	5.85e-4	0.023	1.6e-4	0.20
34.1	$1/2^+$	0.0024	0.0209	1.8e-4	0.20
43.91	$1/2^+$	0.0175	0.0192	4.3e-4	0.17
71.47	$1/2^+$	0.024	0.022	2.9e-4	0.14
86.51	$1/2^+$	0.036	0.020	3.0e-4	0.14
124.88	$1/2^+$	0.017	0.019	2.1e-4	0.16

n + ^{238}U					
$E_r(eV)$	J^π	Γ_n (eV)	Γ_γ (eV)	Γ_f (eV)	Counts/μs
6.67	$1/2^+$	0.0015	0.0227	0	0.11
20.87	$1/2^+$	0.0101	0.0228	5.46e-8	0.08
36.68	$1/2^+$	0.0336	0.0223	0	0.10
66.03	$1/2^+$	0.0243	0.0224	5.19e-8	0.15
102.56	$1/2^+$	0.0709	0.0232	0	0.13
116.90	$1/2^+$	0.0253	0.0214	0	0.10

Appendix B

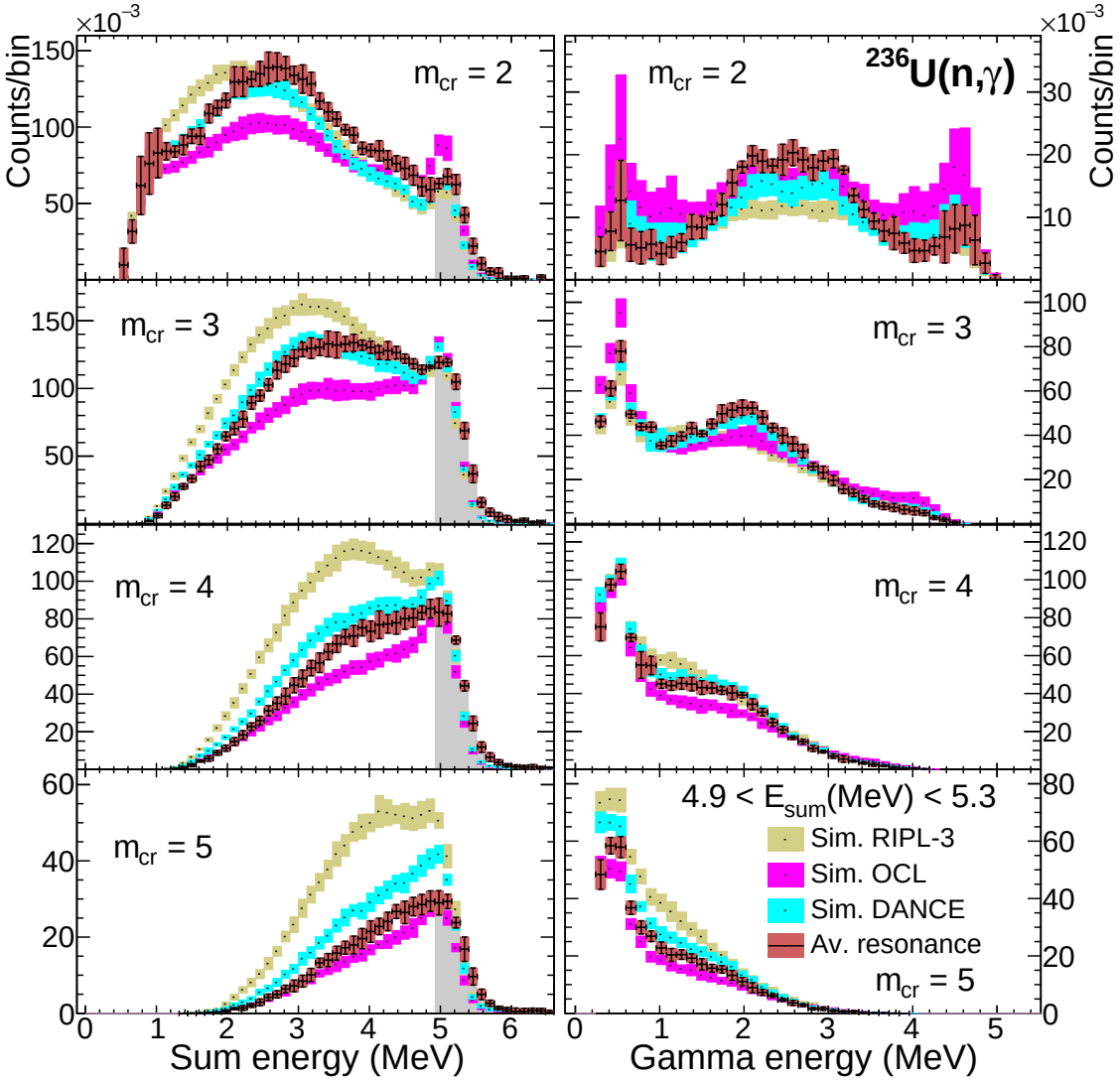

Figure B1: Comparison of the MSC spectra for ^{236}U(n, γ) reactions with simulations using the LD and PSF models as recommended in RIPL-3 database [21] (mustard), and as published in OCL [6] (pink) and DANCE [7] (blue). The crystal multiplicity and sum energy conditions are specified in the figures.

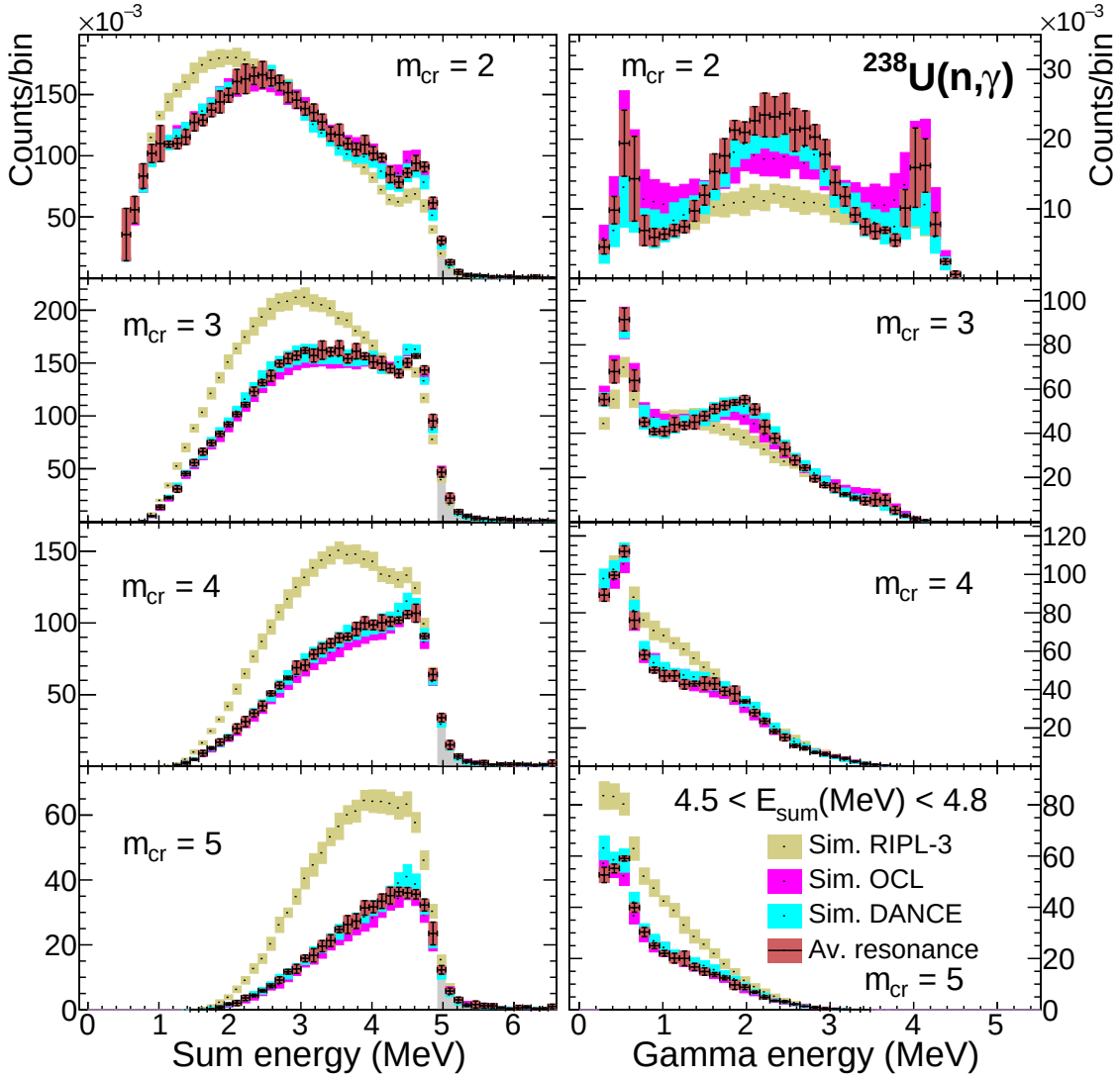

Figure B2: Comparison of the MSC spectra for ^{238}U(n, γ) reactions with simulations using the LD and PSF models as recommended in RIPL-3 database [21] (mustard), and as published in OCL [6] (pink) and DANCE [7] (blue). The multiplicity and sum energy conditions are specified in the figures.

Appendix C

Table C1: Levels from ENSDF for ^{235}U used for describing the region below a certain critical excitation energy E_{crit} of 0.820 MeV in the simulation of the gamma cascades by DICEBOX.

E_{level} (keV)	J^π	E_{level} (keV)	J^π	E_{level} (keV)	J^π
0.000	$7/2^-$	368.900	$13/2^+$	670.924	$7/2^-$
0.076	$1/2^+$	393.218	$3/2^+$	671.940	$23/2^-$
13.034	$3/2^+$	414.768	$9/2^+$	701.101	$7/2^-$
46.103	$9/2^-$	426.741	$5/2^+$	703.753	$3/2^-$
51.697	$5/2^+$	439.390	$19/2^-$	710.020	$21/2^+$
81.724	$7/2^+$	445.648	$7/2^+$	720.220	$9/2^-$
103.903	$11/2^-$	456.840	$15/2^+$	750.210	$9/2^-$
129.2995	$5/2^+$	473.826	$7/2^+$	761.017	$1/2^-$
150.356	$9/2^+$	482.000	$17/2^+$	769.270	$1/2^+$
171.358	$7/2^+$	510.490	$9/2^+$	769.934	$3/2^-$
171.464	$13/2^+$	533.208	$9/2^+$	778.360	$11/2^-$
197.087	$11/2^+$	551.170	$21/2^-$	779.510	$3/2^+$
225.382	$9/2^+$	557.200	$17/2^+$	787.800	$21/2^+$
250.014	$15/2^-$	559.340	$19/2^+$	790.900	$15/2^+$
291.135	$11/2^+$	608.170	$11/2^+$	800.580	$23/2^+$
294.557	$13/2^+$	633.092	$5/2^-$	805.650	$25/2^-$
332.845	$5/2^+$	637.794	$3/2^-$	805.651	$3/2^-$
339.976	$17/2^-$	658.960	$1/2^-$	806.900	$11/2^-$
357.220	$15/2^+$	664.531	$5/2^-$	811.960	$5/2^-$
367.031	$7/2^+$	666.690	$19/2^+$		

Table C2: Levels from ENSDF for ^{237}U used for describing the region below a certain critical excitation energy E_{crit} of 0.760 MeV in the simulation of the gamma cascades by DICEBOX.

E_{level} (keV)	J^π	E_{level} (keV)	J^π
0.000	$1/2^+$	506.000	$15/2^-$
11.390	$3/2^+$	518.000	$17/2^+$
56.300	$5/2^+$	540.620	$1/2^-$
82.860	$7/2^+$	551.000	$11/2^+$
159.960	$5/2^+$	554.980	$3/2^-$
163.000	$9/2^+$	578.010	$5/2^-$
204.190	$7/2^+$	592.000	$17/2^-$
205.000	$11/2^+$	607.700	$17/2^+$
260.950	$9/2^+$	632.000	$13/2^+$
274.000	$7/2^-$	664.270	$3/2^+$
316.000	$9/2^-$	666.450	$5/2^+$
317.300	$13/2^+$	677.590	$5/2^+$
327.000	$11/2^+$	690.000	$19/2^-$
367.000	$11/2^-$	697.650	$19/2^+$
375.100	$15/2^+$	608.170	$5/2^+$
409.800	$13/2^+$	720.450	$3/2^-$
426.150	$7/2^+$	721.500	$19/2^+$
432.000	$13/2^-$	734.340	$1/2^-$
482.000	$9/2^+$	758.160	$3/2^-$
501.400	$15/2^+$		

Table C3: Levels from ENSDF for ^{239}U used for describing the region below a certain critical excitation energy E_{crit} of 0.830 MeV in the simulation of the gamma cascades by DICEBOX.

E_{level} (keV)	J^π	E_{level} (keV)	J^π
0.000	$5/2^+$	734.650	$5/2^+$
42.543	$7/2^+$	739.381	$1/2^-$
98.630	$9/2^+$	746.057	$3/2^-$
133.799	$1/2^+$	757.150	$5/2^+$
145.769	$3/2^+$	784.275	$5/2^-$
169.089	$7/2^+$	795.900	$7/2^-$
193.987	$5/2^+$	815.181	$1/2^-$
222.240	$7/2^+$	823.718	$3/2^-$
226.300	$9/2^+$		
292.587	$7/2^-$		
301.800	$11/2^+$		
307.800	$9/2^+$		
372.700	$11/2^-$		
498.600	$15/2^-$		
539.290	$5/2^-$		
687.854	$1/2^+$		
694.700	$5/2^+$		
702.500	$9/2^+$		
715.834	$3/2^+$		
726.122	$3/2^+$		

Bibliography

[1] G A Bartholomew. Neutron capture gamma rays. *Ann. Rev. Nucl. Sci.*, 11(1):259–302, 1961. doi:10.1146/annurev.ns.11.120161.001355.

[2] D. M. Brink. *Some aspect of the interaction of fields with matter*. PhD thesis, Oxford University, 1955.

[3] N. Lo Iudice and F. Palumbo. New isovector collective modes in deformed nuclei. *Phys. Rev. Lett.*, 41:1532–1534, Nov 1978. doi:10.1103/PhysRevLett.41.1532.

[4] F. Iachello. Electron scattering in the interacting boson model. *Nucl. Phys. A*, 358:89 – 112, 1981. doi:https://doi.org/10.1016/0375-9474(81)90308-0.

[5] U. Kneissl, H.H. Pitz, and A. Zilges. Investigation of nuclear structure by resonance fluorescence scattering. *Prog. Part. Nucl. Phys.*, 37:349 – 433, 1996. doi:https://doi.org/10.1016/0146-6410(96)00055-5.

[6] M. Guttormsen, L. A. Bernstein, A. Görgen, et al. Scissors resonance in the quasicontinuum of th, pa, and u isotopes. *Phys. Rev. C*, 89:014302, Jan 2014. doi:10.1103/PhysRevC.89.014302.

[7] J. L. Ullmann, T. Kawano, B. Baramsai, et al. Constraining the calculation of ^{234,236,238}U(n,γ) cross sections with measurements of the γ-ray spectra at the dance facility. *Phys. Rev. C*, 96:024627, Aug 2017. doi:10.1103/PhysRevC.96.024627.

[8] C. Guerrero et al. Study of Photon Strength Function of Actinides: the Case of 235U, 238Np and 241Pu. *J. Korean Phy. Soc.*, 59(2):1510, 2011. URL: https://doi.org/10.3938/jkps.59.1510.

[9] G. J. Mathews and R. A. Ward. Neutron capture process in astrophysics. *Rep. Prog. Phys.*, 48(10):1371–1418, oct 1985. doi:10.1088/0034-4885/48/10/002.

[10] C. Sneden, J. J. Cowan, and R. Gallino. Neutron-capture elements in the early galaxy. *Annu. Rev. Astron. Astrophys.*, 46(1):241–288, 2008. doi:10.1146/annurev.astro.46.060407.145207.

[11] Report of the nuclear physics and related computational science R&D for advanced fuel cycles workshop, august 10-12, 2006, bethesda, maryland. 8 2006.

[12] H. A. Bethe. An attempt to calculate the number of energy levels of a heavy nucleus. *Phys. Rev.*, 50:332–341, Aug 1936. doi:10.1103/PhysRev.50.332.

[13] A. Gilbert and A. G. W. Cameron. A composite nuclear-level density formula with shell corrections. *Can. J. of Phys.*, 43(8):1446–1496, 1965. doi:10.1139/p65-139.

[14] T. von Egidy, H.H. Schmidt, and A.N. Behkami. Nuclear level densities and level spacing distributions: Part ii. *Nucl. Phys. A*, 481(2):189 – 206, 1988. doi:https://doi.org/10.1016/0375-9474(88)90491-5.

[15] T. von Egidy and D. Bucurescu. Systematics of nuclear level density parameters. *Phys. Rev. C*, 72:044311, Oct 2005. doi:10.1103/PhysRevC.72.044311.

[16] T. von Egidy and D. Bucurescu. Experimental energy-dependent nuclear spin distributions. *Phys. Rev. C*, 80:054310, Nov 2009. doi:10.1103/PhysRevC.80.054310.

[17] G. Audi, A.H. Wapstra, and C. Thibault. The ame2003 atomic mass evaluation: (ii). tables, graphs and references. *Nucl. Phys. A*, 729(1):337 – 676, 2003. The 2003 NUBASE and Atomic Mass Evaluations. doi:https://doi.org/10.1016/j.nuclphysa.2003.11.003.

[18] N. Rosenzweig. Influence of shell structure on the level density of a highly excited nucleus. *Phys. Rev.*, 108:817–826, Nov 1957. doi:10.1103/PhysRev.108.817.

[19] S. Goriely. A new nuclear level density formula including shell and pairing correction in the light of a microscopic model calculation. *Nucl. Phys. A*, 605(1):28 – 60, 1996. doi:https://doi.org/10.1016/0375-9474(96)00162-5.

[20] A V Ignatyuk, G N Smirenkin, and A S Tishin. Phenomenological description of energy dependence of the level density parameter. *Yad. Fiz.*, 21(3):485–490, 3 1975.

[21] R. Capote et al. RIPL – reference input parameter library for calculation of nuclear reactions and nuclear data evaluations. *Nucl. Data Sheets*, 110(12):3107 – 3214, 2009. Special Issue on Nuclear Reaction Data. doi:https://doi.org/10.1016/j.nds.2009.10.004.

[22] S. Hilaire, J.P. Delaroche, and A.J. Koning. Generalized particle-hole state densities within the equidistant spacing model. *Nucl. Phys. A*, 632(3):417 – 441, 1998. doi:https://doi.org/10.1016/S0375-9474(98)00003-7.

[23] S. Hilaire and S. Goriely. Global microscopic nuclear level densities within the HFB plus combinatorial method for practical applications. *Nucl. Phys. A*, 779:63 – 81, 2006. doi:https://doi.org/10.1016/j.nuclphysa.2006.08.014.

[24] S. Goriely, S. Hilaire, and A. J. Koning. Improved microscopic nuclear level densities within the hartree-fock-bogoliubov plus combinatorial method. *Phys. Rev. C*, 78:064307, Dec 2008. doi:10.1103/PhysRevC.78.064307.

[25] A Koning, S Hilaire, and S Goriely. Talys-1.9 a nuclear reaction program, user manual. *NRG, Netherlands*, pages 112–113, Dec 2017.

[26] [online]URL: https://www-nds.iaea.org/RIPL-3/.

[27] A.G. Bohr and B.R. Mottelson. *Nuclear Structure*, volume I. W. A., 1969.

[28] M. Krtičcka. *Photon Strength Function in Rare-Earth Nuclei Studied From Slow Neutron Capture*. PhD thesis, Charles University in Prague, 2002.

[29] G. C. Baldwin and G. S. Klaiber. Photo-fission in heavy elements. *Phys. Rev.*, 71:3–10, Jan 1947. doi:10.1103/PhysRev.71.3.

[30] H. Steinwedel and J. Jensen. Hydrodynamik von kerndipolschwingungen. *Z. Naturforsch*, 5A, 08 1950. doi:10.1515/zna-1950-0801.

[31] M. Goldhaber and E. Teller. On nuclear dipole vibrations. *Phys. Rev.*, 74:1046–1049, Nov 1948. doi:10.1103/PhysRev.74.1046.

[32] B. L. Berman and S. C. Fultz. Measurements of the giant dipole resonance with monoenergetic photons. *Rev. Mod. Phys.*, 47:713–761, Jul 1975. doi:10.1103/RevModPhys.47.713.

[33] M N Harakeh and A van der Woude. *Giant Resonances Fundamental High-Frequency Modes of Nuclear Excitation*. Oxford University Press, 2001.

[34] S. S. Dietrich and B. L. Berman. Atlas of photoneutron cross sections obtained with monoenergetic photons. *Atomic Data and Nuclear Data Tables*, 38(2):199 – 338, 1988. doi:https://doi.org/10.1016/0092-640X(88)90033-2.

[35] P. Axel. Electric dipole ground-state transition width strength function and 7-mev photon interactions. *Phys. Rev.*, 126:671–683, Apr 1962. doi:10.1103/PhysRev.126.671.

[36] C. M. McCullagh, M. L. Stelts, and R. E. Chrien. Dipole radiative strength functions from resonance neutron capture. *Phys. Rev. C*, 23:1394–1403, Apr 1981. doi:10.1103/PhysRevC.23.1394.

[37] G Baym and C Pethick. *Landau Fermi-Liquid Theory and Low Temperature Properties of Normal Liquid 3He*, chapter 1, pages 1–121. John Wiley & Sons, Ltd, 2007. doi:10.1002/9783527617159.ch1.

[38] S. G. Kadmenskii, V. P. Markushev, and V. I. Furman. *Sov. J. Nucl. Phys.*, 37:165, 1983.

[39] L. Zanini, F. Corvi, et al. Cascade γ decay study of ^{108}Ag following thermal and resonance neutron capture in ^{107}Ag. *Phys. Rev. C*, 68:014320, Jul 2003. doi:10.1103/PhysRevC.68.014320.

[40] J. Kopecky and M. Uhl. Test of gamma-ray strength functions in nuclear reaction model calculations. *Phys. Rev. C*, 41:1941–1955, May 1990. doi:10.1103/PhysRevC.41.1941.

[41] J. Kopecky and R.E. Chrien. Observation of the $M1$ giant resonance by resonance averaging in 106pd. *Nucl. Phys. A*, 468(2):285 – 300, 1987. doi:https://doi.org/10.1016/0375-9474(87)90518-5.

[42] V.A. Plujko, O.M. Gorbachenko, E.P. Rovenskykh, and V.A. Zheltonozhskii. Average description of dipole gamma transitions in hot atomic nuclei. *Nucl. Data Sheets*, 118:237 – 239, 2014. doi:https://doi.org/10.1016/j.nds.2014.04.046.

[43] S.F. Mughabghab and C.L. Dunford. A dipole–quadrupole interaction term in $E1$ photon transitions. *Phys. Lett. B*, 487(1):155 – 164, 2000. doi:https://doi.org/10.1016/S0370-2693(00)00792-9.

[44] S. Goriely. Radiative neutron captures by neutron-rich nuclei and the r-process nucleosynthesis. *Phys. Lett. B*, 436(1):10 – 18, 1998. doi:https://doi.org/10.1016/S0370-2693(98)00907-1.

[45] J. Kopecky, M. Uhl, and R. E. Chrien. Radiative strength in the compound nucleus ^{157}Gd. *Phys. Rev. C*, 47:312–322, Jan 1993. doi:10.1103/PhysRevC.47.312.

[46] *Handbook for Calculations of Nuclear Reaction Data*, volume IAEA-TECDOC-1034. IAEA, Vienna, 1998. URL: https://www.iaea.org/publications/7129/handbook-for-calculations-of-nuclear-reaction-data-ripl-2.

[47] J. Kroll, B. Baramsai, G. E. Mitchell, et al. Strength of the scissors mode in odd-mass gd isotopes from the radiative capture of resonance neutrons. *Phys. Rev. C*, 88:034317, Sep 2013. doi:10.1103/PhysRevC.88.034317.

[48] C. S. Shapiro and G. T. Emery. Magnetic dipole gamma-ray strength function in deformed nuclei, and neutron-capture gamma rays. *Phys. Rev. Lett.*, 23:244–246, Aug 1969. doi:10.1103/PhysRevLett.23.244.

[49] L. M. Bollinger and G. E. Thomas. Average-resonance method of neutron-capture

γ-ray spectroscopy: States of ^{106}Pd, ^{156}Gd, ^{158}Gd, ^{166}Ho, and ^{168}Er. *Phys. Rev. C*, 2:1951–2000, Nov 1970. doi:10.1103/PhysRevC.2.1951.

[50] J. Kopecky, S. Goriely, S. Péru, S. Hilaire, and M. Martini. $E1$ and $M1$ strength functions from average resonance capture data. *Phys. Rev. C*, 95:054317, May 2017. doi:10.1103/PhysRevC.95.054317.

[51] D. Frekers, H.J. Wörtche, A. Richter, R. Abegg, et al. Spin excitations in the deformed nuclei 154sm, 158gd and 168er. *Phys. Lett. B*, 244(2):178 – 182, 1990. doi:https://doi.org/10.1016/0370-2693(90)90051-7.

[52] A. Richter. Probing the nuclear magnetic dipole response with electrons, photons and hadrons. *Prog. Part. Nucl. Phys.*, 34:261 – 284, 1995. Electromagnetic Probes and the Structure Hadrons and Nuclei. doi:https://doi.org/10.1016/0146-6410(95)00022-B.

[53] D. Bohle, A. Richter, W. Steffen, A.E.L. Dieperink, et al. New magnetic dipole excitation mode studied in the heavy deformed nucleus 156gd by inelastic electron scattering. *Phys. Lett. B*, 137(1):27 – 31, 1984. doi:https://doi.org/10.1016/0370-2693(84)91099-2.

[54] D. Bohle, G. Küchler, A. Richter, and W. Steffen. Further evidence for the new collective magnetic dipole mode in heavy deformed nuclei. *Phys. Lett. B*, 148(4):260 – 264, 1984. doi:https://doi.org/10.1016/0370-2693(84)90084-4.

[55] S. L. Hammond, A. S. Adekola, C. T. Angell, et al. Dipole response of ^{238}u to polarized photons below the neutron separation energy. *Phys. Rev. C*, 85:044302, Apr 2012. doi:10.1103/PhysRevC.85.044302.

[56] J. Margraf, A. Degener, H. Friedrichs, et al. Photoexcitation of low-lying dipole transitions in ^{236}U. *Phys. Rev. C*, 42:771–774, Aug 1990. doi:10.1103/PhysRevC.42.771.

[57] E. Kwan, G. Rusev, A. S. Adekola, F. Dönau, et al. Discrete deexcitations in ^{235}U below 3 mev from nuclear resonance fluorescence. *Phys. Rev. C*, 83:041601, Apr 2011. doi:10.1103/PhysRevC.83.041601.

[58] J. L. Ullmann, T. Kawano, T. A. Bredeweg, et al. Cross section and γ-ray spectra for ^{238}U(n,γ) measured with the dance detector array at the los alamos neutron science center. *Phys. Rev. C*, 89:034603, Mar 2014. doi:10.1103/PhysRevC.89.034603.

[59] J Speth. *Electric and Magnetic Giant Resonances in Nuclei*. WORLD SCIENTIFIC, 1991. doi:10.1142/1126.

[60] S. Goriely and E. Khan. Large-scale QRPA calculation of $E1$-strength and its impact on the neutron capture cross section. *Nucl. Phys. A*, 706(1):217 – 232, 2002. doi:https://doi.org/10.1016/S0375-9474(02)00860-6.

[61] M. Martini, S. Péru, S. Hilaire, et al. Large-scale deformed quasiparticle random-phase approximation calculations of the γ-ray strength function using the gogny force. *Phys. Rev. C*, 94:014304, Jul 2016. doi:10.1103/PhysRevC.94.014304.

[62] I. Daoutidis and S. Goriely. Large-scale continuum random-phase approximation predictions of dipole strength for astrophysical applications. *Phys. Rev. C*, 86:034328, Sep 2012. doi:10.1103/PhysRevC.86.034328.

[63] G. Colò and P.F. Bortignon. QRPA plus phonon coupling model and the photoabsorption cross section for ^{18,20,22}O. *Nucl. Phys. A*, 696(3):427 – 441, 2001.

doi:https://doi.org/10.1016/S0375-9474(01)01217-9.

[64] O. Achakovskiy, A. Avdeenkov, S. Goriely, et al. Impact of phonon coupling on the photon strength function. *Phys. Rev. C*, 91:034620, Mar 2015. doi:10.1103/PhysRevC.91.034620.

[65] E. Litvinova, P. Ring, and V. Tselyaev. Relativistic two-phonon model for the low-energy nuclear response. *Phys. Rev. C*, 88:044320, Oct 2013. doi:10.1103/PhysRevC.88.044320.

[66] S. Goriely, S. Hilaire, M. Girod, and S. Péru. First gogny-hartree-fock-bogoliubov nuclear mass model. *Phys. Rev. Lett.*, 102:242501, Jun 2009. doi:10.1103/PhysRevLett.102.242501.

[67] S. Goriely, S. Hilaire, S. Péru, et al. Gogny-hartree-fock-bogolyubov plus quasiparticle random-phase approximation predictions of the $M1$ strength function and its impact on radiative neutron capture cross section. *Phys. Rev. C*, 94:044306, Oct 2016. doi:10.1103/PhysRevC.94.044306.

[68] S. Goriely, S. Hilaire, S. Péru, and K. Sieja. Gogny-HFB+QRPA dipole strength function and its application to radiative nucleon capture cross section. *Phys. Rev. C*, 98:014327, Jul 2018. doi:10.1103/PhysRevC.98.014327.

[69] M. Krtička, S. Goriely, S. Hilaire, S. Péru, and S. Valenta. Constraints on the dipole photon strength functions from experimental multistep cascade spectra. *Phys. Rev. C*, 99:044308, Apr 2019. doi:10.1103/PhysRevC.99.044308.

[70] R. Schwengner, S. Frauendorf, and A. C. Larsen. Low-energy enhancement of magnetic dipole radiation. *Phys. Rev. Lett.*, 111:232504, Dec 2013. doi:10.1103/PhysRevLett.111.232504.

[71] K. Sieja. Electric and magnetic dipole strength at low energy. *Phys. Rev. Lett.*, 119:052502, Jul 2017. doi:10.1103/PhysRevLett.119.052502.

[72] S. Karampagia, B. A. Brown, and V. Zelevinsky. Low energy magnetic radiation enhancement in the $f_{7/2}$ shell. *Phys. Rev. C*, 95:024322, Feb 2017. doi:10.1103/PhysRevC.95.024322.

[73] A. Voinov, E. Algin, U. Agvaanluvsan, et al. Large enhancement of radiative strength for soft transitions in the quasicontinuum. *Phys. Rev. Lett.*, 93:142504, Sep 2004. doi:10.1103/PhysRevLett.93.142504.

[74] M. Guttormsen, R. Chankova, U. Agvaanluvsan, et al. Radiative strength functions in $^{93-98}$Mo. *Phys. Rev. C*, 71:044307, Apr 2005. doi:10.1103/PhysRevC.71.044307.

[75] E. Algin, U. Agvaanluvsan, M. Guttormsen, et al. Thermodynamic properties of ^{56,57}Fe. *Phys. Rev. C*, 78:054321, Nov 2008. doi:10.1103/PhysRevC.78.054321.

[76] J. T. Caldwell, E. J. Dowdy, B. L. Berman, et al. Giant resonance for the actinide nuclei: Photoneutron and photofission cross sections for ^{235}U, ^{236}U, ^{238}U, and ^{232}Th. *Phys. Rev. C*, 21:1215–1231, Apr 1980. doi:10.1103/PhysRevC.21.1215.

[77] F. Bečvář. Simulation of Îş cascades in complex nuclei with emphasis on assessment of uncertainties of cascade-related quantities. *Nucl. Instrum. Meth. A*, 417(2):434 – 449, 1998. doi:https://doi.org/10.1016/S0168-9002(98)00787-6.

[78] D. A. Matters, A. G. Lerch, A. M. Hurst, et al. Investigation of ^{186}Re via radiative thermal-neutron capture on ^{185}Re. *Phys. Rev. C*, 93:054319, May 2016. doi:

10.1103/PhysRevC.93.054319.
[79] M. Krtičcka and S. Valenta. https://www-nds.iaea.org/dicebox/, 2018. URL: https://www-nds.iaea.org/dicebox/.
[80] D. Regnier, O. Litaize, and O. Serot. An improved numerical method to compute neutron/gamma deexcitation cascades starting from a high spin state. *Computer Physics Communications*, 201:19 – 28, 2016. doi:http://doi.org/10.1016/j.cpc.2015.12.007.
[81] O. Litaize, O. Serot, and L. Berge. Fission modelling with FIFRELIN. *The European Physical Journal A*, 51(12):177, 2015. doi:10.1140/epja/i2015-15177-9.
[82] C. E. Porter and R. G. Thomas. Fluctuations of nuclear reaction widths. *Phys. Rev.*, 104:483–491, Oct 1956. doi:10.1103/PhysRev.104.483.
[83] [online]URL: https://www-nds.iaea.org/dicebox/.
[84] T. Kibédi, T.W. Burrows, M.B. Trzhaskovskaya, et al. Evaluation of theoretical conversion coefficients using bricc. *Nucl. Instrum. Meth. A*, 589(2):202 – 229, 2008. doi:https://doi.org/10.1016/j.nima.2008.02.051.
[85] National Nuclear Data Center, Brookhaven National Laboratory. *Evaluated Nuclear Structure Data File - A Manual for Preparation of Data Sets*.
[86] M. Verpelli and R. Capote. Update of RIPL nuclear levels segment. *International Nuclear Data Committee INDC(NDS)-0702*, 2015.
[87] Collaboration n_TOF. CERN n_TOF facility: Performance report. Jan 2003. URL: https://cds.cern.ch/record/1258424.
[88] C. Rubbia et al. A High Resolution Spallation Driven Facility at the CERN-PS to Measure Neutron Cross Sections in the Interval from 1 eV to 250 MeV: a Relative Performance Assessment. Technical Report CERN-LHC-98-002-EET-Add.1, CERN, Geneva, Jun 1998. Addendum to CERN-LHC-98-002-EET. URL: https://cds.cern.ch/record/363828.
[89] G. Battistoni, T. Boehlen, F. Cerutti, et al. Overview of the fluka code. *Annals of Nuclear Energy*, 82:10 – 18, 2015. Joint International Conference on Supercomputing in Nuclear Applications and Monte Carlo 2013, SNA + MC 2013. Pluri- and Trans-disciplinarity, Towards New Modeling and Numerical Simulation Paradigms. doi:https://doi.org/10.1016/j.anucene.2014.11.007.
[90] C. Guerrero et al. Performance of the neutron time-of-flight facility n_TOF at CERN. *The European Phys. J. A*, 49(2):27, 2013. doi:10.1140/epja/i2013-13027-6.
[91] C. Borcea and S. Buono others. The neutron time of flight facility at CERN. *Journal of Nuclear Science and Technology*, 39(sup2):653–656, 2002. doi:10.1080/00223131.2002.10875184.
[92] K. Wisshak, K. Guber, F. Käppeler, et al. The karlsruhe 4ĬĂ barium fluoride detector. *Nucl. Instrum. Meth. A*, 292(3):595 – 618, 1990. doi:https://doi.org/10.1016/0168-9002(90)90179-A.
[93] E. Mendoza, Becares V., and Casado others A. Improved neutron capture cross section measurements with the n_tof total absorption calorimeter. *J. Korean Phy. Soc.*, 59:1813–1816, 08 2011. doi:10.3938/jkps.59.1813.
[94] M. Flaska, A. Borella, D. Lathouwers, et al. Modeling of the gelina neutron target using coupled electron–photon–neutron transport with the mcnp4c3 code. *Nucl.*

Instrum. Meth. A, 531(3):392 – 406, 2004. doi:https://doi.org/10.1016/j.nima.2004.05.087.

[95] U. Abbondanno et al. The data acquisition system of the neutron time-of-flight facility n_TOF at CERN. *Nucl. Inst. and Meth. A*, 538(1):692 – 702, 2005. doi:https://doi.org/10.1016/j.nima.2004.09.002.

[96] CASTOR. cern advanced storage manager [online]. URL: http://castor.web.cern.ch/.

[97] S. Agostinelli, J. Allison, K. Amako, et al. Geant4—a simulation toolkit. *Nucl. Instrum. Meth. A*, 506(3):250 – 303, 2003. doi:https://doi.org/10.1016/S0168-9002(03)01368-8.

[98] J. Allison, K. Amako, J. Apostolakis, et al. Geant4 developments and applications. *IEEE Transactions on Nuclear Science*, 53(1):270–278, 2006.

[99] H. Burkhardt, V. M. Grichine, P. Gumplinger, et al. Geant4 standard electromagnetic package for hep applications. In *IEEE Symposium Conference Record Nuclear Science 2004.*, volume 3, pages 1907–1910 Vol. 3, 2004.

[100] D. R. Hamilton. On directional correlation of successive quanta. *Phys. Rev.*, 58:122–131, Jul 1940. doi:10.1103/PhysRev.58.122.

[101] G. Goertzel. Angular correlation of gamma-rays. *Phys. Rev.*, 70:897–909, Dec 1946. doi:10.1103/PhysRev.70.897.

[102] E. L. Brady and M. Deutsch. Angular correlation of successive gamma-rays. *Phys. Rev.*, 78:558–566, Jun 1950. doi:10.1103/PhysRev.78.558.

[103] W Dridi. *Mesure de la section efficace de capture neutronique de l'*^{234}U *á n_TOF au CERN pour les réacteurs nucléaires de Génération IV*. PhD thesis, Université d'Evry Val d'Essonne, 2006.

[104] M.J Vermeulen. *Measurement of the* $^{236}\mathrm{U}(n,\gamma)$ *cross section for the thorium fuel cycle at the CERN n_TOF facility.* PhD thesis, University of York, 2015.

[105] T Wright. *High Accuracy Measurement of the* $^{238}\mathrm{U}(n,\gamma)$ *Cross Section at the CERN n_TOF Facility.* PhD thesis, University of Manchester, 2014.

[106] C. Guerrero, D. Cano-Ott, E. Mendoza, et al. Monte carlo simulation of the n_TOF total absorption calorimeter. *Nucl. Instrum. Meth. A*, 671:108 – 117, 2012. doi:https://doi.org/10.1016/j.nima.2011.12.046.

[107] C. Guerrero, U. Abbondanno, G. Aerts, et al. The n_TOF total absorption calorimeter for neutron capture measurements at CERN. *Nucl. Instrum. Meth. A*, 608(3):424 – 433, 2009. doi:https://doi.org/10.1016/j.nima.2009.07.025.

[108] S. F. Mughabghab. *Atlas of Neutron Resonances, Resonance Parameters and Thermal Cross Sections, Z=1–100.* Elsevier, New York, 2006.

[109] S. F. Mughabghab. *Atlas of Neutron Resonances, Resonance Properties and Thermal Cross Sections , Z=61–102.* Elsevier, 2018.

[110] A.J. Koning et al. Status of the jeff nuclear data library. *Journal of the Korean Physical Society*, 59:1057, 2011.

[111] A.J.M. Plompen et al. The joint evaluated fission and fusion nuclear data library, JEFF-3.3. *Eur. Phys. J. A*, 56:181, 2020. doi:10.1140/epja/s10050-020-00141-9.

[112] ENDF/B-VIII.0: The 8th major release of the nuclear reaction data library with cielo-project cross sections, new standards and thermal scattering data. *Nuclear*

Data Sheets, 148:1 – 142, 2018. Special Issue on Nuclear Reaction Data. doi: https://doi.org/10.1016/j.nds.2018.02.001.

université PARIS-SACLAY

ÉCOLE DOCTORALE
Particules, hadrons, énergie et noyau : instrumentation, imagerie, cosmos et simulation (PHENIICS)

Titre: Etude de la fonction force radiative et de la densité de niveaux dans la désintégration gamma suite à la capture neutronique sur les isotopes ^{234}U, ^{236}U et ^{238}U.

Mots clés: Physique Nucleaire, fonction force radiative, densité de niveaux, uranium, capture de neutrons.

Résumé: La connaissance des fonctions force radiatives et des densités de niveaux est essentielle pour modéliser les réactions nucléaires et obtenir des informations sur le flux et les intensités gamma pertinentes pour les applications nucléaires. Un certain nombre de modèles théoriques peuvent être utilisés à cette fin. Dans le cadre du modèle statistique, la cascade gamma après une réaction de capture de neutrons dépend de la densité de niveaux (LD) et de la fonction force radiative (PSF). Les réactions de capture sur des cibles U-234, U-236 et U-238 mesurées avec le calorimètre à absorption totale (TAC) à n_TOF (CERN) fournissent des informations expérimentales sur la multiplicité des gammas et sur les spectres gamma qui peuvent être comparées à des simulations numériques pour différents modèles de PSF et de LD. Les codes dédiés DICEBOX et FIFRELIN ont été utilisés pour simuler les cascades gamma tandis que GEANT4 a été utilisé pour la simulation de l'interaction de ces gammas avec les matériaux du TAC. Dans ce travail, nous avons trouvé des modèles et des paramètres cohérents reproduisant simultanément les spectres mesurés avec le TAC, la largeur radiative totale et l'espacement des niveaux pour les ondes s tels que déduits des résonances résolues, pour les trois isotopes d'uranium dans le cadre d'une même approche.

Title: Study of the photon strength functions and level densities in the gamma decay following neutron capture on the isotopes ^{234}U, ^{236}U and ^{238}U.

Keywords: Nuclear Physics, photon strength function, level density, uranium, neutron capture.

Abstract: The knowledge of photon strength functions (PSF) and level densities (LD) are essential to model nuclear reactions and to obtain information on the gamma flux and intensities relevant for nuclear applications. A number of theoretical models can be employed for this purpose. In the framework of the statistical model, the gamma cascade after a neutron capture reaction depends on the LD and PSF. The capture reactions on U-234, U-236 and U-238 targets measured with the total absorption calorimeter (TAC) at n_TOF (CERN) provide experimental information on gamma multiplicity and on gamma spectra which can be compared to numerical simulations for different PSF and LD models. The dedicated codes DICEBOX and FIFRELIN were used to simulate the gamma cascades while GEANT4 was used for the simulation of the interaction of these gammas with the TAC materials. In this work we have found consistent models and parameters reproducing simultaneously the spectra measured with the TAC, the total radiation width and the s-wave level spacing as deduced from the resolved resonances, for the three uranium isotopes within the same analysis approach.

Université Paris-Saclay
Espace Technologique / Immeuble Discovery
Route de l'Orme aux Merisiers RD 128 / 91190 Saint-Aubin, France